IMPROVEMENTS FOR CURRENT MEASUREMENTS WITH ROGOWSKI COIL AND DEVELOPMENT OF CALIBRATION SYSTEM FOR NON-CONVENTIONAL SENSORS

by

Burak Ayhan

Submitted to Graduate School of Natural and Applied Sciences
in Partial Fulfillment of the Requirements
for the Degree of Doctor of Philosophy in
Electrical and Electronics Engineering

Yeditepe University

2020

IMPROVEMENTS FOR CURRENT MEASUREMENTS WITH ROGOWSKI COIL
AND DEVELOPMENT OF CALIBRATION SYSTEM
FOR NON-CONVENTIONAL SENSORS

APPROVED BY:

Prof. Dr. Canbolat UÇAK ……
(Thesis Supervisor)
(Yeditepe University)

Prof. Dr. Fethi OLCAYTUĞ ……
(Yeditepe University)

Prof. Dr. Mukden UĞUR ……
(Türk-Alman University)

Assist. Prof. Dr. Levent OVACIK ……
(İstanbul Technical University)

Assist. Prof. Dr. Suat İLHAN ……
(İstanbul Technical University)

DATE OF APPROVAL: …./…./2020

ACKNOWLEDGEMENTS

Firstly, I would like to express my sincere gratitude Prof. Dr. Canbolat UÇAK from Yeditepe University for being my advisor during my dissertation period, and for his directive ideas, valuable suggestions and discussions. I am also grateful to him for his understanding.

To Assist. Prof. Dr. Levent OVACIK and Assist. Prof. Dr. Suat İLHAN, who are in my dissertation committee, I would like to thank for their much valuable advice.

Most importantly, special thanks and gratitude goes to my wife Tuğba AYHAN and to my son Ahmet Doruk AYHAN, who supported me and stood patiently by my side during my dissertation research, for their crucial support and encouragement. I would not have been able to complete this research without their love and support.

My thesis is dedicated to my family, to my mother and father, who raised me and provided guidance to me my whole life. Without their wisdom and support I would not be where I am today.

Thank you for everything.

ABSTRACT

IMPROVEMENTS FOR CURRENT MEASUREMENTS WITH ROGOWSKI COIL AND DEVELOPMENT OF CALIBRATION SYSTEM FOR NON-CONVENTIONAL SENSORS

Rogowski coils (RCs) known as non-conventional current sensors are widely used for measuring the magnitude of AC currents and well suited for high voltage applications. Nevertheless, the weak points of RC are the adverse effects produced by external varying magnetic fields and the sensitivity to the primary conductor positions. In order to reduce these effects, the magnetic shielding is applied to the RCs. Currently, in literature, magnetic circuit solutions for magnetic shielding effectiveness which is the critical parameter of magnetic shield assume a rectangular shell structure of shielding under vertical external magnetic fields, leading to inaccuracies in parametric analysis. Therefore, in the first part of the dissertation, improved magnetic circuit models are proposed by taking the hollow cylindrical and the toroidal structures of the shielding into consideration to investigate magnetic shielding effectiveness in RCs. The proposed models are verified by simulation studies based on the finite element method for a wide range of design parameters. It is shown that magnetic shielding effectiveness of magnetic circuit models for the hollow cylindrical and the hollow toroidal structures have no more than a 27 percent error when the shielding thicknesses and the shielding distances from non-magnetic former are varied from 5 mm to 30 mm. Moreover, the models are validated for the changes in air gaps, permeability of shielding materials, and the major radius of the non-magnetic former. In the second part of the dissertation, a magnetically shielded RC has been designed and implemented. And then, for the calibration of the RC with traditional measurement bridges, unique measuring systems are developed by adapting RC's output level to traditional levels with transducers. In addition, the novel measurement setup is developed for calibrating the analogue non-conventional input of commercially available measuring bridge with the uncertainty of 10 μA/A and 10 μrad. The magnetically shielded RC is tested and its immunity to the primary conductor position, and pick-up from nearby current conductors is found to be less than 10 μA/A.

ÖZET

ROGOWSKİ BOBİNİ KULLANILARAK GERÇEKLEŞTİRİLEN AKIM ÖLÇÜMLERİNİN İYİLEŞTİRİLMESİ VE GELENEKSEL OLMAYAN AKIM SENSÖRLERİ İÇİN KALİBRASYON SİSTEMLERİNİN GELİŞTİRİLMESİ

Geleneksel olmayan akım sensörleri olarak bilinen Rogowski bobinleri (RC) yaygın olarak AC akım büyüklüklerini ölçmekte kullanılmasının yanı sıra yüksek gerilim uygulamaları için de tercih edilmektedir. Buna karşın, dış manyetik alanların yarattığı olumsuz etkiler ve primer iletken konumlarına olan duyarlılık RC'lerin zayıf noktalarıdır. Bu etkileri azaltmak için RC'lere manyetik ekranlar uygulanmaktadır. Literatürdeki mevcut durumda, dikey yöndeki dış manyetik alanlar altında, manyetik ekranın kritik parametrelerinden biri olan manyetik ekran etkinliğinin hesaplanması için kullanılan manyetik devre çözümlerinde manyetik ekranın dikdörtgen bir kabuk yapısına sahip olduğunu varsayılmakta ve bu da parametrik analizde hatalara sebep olmaktadır. Bu sebeple, tezin ilk bölümünde RC'lerde manyetik ekran etkinliğini araştırmak için, manyetik ekranın toroidal ve silindirik yapısının göz önünde bulundurulduğu geliştirilmiş manyetik devre modeli üzerine çalışılmıştır. Bu manyetik devre modeli sonlu elemanlar yönteminin esas alındığı simülasyon çalışmaları ile çok çeşitli tasarım parametreleri için doğrulanmıştır. İçi boş silindirik ve toroidal yapıya sahip manyetik ekranların geliştirilen manyetik devre modelleri ile hesaplanan manyetik ekran etkinliklerinin, manyetik ekran kalınlığı ve manyetik ekran ile RC arasındaki mesafenin 5 mm ile 30 mm arasında değiştiği durumlarda, yüzde 27'den az bir hataya sahip olduğu görülmüştür. Buna ek olarak, bu manyetik devre modellerinin manyetik ekrandaki hava aralığının, ekranın manyetik geçirgenliğinin ve ekranın ana yarıçapının değiştirildiği durumlar için de doğrulaması yapılmıştır. Tez çalışmasının ikinci kısmında ise manyetik ekranlı RC tasarlanmış ve üretilmiştir. RC'nin geleneksel ölçüm köprüleri ile kalibrasyonu için, RC'nin çıkış seviyelerinin geleneksel seviyelere dönüştürücüler ile adapte edildiği özgün ölçüm sistemleri geliştirilmiştir. Ek olarak, piyasada ticari olarak mevcut ölçüm köprülerinin geleneksel olmayan analog girişlerinin kalibrasyonu için 10 µA/A ve 10 µrad belirsizliğe sahip yeni bir ölçüm düzeneği geliştirilmiştir. Manyetik ekranlı RC test edilmiş ve onun primer iletkenin konumuna ve yakındaki akım iletkenlere karşı bağımlılığının 10 µA/A altında olduğu bulunmuştur.

TABLE OF CONTENTS

LIST OF FIGURES

LIST OF TABLES

LIST OF SYMBOLS/ABBREVIATIONS

A	Represents electronic circuitry as a transconductance amplifier
A_i	Cross-sectional area of inner-shield
A_o	Cross-sectional area of outer-shield
A_c	Cross-sectional area of cavity inside shielding
A_{Tg}	Cross-sectional area of inner gaps in toroidal structure
A'_{Tg}	Cross-sectional area of outer gaps in toroidal structure
a	Thickness of magnetic shields
b	Distance between non-magnetic former and magnetic shields
c	Thickness of hollow cylindrical magnetic shielding structure
C_1	Represents magnetic shield in the form of hollow cylindrical structure
C_2	Represents thick magnetic shield made by ferromagnetic foil
C_3	Represents detector core
E_1	Represents electrostatic shield made by copper foil
E_2	Represents electrostatic shield made by copper foil
F	Magnetomotive force
g	Air gap distance between magnetic shields
h	Thickness or radius of non-magnetic former of RC
H	Magnetic field intensity
$\bar{H}_0$	Average magnetic field intensities before magnetic shielding in the non-magnetic former
$\bar{H}_T$	Average magnetic field intensities after magnetic shielding in the non-magnetic former
I_p	Primary current
I_s	Secondary current
I_M	Magnetizing current
N_D	Number of turns of detection winding
N_P	Number of turns of primary winding
N_S	Number of turns of secondary winding
N_{C1}	Number of turns of compensation winding
N_{C2}	Number of turns of compensation winding

N_{add1} Number of turns of additional winding for generation of known ratio error

N_{add2} Number of turns of additional winding for generation of known phase displacement

r Major radius of non-magnetic former of RC

r_1 Inner radius of hollow cylindrical magnetic shielding structure

r_2 Outer radius of hollow cylindrical magnetic shielding structure

r_3 Inner radius of the cross-sectional view of hollow toroidal magnetic shielding structure

r_4 Outer radius of the cross-sectional view of hollow toroidal magnetic shielding structure

R_B Resistances of secondary burden

S Shielding effectiveness

S_H Magnetic shielding effectiveness without air gap for horizontal external magnetic fields

S_V Magnetic shielding effectiveness without air gap for vertical external magnetic fields

S_{Vh} Magnetic shielding effectiveness with horizontal air gap for horizontal external magnetic fields

S_{Vv} Magnetic shielding effectiveness with vertical air gap for horizontal external magnetic fields

V_{m_1} Magnetic scalar potential between point Q_1 and Q_2

V_{m_2} Magnetic scalar potential between points P_1 and Q_1

V_{m_s} Magnetic scalar potential between points P_1 and P_2

V_{m_T} Magnetic scalar potential between points P_1 and P_2 in the air

$V_{m_{TRC}}$ Magnetic scalar potential between points P_1 and P_2 in the air when RC former is air

ϕ Magnetic flux

ϕ_S Flux entering the magnetic shield

ϕ_T Flux entering into the air between non-magnetic RC former and magnetic shield

ϕ_o External vertical magnetic flux

μ Relative permeability of magnetic material

μ_0 Permeability of free space

$\mathcal{L}$ Permeance

$\mathcal{R}$ Reluctance

AC	Alternating current
CC	Current comparator
DC	Direct current
DIN	German Institute for Standardization
ECCC	Electronic compensated current comparator
FEM	Finite element method
IEC	International Electrotechnical Commission
IEEE	Institute of Electrical and Electronics Engineers
NBS	National Bureau of Standards in United States of America
NMI	National Metrology Institute
PCB	Printed circuit board
ppm	Parts per million
PTB	National Metrology Institute of Germany
RC	Rogowski coil
SI	International system of units
UME	National Metrology Institute of Turkey
VTT	Finland Metrology Institute

1. INTRODUCTION

Rogowski coils (RCs) are well recognized as current sensors for several decades and they are exceptionally well suited for high-voltage applications. Mainly, RCs surround current feeding conductor in a toroidal form and a voltage is induced at the coil terminals proportional to the conductor current as a result of the alternating magnetic field. Since RCs have no ferromagnetic material as core, they will not saturate, and therefore, they will exhibit linear characteristics for a wide range of measured current. The current feeding conductor is the primary and the Rogowski coil is the secondary winding. Most often the primary winding has only one turn.

The weak points of RCs are the effects produced by external varying magnetic fields and the position of the primary conductor in the vicinity of the coil. A magnetic shield can be utilized to decrease its vulnerability against the coupling of external magnetic fields in RCs. The magnetic shielding, applied to the current comparators with its first use dating back to the 1960s, will be adapted to the RC in this dissertation. Before the design of magnetic shield, the effects of the parameters such as thickness of magnetic shield, distance between non-magnetic former and magnetic shield, air gap distance between magnetic shields, permeability of magnetic cores, etc. are investigated through proposed magnetic circuit model and Finite Element Method (FEM).

The magnetic shield effectiveness is the most important specification of magnetic shield and it is generally expressed as the ratio of magnetic field intensity at a point without a magnetic shield to magnetic field intensity at the same point in the presence of a magnetic shield. The shielding effectiveness S can be written as

$$S = \frac{H_0}{H_T} \tag{1.1}$$

where H_0 and H_T are the magnetic field intensities before and after magnetic shielding in the coil former, respectively. In the literature, there has been no statement on which points are considered for the calculations of the shielding effectiveness. Since a magnetic field intensity with and without shielding may change from point to point in general, a shielding effectiveness value will depend on the location of the points in the shielding cavity. Therefore, shielding effectiveness of magnetic shielding for RCs will be simulated with FEM

by considering different points in shielding cavity, and a simple and more accurate estimation models will be proposed to calculate shielding effectiveness for the hollow cylindrical and the hollow toroidal structure.

In this dissertation, the magnetic shield will be constructed by four tape-wound magnetic cores, in the form of a hollow cylindrical structure which surrounds the rectangular non-magnetic former of RC with horizontal air gaps. The construction of a magnetic shield with vertical air gaps is also possible for the cylindrical magnetic shielding structure. Tape-wound magnetic cores will be preferred in power system applications because of the simplicity of their construction. The hollow cylindrical magnetic shield will be combined with windings inside and outside of the shield to prevent its saturation.

The metrological infrastructure for the calibration and characterization of non-conventional current sensor such as RC will be prepared by developing calibration systems. These novel calibration systems will be evaluated by considering their measurement uncertainty. An additional aim will be the establishment of a traceable calibration service for a commercially available measuring bridge for non-conventional current sensors.

The dissertation document is organized as follows: Literature review is presented in Chapter 2. The magnetic shield is analyzed by developing a magnetic circuit model for hollow cylindrical and hollow toroidal structures, and then these models are verified by FEM simulations in Chapter 3. The design stages of magnetically shielded RC is described and the effects of the design parameters on the shielding effectiveness are studied in detail in Chapter 4. The different calibration systems for non-conventional current sensors and commercially available measuring bridge are developed in Chapter 5. In addition, the metrological performance of magnetically shielded RC is investigated in the same chapter. The conclusion of the dissertation are presented in the last chapter.

2. LITERATURE REVIEW

The literature review is categorized by considering main topics of the dissertation as the design of RCs, magnetic shielding techniques, calibration methods for RCs, estimation of measurement uncertainties, and the traceability of calibration results to International system of units (SI units).

The first coil was developed by Chattock for measuring the difference of magnetic potential between any two points. The coil with a circular cross-section was evenly wound on a core of flexible gas-tubing made by plaited and varnished canvas [1]. W. Rogowski and W. Steinhaus used the Chattock's technique to measure time-varying current by bringing the beginning and the end of the winding together to form a closed loop around a current-carrying conductor. Their coil was uniformly wound upon a flexible strip of pressboard. It is now named the Rogowski coil [2].

RCs can be constructed such as single or multi-layer, and rigid or flexible [3]. The former of RC is made of non-ferromagnetic materials such as plastic, castermid or other types of non-magnetic materials. Single-layer coils are used for AC current measurement in which a low mutual inductance and a low phase displacement are required. Multi-layers coils are preferred to measure a low AC current owing to the fact that it has higher values of mutual inductance.

To overcome the weaknesses of RCs, they are designed by considering three main points which are as follows, to create nearly perfect compensation counter-turn, to make uniform pitch advancement, and to make all turns nearly identical. A single layer RC was manufactured by using numerically controlled methods [4]. A toroidal core of RC had a rectangular cross-section made of a machinable glass-ceramic material, and it was coated with a thin electrically conductive silver-composition coating. The coil was finally formed by removing very thin lines of the conductive material by laser machining. This procedure resulted in a much lower positional sensitivity of the coils, and the achieved accuracy was of the order of 0.2 percent.

Precision machined non-magnetic formers with low expansion coefficient and special winding machines for uniformity are used in the design of a rigid coil. A design of split RC

and an active electronic integrator for the output of RC were described in Reference [5]. The influences of temperature impact on the winding and of thermal expansion of a coil former were examined and then a method was developed to minimize these influences by adjusting the input resistance of the integration [6]. An axial symmetry of coil turns was provided by molding of thermoplastic coil former materials with grooves on the surface of the former [7]. In addition to this, air-turn cancellation effectiveness of the coil was enhanced by using a resistive divider at the coil output.

Currently, the uses of two- and three- dimensional Printed circuit board (PCB) techniques have become very popular in order to obtain a perfect uniformity at coil windings and to decrease the temperature dependency of the coil. The nearly perfect uniformity at coil windings was achieved by using PCB material [8]. The coil comprises of a printed plate with a conductive rectilinear pattern on both sides. These conductive patterns were logically placed on both sides to provide electrical connections among the coil winding segments. Thermal expansion coefficients of materials were taken into consideration in the selection of plate material. To reduce the effect of temperature on the output of this PCB Rogowski coil, a defined value of a resistor was connected in series with the PCB Rogowski coil output [9]. This approach is similar to the one described in Reference [6].

For achieving higher accuracy, RC was fabricated by successively placing two identical coils consisting of printed circuit boards with conductive patterns. These coils were wound in opposite pitch-progressing directions around their cores. A similar approach was adopted to split-core type RCs for installation without the need to disconnect primary conductors. Comprehensive performance tests of these non-split and split PCB Rogowski coils were carried out and the measurement results were presented in Reference [10]. This design was improved by applying a separate electromagnetic shielding to the coils and using a double-shielded twisted pair cable to mitigate noise effects [11].

Three-dimensional PCB structure containing a return loop located in a middle layer was introduced for minimizing the influence of a nearby primary conductor [12]. Another structure for three-dimensional PCB coils was manufactured by using a multi-layer single printed circuit board [13]. The coil consists of an outer and an inner coil which is wound on opposite pitch-progressing directions. The turn density of inner coil is larger than the turn density of the outer coil to compensate its smaller turn size.

RC has a sensitivity to external magnetic fields since the cross-sectional area of each turn in the coil is not the same with others, the turn density is not uniform around the coil and the coil shape is not the same everywhere in the coil. In order to reduce its vulnerability against coupling of external magnetic fields, the magnetic shielding is applied to the RCs [14]. In the dissertation, it is planned to adapt the magnetic shielding used in the current comparators [15], [16] and [17] to RC.

The error of current comparator has two components; a magnetic error and a capacitive error. Reference [18] concentrates on minimizing magnetic error of the current comparator. Magnetic error of the current comparator is minimized by keeping out external magnetic fields from the detection core using the magnetic shield.

External magnetic fields are classified into three categories which are horizontal, vertical and dipole-type fields. The studies done in the literature are grouped as shown in Figure 2.1 according to the types of external magnetic fields.

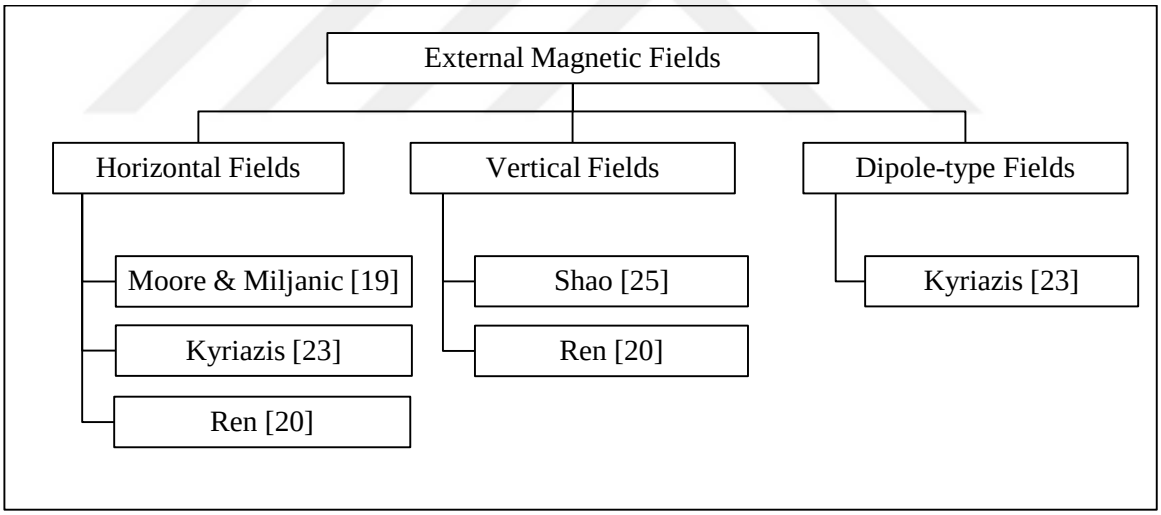

Figure 2.1. Studies in the literature

In Reference [19], a formula based on the magnetic circuit approach was proposed to calculate the magnetic shielding effectiveness of the current comparator for horizontal external magnetic fields. The derived formula is as follows:

$$S_H = \frac{\mu_S}{\mu_0} \frac{8}{l^2} a\, b \tag{2.1}$$

Considering Equation (2.1), the magnetic shielding effectiveness is in direct proportion to the permeability ratio μ_S/μ_0 and the product of the thickness of the shield a and air gap b, and it is in inverse proportion to the square of distance l. In Reference [19], the authors concluded that a and b should be equal in order to provide optimum shielding effectiveness.

The more accurate formula for the horizontal external magnetic fields was achieved by means of a long rectangular shell model in Reference [20]. The derived formula for horizontal shielding effectiveness is given by

$$S_H = \frac{\mu_S}{\mu_0}\frac{8}{l^2}\frac{ab(c-a)}{(c-b-2a)} \tag{2.2}$$

In addition to the horizontal shielding effectiveness, the formula was derived in order to calculate the magnetic shielding effectiveness for vertical external magnetic fields. The derived formula was improved in Reference [21] and a simpler and more accurate formula was obtained. The formula is given by

$$S_V = \frac{\mu_S}{\mu_0}\frac{8}{3}\frac{ab}{c(c-a)} - \frac{2a}{c} + 1 \tag{2.3}$$

In Reference [21], experiments were performed on a 25 kA DC comparator to measure the magnetic shielding effectiveness in the presence of external horizontal and vertical magnetic fields for verifications of analytical results calculated by Equations (2.2) and (2.3). Relative errors between experiments and analytical results were found to be less than 5 percent. According the Equations (2.2) and (2.3), the magnetic shielding effectiveness of comparators depends on the permeability ratio μ_S/μ_0 and the dimensions of the magnetic shield given by a, b, c and l. If the magnetic shield has no air gap between magnetic cores constructing the magnetic shield, magnetic shielding effectiveness for vertical magnetic fields S_V is much better than that for horizontal magnetic fields S_H.

3D FEM was introduced for a calculation of magnetic shielding effectiveness in Reference [22]. The numeric results were compared with analytical results derived in Reference [21] and some experiments were performed by the authors. The results are given in Table 2.1, and it is noticeable that shielding effectiveness values from three different approaches get close to each other when the permeability of the magnetic shielding core is high.

Table 2.1. Comparison of analytical, numerical and experimental results

μ_r	FEM Results	Analytical Results	Experimental Results
5000	20.5	21.1	20.2
3000	13.3	12.4	13.5
500	8.5	2.02	8.6
300	4.4	1.12	4.5

The effectiveness of magnetic shielding in the current comparator was studied for radial, axial and dipole magnetic fields in Reference [23]. Two simple formulas were derived to calculate the magnetic shielding effectiveness against dipole and radial magnetic fields using the magnetostatic approximation. The formula for axial magnetic fields was derived by using the magnetic circuit approach. The analytical results were verified by detailed experiments. The paper concludes that the differences between the measurement and analytical solution were reasonable. A small difference for dipole magnetic fields was occurred due to the assumption of a single thickness in the computation. Consequently, magnetic shield permeability, thickness, cross-sectional dimensions and the air gap between the shield and the core are shown to be the critical parameters for the design of the magnetic shield.

Magnetic shielding effectiveness in high power dc comparator was computed based on a magnetic circuit method for horizontal external magnetic fields in Reference [24]. The calculation method was verified by experiments. Analytic result was found to be closer to the experimental result.

Reference [25] concentrated on the negative effect of air gaps which are unavoidable in the design of the magnetic shield. They declared that Equation (2.2) was valid for horizontal magnetic fields but Equation (2.3) was invalid for vertical magnetic fields in the presence of air gap. According to the formulas for vertical external magnetic fields, the magnetic shielding effectiveness with the vertical air gap is twice as that with the horizontal air gap.

$$S_{Vh} = \frac{2ab}{cg} \ (\mu_s \gg \mu_0) \tag{2.4}$$

$$S_{Vv} = \frac{4ab}{cg} \ (\mu_s \gg \mu_0) \tag{2.5}$$

Numeric analysis based on the magnetic scalar potential was conducted by FEM to confirm the equations. The FEM results were compared with the analytical results. In addition, experiments were performed on 1 kA DC current comparator with the horizontal air gap to confirm the equations. The Helmholtz coils were used to generate the external horizontal and vertical magnetic fluxes. The listed tables in Reference [25] show that the experiment and analytic results are close to each other.

The shielding effectiveness of double-layer magnetic shield was studied by using a magnetic circuit approach under external horizontal magnetic fields in Reference [26]. The formula for the calculation of magnetic shielding effectiveness was derived and it is validated by FEM simulations. The relative errors between analytical and simulation results were found to be less than 30 percent. The study concludes that the greater value of shielding effectiveness on double-layer magnetic shield can be achieved when the thickness of the magnetic shield is equal to the distance between non-magnetic RC former and shields.

Magnetic shielding effectiveness of current comparator was numerically computed by using the commercial ANSYS program in Reference [27]. Two and three-dimensional structures of current comparator were simulated by using numeric methods and the simulation results of two and three-dimensional structures were found to be reasonably close the each other in Reference [28].

Although there are numerous publications about the design, production, and application of RC in the literature, there are few publications about its calibration and its traceability to SI units [29].

The basic calibration setup is presented in DIN EN 60044-8 standard for electronic current transformers / current sensors [30]. The calibration setup consists of a reference current transformer, AC current shunt, and a lock-in amplifier. The primary current is applied to both the reference current transformer and the RC. The secondary current of reference current transformer is converted to a voltage by AC current shunt. The voltage across on AC current shunt and the voltage output of RC with the integrator are compared by a lock-in amplifier.

The similar measurement setup was established for the calibration of RC with the integrator in the current range of 30 kA [31]. Uncertainty components of measurement were described in detail and the maximum 0.035 percent of measurement uncertainty was obtained by using this setup. The same system was modified for high-frequency measurements by using a coaxial current shunt instead of a standard current transformer in Reference [32].

A coil of known mutual inductance was used as a reference in the calibration setup of RC instead of the reference current transformer in Reference [4]. Output voltages of coils were connected to a digitizer with high-speed and high resolution. The ratio of two voltages gave the mutual inductance of the coil to be calibrated with the correction of mutual inductance of the reference coil. No information about the phase displacement of the RC was available in Reference [4].

In Reference [33], RC calibration was performed against AC current shunt at the current level of 10 A. Voltage signals from RC and the current shunt were digitized by two sampling voltmeters. Mutual inductance and phase displacement were calculated with the digitized values. The phase differences between the ranges of two voltmeters were taken into account and compensated in the frequency domain by using special software. The current linearity of the mutual inductance of the calibrated coil was found to be less than 10 μH/H from 10 A to 8 kA. The overall uncertainty in the laboratory condition was estimated to be within 0.0025 percent for ratio error and 50 μrad for phase displacement up to 8 kA. The accuracy of the calibration was confirmed by the participation of international comparison.

The designed and characterized RC in Reference [33] was used at on-site calibration of current transformer as reference by locating in a fixed coaxial busbar. The uncertainties were calculated as 0.01 percent for ratio error and 100 μrad for phase displacement [34].

Another calibration setup for RC is described in the Institute of Electrical and Electronics Engineers (IEEE) standard [35]. The calibration system comprises of standard current transformer, a voltage to current converter and a traditional CT test-set. The primary current is applied to both reference current transformer and RC. The output voltage of RC is first converted to a current level (generally 1 A) to accommodate the input range requirements of the CT test-set. Next, the converted current and the secondary current of the standard current transformer are compared and the ratio error and the phase displacement of RC are measured by the traditional CT test-sets. The ratio error of the voltage to current converter used in the

calibration setup was verified by employing precise standard resistor and digital multimeter [36]. The uncertainty of this calibration system was estimated to be 0.230 percent for the ratio error and 1.9 min for the phase displacements. These high values of uncertainty do not meet the needs of calibration laboratories.

A similar calibration setup with a special transconductance amplifier was established to achieve better accuracy [37]. Since errors of reference current transformer and CT test-set are minor, the overall accuracy of the calibration system is determined by the error of the transconductance amplifier. Ratio error and phase displacements of the transconductance amplifier were determined by developing the calibration system. This calibration system was verified by the AC power measurement system with 20 μW/VA accuracy.

A new high accuracy calibration system for RCs was built by using the nonsynchronous digital sampling technique for power frequencies [38]. The current-comparator-based transimpedance amplifier and two-stage current transformer were used as a range extenders. The secondary current of reference current transformer was converted to a voltage by using transimpedance amplifier with integrating an inductive voltage divider. The output voltage of the transimpedance amplifier and the output voltage of RC were separately connected to the two digital voltmeters for sampling. The rated burden of RC was adjusted by adding appropriate resistors by considering the input resistance of the digital voltmeter. The devices establishing the calibration system were evaluated on a component basis. By using a high accurate calibration system, expanded uncertainties were estimated to be less than 0.0050 percent for ratio error and 50 μrad for phase displacement up to 2 kA. This calibration system was modified for frequencies up to 10 kHz by changing transimpedance amplifier with a current shunt and by designing an optional numeric integration of the coil output signal [39]. Current generating capability was limited to 100 A for frequencies up to 10 kHz and the calibration uncertainties were found to be less than 0.05 percent for ratio error and 500 μrad for phase displacement which are more than uncertainties estimated at power frequencies.

The requirements were found out for the calibration of RC and consequently, three different calibration techniques were developed at National Metrology Institute of Turkey (UME), National Metrology Institute of Germany (PTB) and Dutch National Metrology Institute (VSL) [40]. The operation and evaluation of these calibration setups were presented [41]. The uncertainties of each calibration system were calculated separately. All information is summarized including electronic current transformers with digital outputs [42].

The calibration methods of commercial test-sets for non-conventional instrument transformer with analog and digital outputs were presented [43]. The calibration method is to apply known ratio error and phase displacement values to the commercial test-sets. The technicality of the calibration setup is given in Chapter 5.3 in detail.

The calibration systems explained here are generally used for determining the linearity of RC, the influence of the current conductor position inside the coil window and the nearby current conductor, gap opening sensitivity for split cores and temperature dependencies of RC.

Eight RCs with three different sizes were examined against the precision air core of National Bureau of Standards (NBS) to determine their positional sensitivity, gap opening sensitivity for split types and proximity effects of the return conductor. Sensitivity variations for all effects were found in the order of a few tenths of one percent [44]. Sensitive to the effects of orientation and proximity of rigid coils was found to be less than splits coils.

A high precision mutual inductor with electrostatic and magnetic shields was designed in Reference [45]. Its immunity to external fields and independence of mutual inductance on primary conductor positions was measured. Approximately 100 times improvement was achieved on mutual inductance changes arising from the primary conductor position and ambient magnetic fields after the shields.

The influence of primary current position on the mutual inductance of the coil was investigated in Reference [46] .The position of the primary conductor has no effect on the mutual inductance of the coil in an ideal coil. However, this is not certainty true in the real cases due to the imperfection of windings of the coil. The difference of mutual inductances between the ideal model and the real case was calculated and the analytical results were confirmed by the measurements. As a result, it is concluded that RC should be centered and fixed to perform high accuracy AC current measurement and the windings of RC must be wound as uniform as possible to achieve constant and stable output.

The effects of the current source, the corners in the primary conductor and return conductor on the accuracy of high precision split-core RC were tested by using two sampling voltmeters (Agilent 3458A) and a special bus bar system in Reference [47]. The changes in the ratio error and the phase displacement were presented for each effect. A safe clearance for RC was defined by considering the data of changes. Then, this data was used for

estimating of an overall uncertainty of calibration system where this coil was in Reference [48].

ART type LEM model RC was tested for linearity and sensitivity to the primary conductor position by PTB in Reference [49]. A maximum error variation was measured as 0.12 percent in ratio error when the primary conductor has touched the coil window with 90° steps. There were no significant error variations on phase displacements.

Mutual inductances between RC and the conductor which are straight, curvilinear, large cross-section were calculated and theoretical results were evaluated by experiments [50]. Besides, a gap compensation for the split-core RC was studied. The making of gap compensation by increasing the turns at the end fittings of the coil was described. It is concluded that an air gap must be kept as small as possible to have a low sensitivity to external magnetic fields.

3. ANALYSIS OF MAGNETIC SHIELDING

The magnetic shield consists of four tape-wound magnetic cores, in the form of a hollow cylindrical structure which surrounds the rectangular non-magnetic former with horizontal air gaps is shown at the top section of Figure 3.1. At the bottom section of Figure 3.1, a half-section view of the magnetic shield consists of a hollow toroidal structure that surrounds the circular non-magnetic former with horizontal air gaps is shown. In high-voltage power system applications primary current shown in Figure 3.1 has 50 Hz fundamental frequency to be measured by RCs.

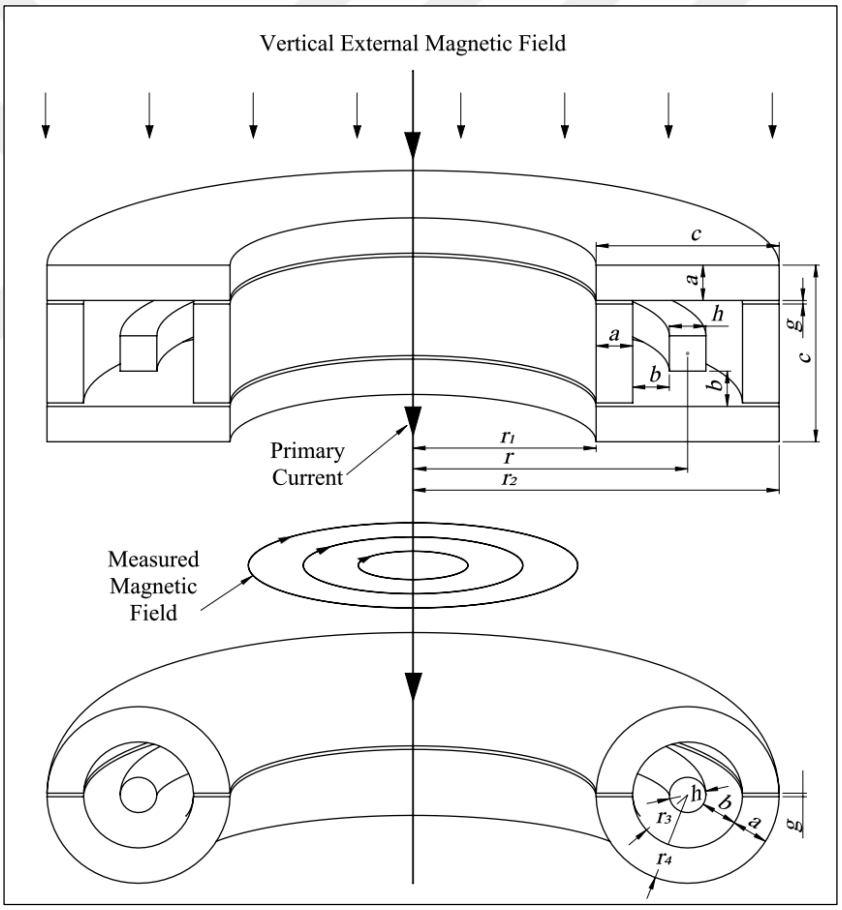

Figure 3.1. Half – section views of non-magnetic RC formers enclosed by four tape-wound magnetic cores of rectangular cross-sections with horizontal air gaps (above) and enclosed by toroidal magnetic cores with horizontal air gaps (below)

Construction of a magnetic shield with vertical air gaps is also possible for cylindrical magnetic shielding structure. Hence, the proposed method provides a magnetic circuit model for the devices with horizontal or vertical air gaps.

In the literature, the magnetic shielding effectiveness is generally expressed as the ratio of the magnetic field intensity at a point without a magnetic shield to the magnetic field intensity at the same point in the presence of a magnetic shield. Nevertheless, applying magnetic shielding may alter the magnitudes and directions of magnetic field intensity vectors differently at each point. Therefore, in this paper, the averages of the magnetic field intensities in the non-magnetic former before and after applying magnetic shielding are used to calculate shielding effectiveness in the FEM simulations. The shielding effectiveness S can be written as

$$S = \frac{\bar{H}_0}{\bar{H}_T} \tag{3.1}$$

Reference [25] refined the formula for magnetic shielding effectiveness developed in Reference [21] for vertical external magnetic fields when air gaps exist. The authors calculated the shielding effectiveness for a current comparator when a high permeability detection core is used. The formulas revived step by step for horizontal air gaps below. The external vertical magnetic flux is divided into two parts shown in Figure 3.2 as the flux entering the magnetic shield and the flux entering into the air between core and magnetic shield.

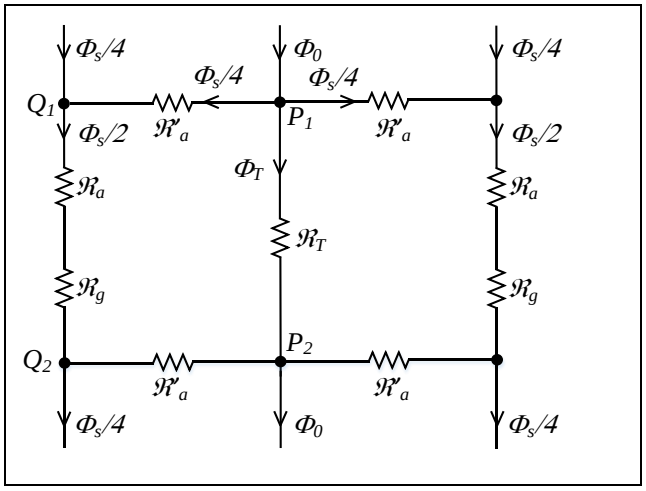

Figure 3.2 Magnetic circuit model for horizontal air gaps

$$\emptyset_0 \;=\; \emptyset_S + \emptyset_T \tag{3.2}$$

Since $\emptyset = B \cdot A = \mu \cdot H \cdot A$ and D is defined as a depth. $\emptyset_S$ and $\emptyset_T$ become

$$\emptyset_S \;=\; \mu\, H_S\, 2\, a\, D \tag{3.3}$$

$$\emptyset_T \;=\; \mu_0\, H_T\, (c - 2\, a)\, D \tag{3.4}$$

Therefore, we can get

$$\mu_0\, H_0\, c\, D \;=\; \mu\, H_S\, 2a\, D + \;\mu_0\, H_T\, (c - 2a)\, D \tag{3.5}$$

The equation (3.5) is divided by D.

$$\mu_0\, H_0\, c \;=\; \mu\, H_S\, 2a + \;\mu_0\, H_T\, (c - 2a) \tag{3.6}$$

Equation (3.6) is correct when the structure is rectangular and not circular. $\mathcal{R}_a$ and $\mathcal{R}_g$ are the reluctances of magnetic shield path between point Q_1 and Q_2 and horizontal air gap. Magnetic scalar potential between point Q_1 and Q_2 is

$$V_{m_1} \;=\; \mathcal{R}_a \frac{\emptyset_s}{2} + \mathcal{R}_g \frac{\emptyset_s}{2} = \frac{c - a - 2g}{\mu_s\, a\, D}\, \frac{\emptyset_s}{2} + \frac{2g}{\mu_0\, a\, D}\, \frac{\emptyset_s}{2} \tag{3.7}$$

$$V_{m_1} \;= (c - a - 2g)\, H_S + 2g\;\, H_S\, \frac{\mu}{\mu_0} \tag{3.8}$$

$\mathcal{R}_a'$ is the reluctance of magnetic shield path between points P_1 and Q_1. The magnetic scalar potential between points P_1 and Q_1 is

$$V_{m_2} \;=\; \mathcal{R}_a' \frac{\emptyset_S}{4} = \frac{\frac{c - a}{2}}{\mu\, a\, D}\, \frac{\emptyset_S}{4} = \frac{c - a}{2\mu\, a\, D}\, \frac{\mu\;\, H_S\, 2a\, D}{4} = \frac{H_S}{4}(c - a) \tag{3.9}$$

Paper assumes that half of $\frac{\emptyset_S}{2}$ is coming from each branch connected to the point Q_1. In the magnetic shielding, the magnetic scalar potential between points P_1 and P_2 is

$$V_{m_s} = V_{m_1} + 2V_{m_2} = (c - a - 2g)\ H_s + 2g\ H_s \frac{\mu}{\mu_0} + 2\frac{H_s}{4}\ (c - a) \qquad (3.10)$$

Equation (3.10) is bracketed in H_s

$$V_{m_s} = (c - a - 2g + 2g\frac{\mu}{\mu_0} + \frac{c - a}{2})\ H_s \qquad (3.11)$$

$$V_{m_s} = \left[\frac{3(c - a)}{2} + 2g\ (\frac{\mu}{\mu_0} - 1)\right]\ H_s \qquad (3.12)$$

$\mathcal{R}_T$ is the reluctance of distance between non-magnetic former and magnetic shields. The magnetic scalar potential between points P_1 and P_2 in the air is

$$V_{m_T} = \mathcal{R}_T \emptyset_T = \frac{2b}{\mu_0(c - 2a)D}\ \emptyset_T = \frac{2b}{\mu_0(c - 2a)D}\mu_0\ H_T(c - 2a)D \qquad (3.13)$$

$$V_{m_T} = 2\ b\ H_T \qquad (3.14)$$

As the magnetic scalar potential difference between two points only depends on their positions, thus

$$V_{m_s} = V_{m_T} \qquad (3.15)$$

Relation between H_s and H_T becomes

$$H_s = \frac{2b}{\left[\frac{3(c - a)}{2} + 2g\ (\frac{\mu}{\mu_0} - 1)\right]}\ H_T \qquad (3.16)$$

Carrying Equation (3.16) to Equation (3.6) to define the relation between H_0 and H_T

$$\mu_0\ H_0\ c = \mu\frac{2b}{\left[\frac{3(c - a)}{2} + 2g\ (\frac{\mu}{\mu_0} - 1)\right]}\ H_T\ 2a + \mu_0\ H_T\ (c - 2a) \qquad (3.17)$$

$$H_0 = \left[\frac{4ab}{\frac{3(c-a)}{2} + 2g\,(\frac{1}{\mu_0} - \frac{1}{\mu})} + (c-2a)\mu_0\right]\left[\frac{1}{\mu_0 c}\right] H_T \tag{3.18}$$

Magnetic shielding effectiveness for vertical magnetic field and horizontal gaps is

$$S_{Vh} = \frac{H_0}{H_T} = \frac{4ab}{c\left[\frac{3(c-a)}{2}\frac{\mu_0}{\mu} + 2g(1-\frac{\mu_0}{\mu})\right]} + \frac{(c-2a)}{c} \tag{3.19}$$

If $\mu \gg \mu_0$

$$S_{Vh} = \frac{H_0}{H_T} = \frac{2ab}{cg} - \frac{2a}{c} + 1 \tag{3.20}$$

$$S_{Vh} = \frac{H_0}{H_T} = \frac{2ab}{cg} \tag{3.21}$$

Equation (3.21) is derived to calculate the magnetic shielding effectiveness in the current comparator under the vertical magnetic field, considering the horizontal air gaps.

The same formulation, with a slightly different form, can be adapted for RC where non-magnetic former has unity relative permeability. In that case, for horizontal air gaps, $\mathcal{R}_T$ and the magnetic scalar potential ($V_{m_{TRC}}$) between points P_1 and P_2 in the air are

$$V_{m_{TRC}} = \mathcal{R}_T \emptyset_T = \frac{(c-2a)}{\mu_0(c-2a)D}\ \emptyset_T = \frac{1}{\mu_0 D}\mu_0\, H_T(c-2a)D \tag{3.22}$$

shielding effectiveness is

$$S_{Vh} = \frac{c-2a}{cg}\left(a + g - \frac{a[3(c-a)-4g]}{3(c-a)+4g(\mu-1)}\right) \tag{3.23}$$

and for vertical air gaps, shielding effectiveness is

$$S_{Vv} = \frac{c-2a}{cg}\left(2a + g - \frac{2a[3(c-a)-2g]}{3(c-a)+2g(\mu-1)}\right) \tag{3.24}$$

These formulas adapted from [25] are derived by considering a rectangular shell structure of the shielding and assuming that fluxes in inner and outer shields are distributed equally for a vertical external magnetic field. These assumptions contribute to the error when the thicknesses and shielding distances are varied to study the magnetic shielding effectiveness. Therefore, in this dissertation, an improved magnetic circuit model that accounts for the cylindrical or the toroidal structure of the RC is proposed; when a vertical external magnetic field exists. The proposed magnetic circuit model can also be used as a tool for the analysis and design of magnetic shielding of current comparators.

3.1. MAGNETIC CIRCUIT APPROACH

Straightforward calculations of fluxes or magnetic fields are achieved by considering a magnetic circuit model for magnetic devices [51]. In magnetic circuits, fluxes can be regarded to be confined by the path of ferromagnetic materials characterized by magnetic reluctances and are calculated by means of circuit theory. The magnetic circuit models for the horizontal and the toroidal structures have been developed in the following section.

3.1.1. Magnetic Circuit Models of Hollow Cylindrical Structure for Vertical and Horizontal Gaps

Since the magnetic device has a hollow cylindrical structure, calculation of reluctance in any radial circular structure can first be obtained, and then, by using the nodal equation method, the magnetic shielding effectiveness equation can be derived. The reluctance of magnetic material in the direction of the flux shown in Figure 3.3, is obtained by considering an infinitely small section of length dx.

If the permeability of the material is μ, differential reluctance of the dx length becomes

$$d\mathcal{R}(x) = \frac{dx}{\mu\, a\, \alpha\, x} \tag{3.25}$$

For a circular structure $\alpha = 2\pi$, thus reluctance becomes

$$\mathcal{R} = \frac{1}{\mu . 2\pi . a} \, ln \, \frac{r_2}{r_1} \tag{3.26}$$

The reluctance in (3.26) is defined for $r_2 \geq r_1$ and $r_1 > 0$.

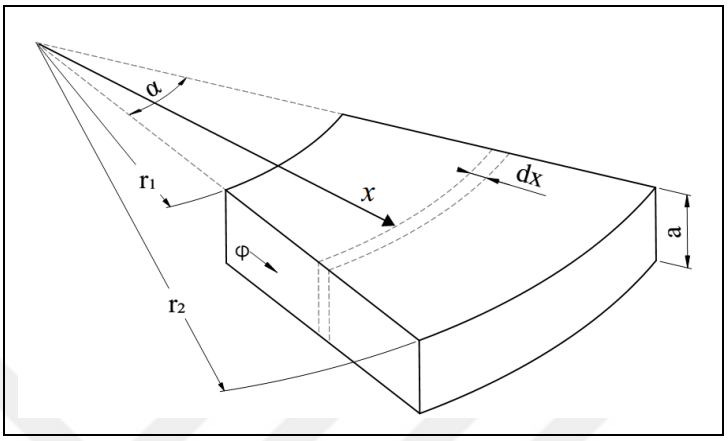

Figure 3.3. A section of hollow cylindrical structure for radial reluctance calculation

Magnetic circuit models for horizontal and vertical air gaps are created based on the points considered in the cross-sectional view of the shielding structure shown in Figure 3.4. The dashed lines represent the shielding with the vertical air gaps. Therefore, the points considered are the same for both shielding designs.

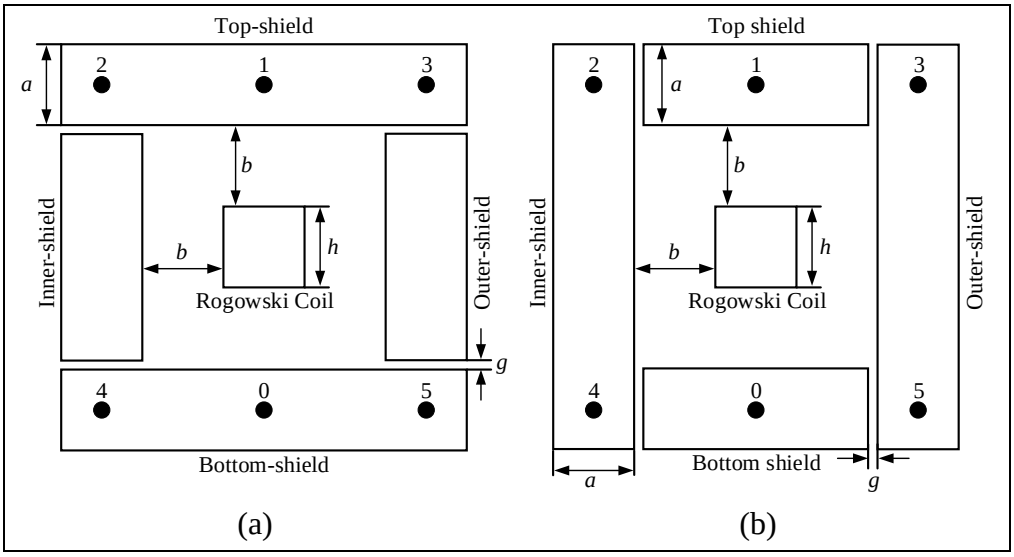

Figure 3.4. Node locations considered for magnetic circuit modeling of hollow cylindrical magnetic shielding for (a) horizontal air gaps and for (b) vertical air gaps

A magnetic circuit model for the horizontal air gaps is shown in Figure 3.5. The top-shield and the bottom-shield are represented by seven different reluctances given as $\mathcal{R}_0$, $\mathcal{R}'_0$, $\mathcal{R}_1$, $\mathcal{R}'_1$, $\mathcal{R}_2$, $\mathcal{R}_{H3}$, $\mathcal{R}'_{H3}$. Note that $\mathcal{R}_0$ and $\mathcal{R}'_0$ represent the reluctances for the fluxes entering from the top-shield and leaving from the sides of bottom-shield. They will not affect the magnetic shielding effectiveness since they do not alter the fluxes entering to the connected nodes. They are included for the sake of representing the magnetic device. The inner-shield reluctance is $\mathcal{R}_{Ha}$ and the outer-shield reluctance is $\mathcal{R}'_{Ha}$. The reluctances of air gaps between shields are $\mathcal{R}_{Hg}$ and $\mathcal{R}'_{Hg}$. Since a RC is being considered, the relative permeability of the non-magnetic former is unity and therefore, air gap reluctance in the cavity of the shielding materials is represented with only one reluctance as $\mathcal{R}_c$. As a result, the shape of the cross-sectional view of a non-magnetic former, whether it is rectangular or circular, will not alter the reluctance of the cavity.

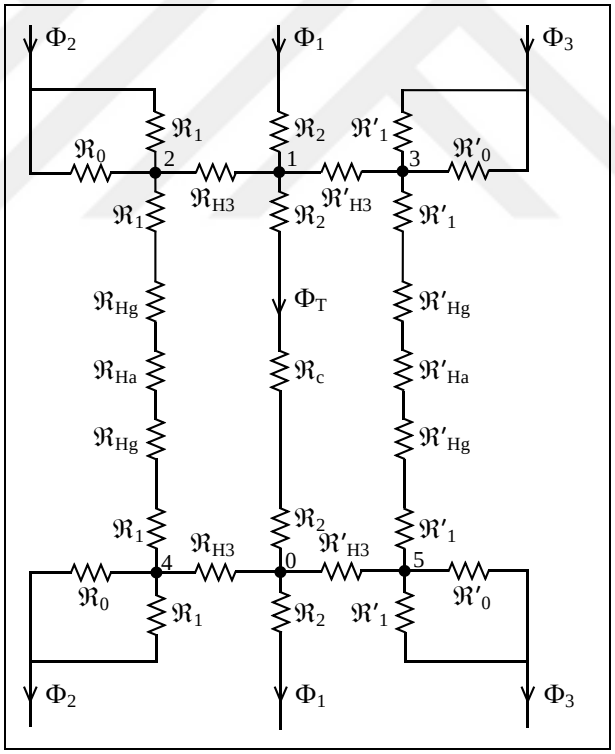

Figure 3.5. Magnetic equivalent circuit for horizontal air gaps

The magnetic circuit model for vertical air gaps is given in Figure 3.6. Some of the reluctances are the same as with the horizontal air gaps model, but because the gaps are vertical, there are also new reluctances in the model given by $\mathcal{R}_4$, $\mathcal{R}'_4$, $\mathcal{R}_{Vg}$, $\mathcal{R}'_{Vg}$, $\mathcal{R}_{V3}$, $\mathcal{R}'_{V3}$, $\mathcal{R}_{Va}$, $\mathcal{R}'_{Va}$.

All of the reluctances for both models in hollow cylindrical structure, as a function of the RC design parameters are indicated in Figure 3.1, are given below.

Cross-sectional area of the inner-shield A_i and outer-shield A_o are

$$A_i = \pi(r_1 + a)^2 - \pi {r_1}^2 \tag{3.27}$$

$$A_o = \pi {r_2}^2 - \pi(r_2 - a)^2 \tag{3.28}$$

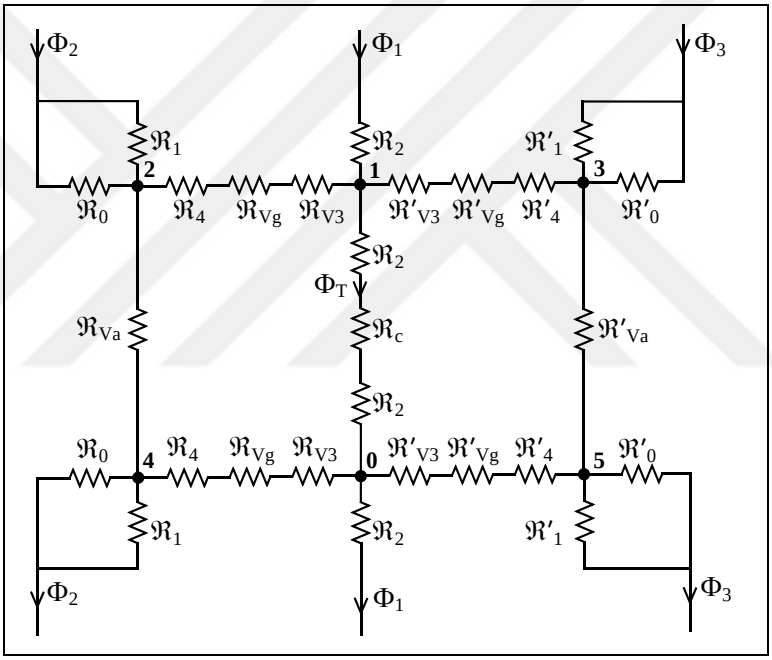

Figure 3.6. Magnetic equivalent circuit for vertical air gaps

The cross-sectional area of the cavity inside shielding A_c is

$$A_c = \pi(r_2 - a)^2 - \pi(r_1 + a)^2 \tag{3.29}$$

Reluctances for the top-shield are written as

$$\mathcal{R}_0 = \frac{1}{\mu\, 2\, \pi\, a} ln \frac{r_1 + a/2}{r_1} \tag{3.30}$$

$$\mathcal{R}_0' = \frac{1}{\mu\ 2\ \pi\ a} ln \frac{r_2}{r_2 - a/2} \tag{3.31}$$

$$\mathcal{R}_1 = \frac{a/2}{\mu\ A_i} \tag{3.32}$$

$$\mathcal{R}_1' = \frac{a/2}{\mu\ A_o} \tag{3.33}$$

$$\mathcal{R}_2 = \frac{a/2}{\mu\ A_c} \tag{3.34}$$

$$\mathcal{R}_{H3} = \frac{1}{\mu\ 2\ \pi\ a} ln \frac{r}{r_1 + a/2} \tag{3.35}$$

$$\mathcal{R}_{H3}' = \frac{1}{\mu\ 2\ \pi\ a} ln \frac{r_2 - a/2}{r} \tag{3.36}$$

Reluctances for air gaps are written as

$$\mathcal{R}_{Hg} = \frac{g}{\mu_0\ A_i} \tag{3.37}$$

$$\mathcal{R}_{Hg}' = \frac{g}{\mu_0\ A_o} \tag{3.38}$$

The reluctance of the inner-shield is

$$\mathcal{R}_{Ha} = \frac{c - 2(a + g)}{\mu\ A_i} \tag{3.39}$$

The outer-shield reluctance is

$$\mathcal{R}_{Ha}' = \frac{c - 2(a + g)}{\mu\ A_o} \tag{3.40}$$

The reluctance of cavity inside shielding $\mathcal{R}_c$ is

$$\mathcal{R}_c = \frac{2b + h}{\mu_0\ A_c} \tag{3.41}$$

The reluctances for vertical air gaps are

$$\mathcal{R}_{Va} = \frac{2b + a + h}{\mu\, A_i} \tag{3.42}$$

$$\mathcal{R}'_{Va} = \frac{2b + a + h}{\mu\, A_o} \tag{3.43}$$

$$\mathcal{R}_{V3} = \frac{1}{\mu\, 2\, \pi\, a} ln \frac{r}{r_1 + a + g} \tag{3.44}$$

$$\mathcal{R}'_{V3} = \frac{1}{\mu\, 2\, \pi\, a} ln \frac{r_2 - a - g}{r} \tag{3.45}$$

$$\mathcal{R}_{Vg} = \frac{1}{\mu_0\, 2\, \pi\, a} ln \frac{r_1 + a + g}{r_1 + a} \tag{3.46}$$

$$\mathcal{R}'_{Vg} = \frac{1}{\mu_0\, 2\, \pi\, a} ln \frac{r_2 - a}{r_2 - a - g} \tag{3.47}$$

$$\mathcal{R}_4 = \frac{1}{\mu\, 2\, \pi\, a} ln \frac{r_1 + a}{r_1 + a/2} \tag{3.48}$$

$$\mathcal{R}'_4 = \frac{1}{\mu\, 2\, \pi\, a} ln \frac{r_2 - a/2}{r_2 - a} \tag{3.49}$$

The flux produced by a vertical magnetic field is separated into three fluxes as ϕ_1, ϕ_2, and ϕ_3 to be able to account for the flux entering from the sides and from the above of top-shield. Flux entering from the sides of inner and outer shields is neglected because of high permeability of shielding material. Therefore, fluxes entering and leaving the shielding are calculated with respect to design parameters as

$$\phi_1 = \mu_0 H_0 [\pi (r_2 - a)^2 - \pi (r_1 + a)^2] \tag{3.50}$$

$$\phi_2 = \mu_0 H_0\, \pi [a(a + 4r_1)] \tag{3.51}$$

$$\phi_3 = \mu_0 H_0 \pi [a(4r_2 - a)] \tag{3.52}$$

3.1.2. Magnetic Circuit Model of Hollow Toroidal Structure for Horizontal Gaps

Magnetic circuit model of hollow toroidal structure for vertical gap is not considered in this study because of difficulties of constructing RCs with vertical gaps. The magnetic circuit model of a hollow toroidal structure of shielding is created by considering the points in the cross-sectional view of the device (see Figure 3.7). Note that the reluctances on the left and the right of the magnetic equivalent circuit are different because of the toroidal structure of the shielding. As an assumption, only one reluctance of the cavity is considered between node 1 and reference node 0 since the top-shield and the bottom-shield reluctances between these points are relatively small with respect to the cavity reluctance.

All of the reluctances for the hollow toroidal structure, as a function of the RC design parameters are indicated in Figure 3.1 and in Figure 3.7, are given below.

Cross-sectional area of the inner and the outer gaps, respectively

$$A_{Tg} = \pi(r - r_3)^2 - \pi(r - r_4)^2 \tag{3.53}$$

$$A'_{Tg} = \pi(r + r_4)^2 - \pi(r + r_3)^2 \tag{3.54}$$

Reluctances of the inner gap and the outer gap are

$$\mathcal{R}_{Tg} = \frac{g}{\mu_0 A_{Tg}} \tag{3.55}$$

$$\mathcal{R}'_{Tg} = \frac{g}{\mu_0 A'_{Tg}} \tag{3.56}$$

The total flux entering from above can be approximated by multiplying flux density with the half of the surface area of the toroid as

$$\phi_1 = \mu_0 H_0 (2\pi^2 r\, r_4) \tag{3.57}$$

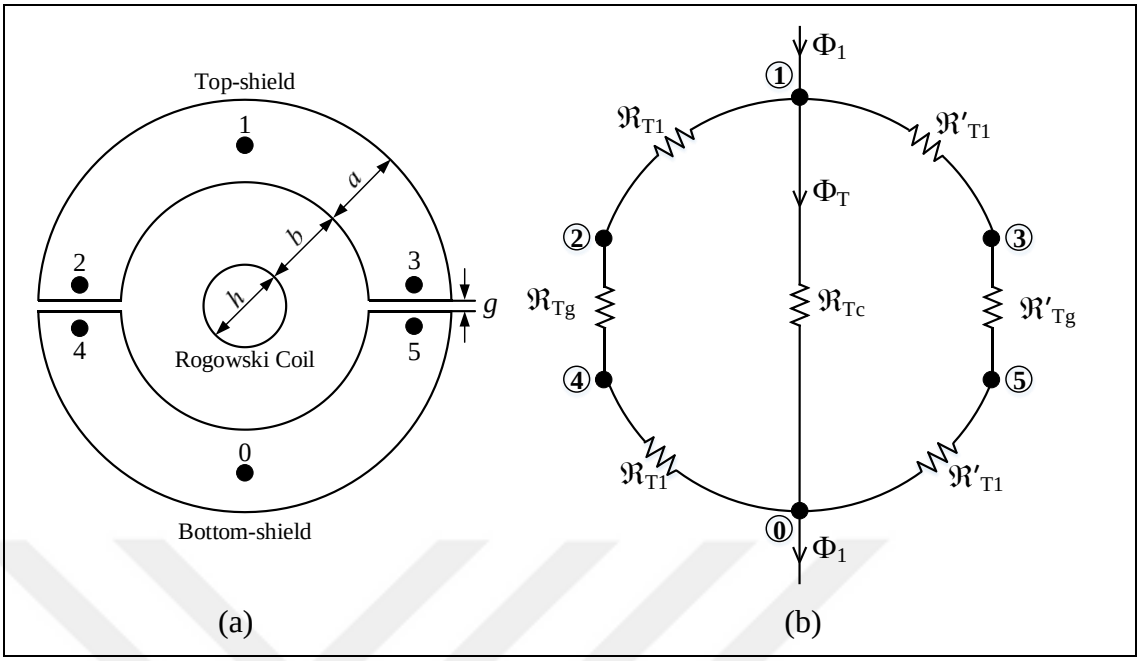

Figure 3.7. Node locations considered for (a) magnetic circuit modeling of hollow toroidal magnetic shielding and (b) its magnetic equivalent circuit

The reluctances $\mathcal{R}_{T1}$ and $\mathcal{R}'_{T1}$ in magnetic equivalent circuit shown in Figure 3.7 is obtained by starting from an infinitely small section of length dr' as shown in Figure 3.8. Note that, differential permeance for angle $d\theta$ is considered first and then, reluctance for corresponding section is calculated.

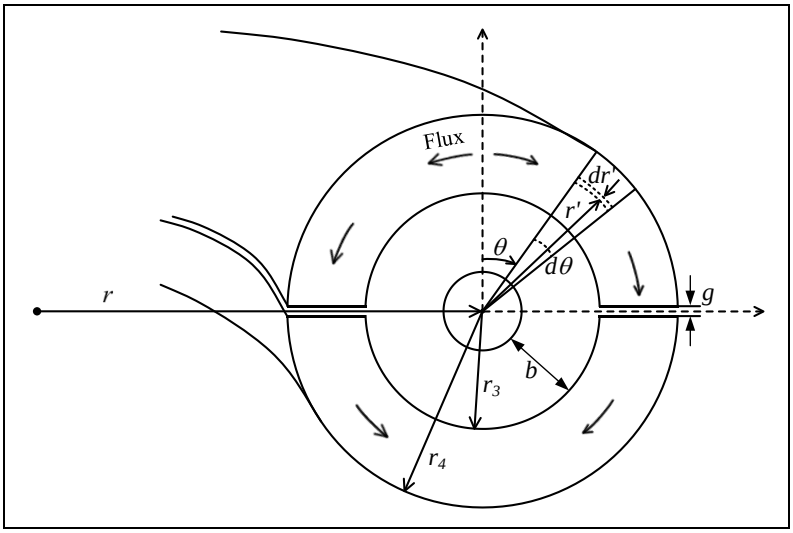

Figure 3.8. The cross-sectional view of hollow toroidal magnetic shielding structure for reluctance calculation

Differential permeance for the angle $d\theta$ can be written as

$$d\mathcal{L} = \int_{r_3}^{r_4} \frac{2\mu\pi(r + r'\,sin\theta)dr'}{r'\,d\theta} = \frac{2\mu\pi\left[r\,ln\frac{r_4}{r_3} + (r_4 - r_3)\,sin\theta\right]}{d\theta} \tag{3.58}$$

Therefore, differential reluctance becomes $d\mathcal{R} = 1/d\mathcal{L}$ and the total reluctance $\mathcal{R}_\theta$ between angle θ_1 and θ_2 is written as

$$\mathcal{R}_\theta = \int_{\theta_1}^{\theta_2} d\mathcal{R} = \int_{\theta_1}^{\theta_2} \frac{d\theta}{2\mu\pi\left[r\,ln\frac{r_4}{r_3} + (r_4 - r_3)\,sin\theta\right]} \tag{3.59}$$

The shielding reluctance $\mathcal{R}_{T1}$ in magnetic equivalent circuit is calculated by integrating Equation (3.59) from $-\pi/2$ to 0 and the reluctance $\mathcal{R}'_{T1}$ from 0 to $\pi/2$ (air gap length is neglected).

The cavity of the hollow toroidal structure has a circular cross-sectional view as shown in Figure 3.9 and it does not have well-defined dimensions for finding its reluctance easily as it is done for the hollow cylindrical structure. Therefore, the reluctance of the cavity can be approximated by assuming a vertical and uniform magnetic field in the cavity. In this case, differential permeance for differential thickness dx for vertical flux at a distance x can be written as

$$d\mathcal{L} = \frac{\mu_0\pi(r + x)dx}{\sqrt{r_3^2 - x^2}} \tag{3.60}$$

The total permeance of the left and the right of vertical axis in Figure 3.9 is not the same since the structure is toroidal, that is, there is no vertical symmetry in terms of permeances. Thus, total permeance can be found by integrating (3.60) from $-r_3$ to $+r_3$ as

$$\mathcal{L} = \int_{-r_3}^{+r_3} \frac{\mu_0\pi(r + x)dx}{\sqrt{r_3^2 - x^2}} = \mu_0\pi^2 r \tag{3.61}$$

The reciprocal of this permeance gives the total reluctance of the cavity as

$$\mathcal{R}_{Tc} = \frac{1}{\mu_0\pi^2 r} \tag{3.62}$$

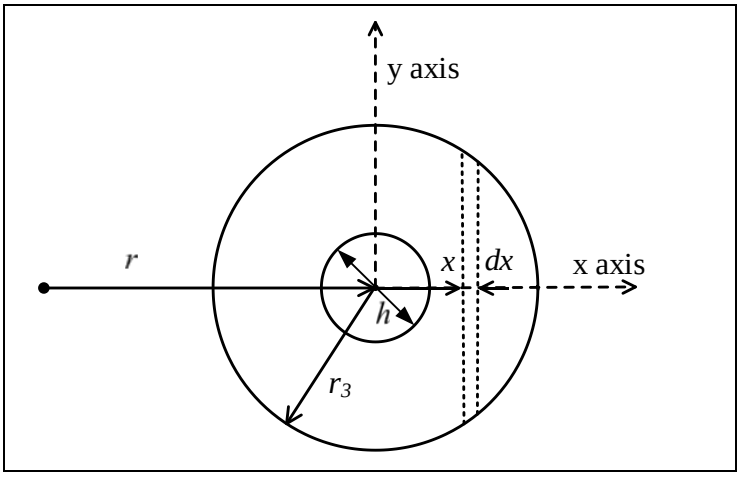

Figure 3.9. The cross-sectional view of the cavity of toroidal structure for reluctance calculation

An interesting result is that the cavity reluctance found above does not depend on the radius of the cavity, that is, no matter how big is the cavity, reluctance will not change. The reluctance of the cavity only depends inversely on the major radius r of the toroid.

3.1.3. Nodal Equations

Nodal equations can be written by using permeances which are the reciprocal of the reluctances and by considering that the total flux of the branches connected to a node must be equal to zero [52] - [53]. Consequently, a flux entering or leaving a node is calculated by multiplying the branch permeance with the magnetomotive force difference between the corresponding nodes where branch is connected. Therefore, the principal diagonal of the permeance matrix will contain the total permeances connected to that specific node as $\mathcal{L}_{ii}$ and off-diagonal permeances will be the negative value of the permeance connected to the corresponding nodes as $-\mathcal{L}_{ij}$ where i ≠ j. Thus, for the magnetic circuits in Figure 3.5, in Figure 3.6 and in Figure 3.7 general nodal permeance matrix is written as

$$\boldsymbol{\mathcal{L}} = \begin{bmatrix} \mathcal{L}_{11} & -\mathcal{L}_{12} & -\mathcal{L}_{13} & 0 & 0 \\ -\mathcal{L}_{12} & \mathcal{L}_{22} & 0 & -\mathcal{L}_{24} & 0 \\ -\mathcal{L}_{13} & 0 & \mathcal{L}_{33} & 0 & -\mathcal{L}_{35} \\ 0 & -\mathcal{L}_{24} & 0 & \mathcal{L}_{44} & 0 \\ 0 & 0 & -\mathcal{L}_{35} & 0 & \mathcal{L}_{55} \end{bmatrix} \tag{3.63}$$

Since flux vector and nodal permeance matrix are known, magnetomotive force of all nodes with respect to the reference is calculated by

$$\mathbf{F} = \boldsymbol{\mathcal{L}}^{-1}\,\boldsymbol{\Phi} \tag{3.64}$$

where $\boldsymbol{\Phi} = [\phi_1 \quad \phi_2 \quad \phi_3 \quad -\phi_2 \quad -\phi_3]^T$ is the source flux vector for the hollow cylindrical structure and $\boldsymbol{\Phi} = [\phi_1 \quad 0 \quad 0 \quad 0 \quad 0]^T$ for the hollow toroidal structure, and $\mathbf{F} = [\mathcal{F}_1 \quad \mathcal{F}_2 \quad \mathcal{F}_3 \quad \mathcal{F}_4 \quad \mathcal{F}_5]^T$ is the node magnetomotive force vector for both. Here, node number zero is taken as the reference. From (3.64), individual fluxes in the branches of a magnetic circuit are easily obtained. For example, the flux in the cavity of the shielding is calculated by

$$\phi_T = \mathcal{L}_{10}\mathcal{F}_1 \tag{3.65}$$

where $\mathcal{L}_{10}$ is the permeance of the branch between node 1 and node 0.

Additionally, the magnetic field intensity values are found by using the relationship given by $Hl = \mathcal{R}\phi = \mathcal{F}$. Thus, for the cavity of the shielding, the magnetic field intensity value after magnetic shielding is applied is given by

$$\bar{H}_T = \frac{\mathcal{F}_1}{\bar{l}} \tag{3.66}$$

where $\bar{H}_T$ is the average magnetic field intensity and $\bar{l}$ is the average length of the cavity. The average length of the cavity for the hollow cylindrical magnetic shielding is the distance between the top-shield and the bottom-shield as shown in Figure 3.4, and given by $\bar{l} = h + 2b$, whereas for the hollow toroidal shielding as shown in Figure 3.7, the average length is given by $\bar{l} = (\pi/4)(h + 2b)$.

As a result, the magnetic shielding effectiveness is calculated by using Equations (3.1) and (3.66) where $\bar{H}_0$ is the average uniform magnetic field intensity before applying shielding for the RCs.

The magnetic circuit model proposed may be slightly more complicated than the analytical solution given in the literature since a 5×5 matrix is involved, but the accuracy is considerably better for the range of parameters studied.

3.2. FEM ANALYSIS

In order to validate the proposed magnetic circuit approaches in Chapter 3.1, simulation studies have been done to calculate magnetic shielding effectiveness of hollow cylindrical and toroidal structures for changes in parametric space by using *ANSYS-Maxwell* software licensed to Yeditepe University.

3.2.1. ANSYS-Maxwell Software

Simulation studies for the analysis of effectiveness of the magnetic shield have been performed by the *ANSYS-Maxwell* which is the premier electromagnetic field simulation software for low-frequency analysis and design of devices such as sensors, machines, actuator, and coils. The *ANSYS-Maxwell* software uses FEM to solve electric and magnetic problems in devices. In FEM, the problem which requires the solution of boundary values for partial differential equations is converted to a system of algebraic equations that give approximate values at the discrete number of points. The solution accuracy can be controlled by minimizing an associated error function as a result of altering the number of discrete points used.

In *ANSYS-Maxwell*, the geometry of the model discretized into a large number of small regions of triangular pyramids called tetrahedrons in 3D [54]. The assembly of all tetrahedrons constitutes a mesh which also referred to as the finite element mesh. Increasing the mesh resolution by decreasing the size of each tetrahedron improves the accuracy of the solution. Since using high numbers of tetrahedrons require the solution of large number of algebraic equations, the accuracy of the solution will be limited by the memory capacity of the computer used. Therefore, the accuracy of *ANSYS-Maxwell* simulation result is directly related to the number of mesh components used, the size of 3D region under consideration, and the complexity of the problem. For simulations, the hardware used is Intel® Core™ i7 (2.4 GHz, 16 GB RAM) with 64-bit operating system.

ANSYS-Maxwell has three different solvers which are magnetostatic, eddy current and transient magnetic. The magnetostatic solver computes static magnetic fields caused by DC currents and permanent magnets for linear and non-linear materials. Eddy current solver is

used for simulating time-varying magnetic fields in the frequency domain to resolve skin depths and proximity effects within objects. The transient magnetic solver calculates transient magnetic fields produced by time-varying or moving electrical sources and permanent magnets.

During the simulation of RC and effectiveness of shielding, *ANSYS-Maxwell*'s magnetostatic solver is used because a constant magnitude external field is considered for the analysis of magnetic shielding effectiveness.

In *ANSYS-Maxwell*'s magnetostatic solver, the adaptive meshing technique is utilized in order to generate a quality mesh. A first solution has been found with a rough mesh in the adaptive meshing technique and then the mesh is refined with progressively smaller tetrahedral meshes. Once the target error value set by the user has been reached, the solution for the problem is attained. The minimum target error that can be reached depends on the memory capacity of the computer used. Therefore, during simulation studies, the minimum target error has been always pursued by utilizing the capabilities of the computer used.

In magnetostatic solver, the adaptive mashing technique is applied by subdividing the elements with the highest energy error until the energy percent error and the delta percent energy are below the target percent error specified by the user. The mechanism for evaluating error in magnetostatic solver may be to use Curl H to find the current density and then subtracting this value from all input currents and sources. In an ideal case, the solution must be zero, but because of discretization of the problem and finite mesh, a numerical solution will have a slight error leading to a residual current density. An energy error value is calculated from this residual current density. The energy percent error is the ratio of energy error to total energy calculated from all original sources.

$$Percent\ energy\ error\ (\%) = \ Error\ Energy / Total\ Energy \times 100 \tag{3.67}$$

For adaptive mesh calculations, if more than one pass is completed, the change in total energy between consecutive passes is calculated. Then, the percent difference is called as delta percent energy.

3.2.2. Modeling of FEM Simulation

Simulation studies are done by creating a uniform magnetic field region which represents an external vertical magnetic field where the non-magnetic RC former and the magnetic shield will be placed in the center. The geometry of the region is built by using the drawing bar in the toolbar of *ANSYS-Maxwell*. The region is a rectangular prism box with a width of 800 mm, a depth of 800 mm and a height of 600 mm. The material property of the region is selected as an air.

The uniform constant magnetic field intensity is created in the region by assigning the boundary condition to side faces of the region as the *Tangential H-Field* by defining the direction of vectors in the negative *z*-direction and then by assigning the boundary conditions to the top and bottom faces of the region as the *Zero Tangential H-Field*. A uniform magnetic field intensity of 1000 A/m in the negative *z*-direction is used in all simulations to be comparable with the literature in this section as shown in Figure 3.10.

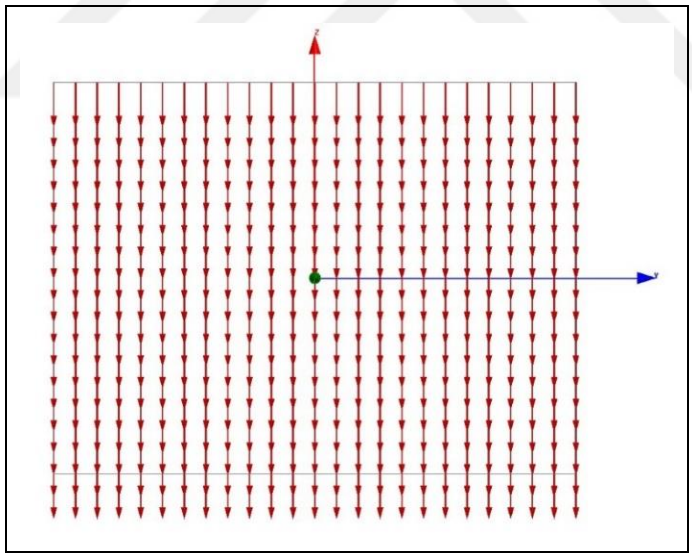

Figure 3.10. Representation of uniform vertical external magnetic field region

To simulate the non-magnetic former of RC, the toroidal ring core with the dimensions of 170 mm in inner diameter, 190 mm in outer diameter and 10 mm in height was built and placed in the center of the region. The symmetrical cylindrical structure of non-magnetic RC former has been explored for effective usage of computer memory. As previously described, a minimum target error was obtained by increasing mesh numbers in the structure. However,

the mesh numbers in the structure limited by the memory capacity of the computer. By using one-eighth of the toroidal ring core, it was possible to increase mesh numbers considerably, and therefore a better solution for the simulation has been achieved.

Solving of one-eighth of structure in *ANSYS-Maxwell* is performed by dividing the structure into XY, YZ and XZ planes using the split window in *ANSYS-Maxwell* and then by assigning the boundary of each plane to the *Symmetry Boundary*. The critical point for the assigning of boundaries is the selection of the symmetry boundaries of YZ and XZ planes as the *Flux Tangential* and the symmetry boundary of the XY plane as the *Flux Normal*.

Relationships among target errors, mesh numbers and computed average magnetic field intensity values were investigated by applying two different mesh operations offered by *ANSYS-Maxwell*; *adaptive meshing* and *inside selection/length based*. The permeability of the toroidal ring core was selected as 8000 here. Simulation results using the *adaptive meshing operation* are given in Table 3.1. In this table, it is clearly seen that the refinement steps by the *adaptive meshing operation* for smaller target errors increase the accuracy of average magnetic field intensity value in the negative z-direction. Also, it is noticeable that the difference in average magnetic field intensity value decreases in consecutive steps indicating the convergence. At the thirty-seventh steps in, a target error of 0.0000032 percent is achieved with 2033286 total mesh numbers, and as a result, the average magnetic field intensity value in the toroidal core becomes 28.262 mA/m just before the memory capacity limit of the computer is reached.

Figure 3.11. shows target errors with respect to the refinement steps (i.e. pass number) for the adaptive mesh operation. After the twenty-fifth steps, the difference between the consecutive target errors is very small. This means that the target error is converged to 0.0000032 percent and is close to zero with the memory capacity of available computer.

Table 3.1. Simulation data for the steps of adaptive meshing operation

Pass	Target Error	Total Mesh Numbers			Average *H* Values
	(%)	Core	Region	Total	(mA/m)
1	0.1404800	37	108	145	82.669
2	0.0091830	37	154	191	67.148
3	0.0048289	37	215	252	59.656
4	0.0045142	37	295	332	58.976
5	0.0044429	37	402	439	46.937
6	0.0043438	37	538	575	42.844
7	0.0043063	37	718	755	39.480
8	0.0044182	37	953	990	38.116
9	0.0040946	47	1247	1294	34.465
10	0.0031792	52	1633	1685	31.954
11	0.0028341	66	2131	2197	31.544
12	0.0027183	89	2772	2861	30.789
13	0.0024937	144	3583	3727	30.400
14	0.0018747	197	4653	4850	30.088
15	0.0013748	323	5987	6310	29.530
16	0.0009892	532	7675	8207	29.266
17	0.0008044	786	9890	10676	29.048
18	0.0005792	1051	12835	13886	28.838
19	0.0004321	1599	16463	18062	28.694
20	0.0003486	2397	21090	23487	28.584
21	0.0002576	3212	27326	30538	28.511
22	0.0002049	4615	35089	39704	28.449
23	0.0001623	6641	44980	51621	28.407
24	0.0001240	8877	58238	67115	28.373
25	0.0000915	12032	75222	87254	28.345
26	0.0000743	17161	96273	113434	28.325
27	0.0000569	22940	124528	147468	28.310
28	0.0000429	30040	161678	191718	28.298
29	0.0000332	41087	208154	249241	28.288
30	0.0000255	55047	268971	324018	28.281
31	0.0000187	72065	349166	421231	28.276
32	0.0000145	95977	451629	547606	28.271
33	0.0000105	123969	587924	711893	28.268
34	0.0000078	162914	762555	925469	28.266
35	0.0000060	212376	990740	1203116	28.264
36	0.0000044	276947	1287114	1564061	28.263
37	0.0000032	358987	1674299	2033286	28.262

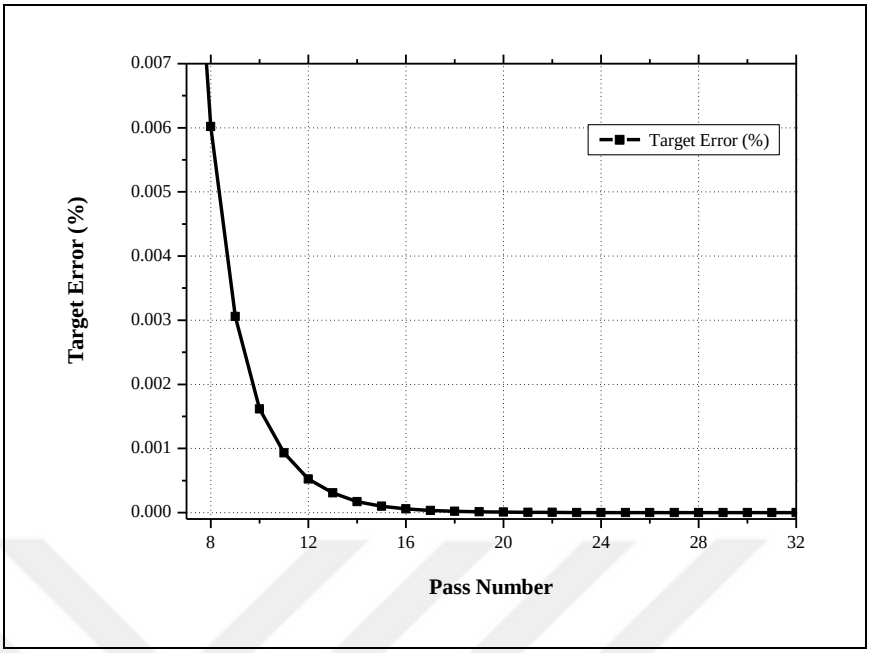

Figure 3.11. Convergent of target error in the adaptive mesh operation

As can be seen in Figure 3.12, the mesh numbers become intense in the regions near the corners of the toroidal ring core when the *adaptive mesh operation* is used. The edge lengths of tetrahedrons are automatically minimized by *ANSYS-Maxwell* in these regions. This means that the *adaptive meshing operation* concentrates on the critical points of the model to have accurate simulation results.

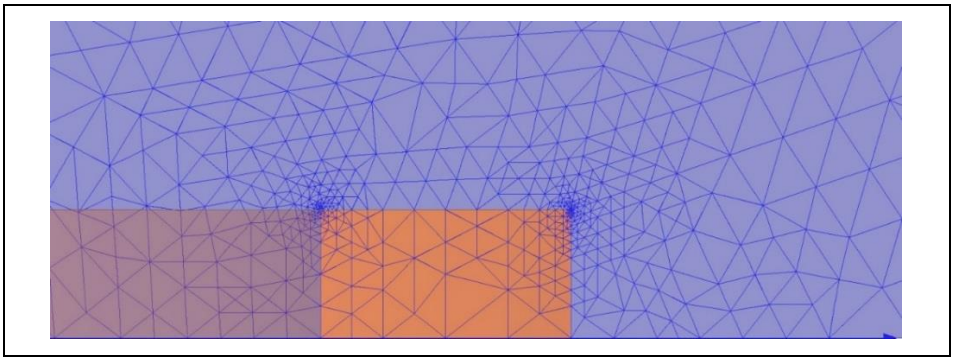

Figure 3.12. Mesh distribution of toroidal ring core without the magnetic shield

Since the material of magnetic shielding cores is a magnetic alloy with high initial permeability and magnetic materials are attractive for magnetic field vectors, the magnetic field intensity distribution is not uniform inside and around the toroidal ring core as shown in Figure 3.13. The magnetic field intensity values around the toroidal ring core are higher

than the applied magnetic field intensity value of 1 kA/m and especially the values at the corner of the toroidal ring core approximately increase to 3 kA/m. Further investigation about magnetic field intensity distribution in the toroidal ring core and around will be carried out.

Table 3.2. Simulation data for the steps of inside selection/length based mesh operation

Pass	**Target Error**	**Total Mesh Numbers**			**Average H Values**
	(%)	**Core**	**Region**	**Total**	**(mA/m)**
1	0.000810	258026	25997	284023	28.675
2	0.000106	259357	109879	369236	28.300
3	0.000061	262604	217412	480016	28.247
4	0.000038	271609	352421	624030	28.227
5	0.000027	292234	519009	811243	28.214
6	0.000017	324031	730591	1054622	28.206
7	0.000012	373480	997539	1371019	28.201

Similar simulations were repeated for the investigation of the effect of the *inside selection/length* based mesh operation. The *inside selection/length* based operation limits the edge length of all the tetrahedrons formed inside a selected object. The inside selection/length based mesh operation was applied to the toroidal ring core. The maximum length of tetrahedrons formed inside in the toroidal ring core performed was limited to 1 mm. In this mesh operation, the mesh numbers inside the toroidal ring core started with high numbers and slightly increased with the next iteration in the *adaptive mesh operation*. The computed results are tabulated in Table 3.2. At the seventh step in Table 3.2, the convergent value of magnetic field intensity is computed around 28.201 mA/m.

This slight difference between the average magnetic field intensity values obtained by using two different mesh operations can be overlooked. However, while the target error of 0.000012 percent is obtained in the simulation with 1371019 total mesh numbers using the *inside selection/length* based operation; the target error of 0.0000032 percent is achieved with 2033286 total mesh numbers when adaptive mesh operation is used.

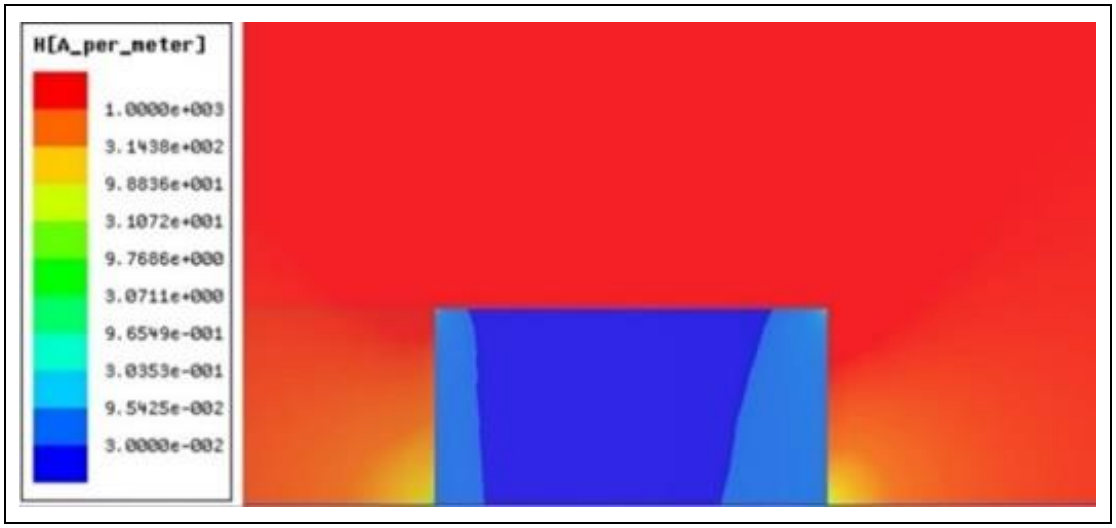

Figure 3.13. Magnetic field intensity distribution near the toroidal ring core

The mesh distribution and the magnetic field intensity distribution when *inside selection/length based mesh operation* is used show similar characteristics with the adaptive mesh operation shown in Figure 3.12 and Figure 3.13. However, the *adaptive mesh operation* in *ANSYS-Maxwell*'s magnetostatic solver is preferred during the simulation of the toroidal ring core with and without the magnetic shielding because better minimum target errors and more accurate simulation results are achieved.

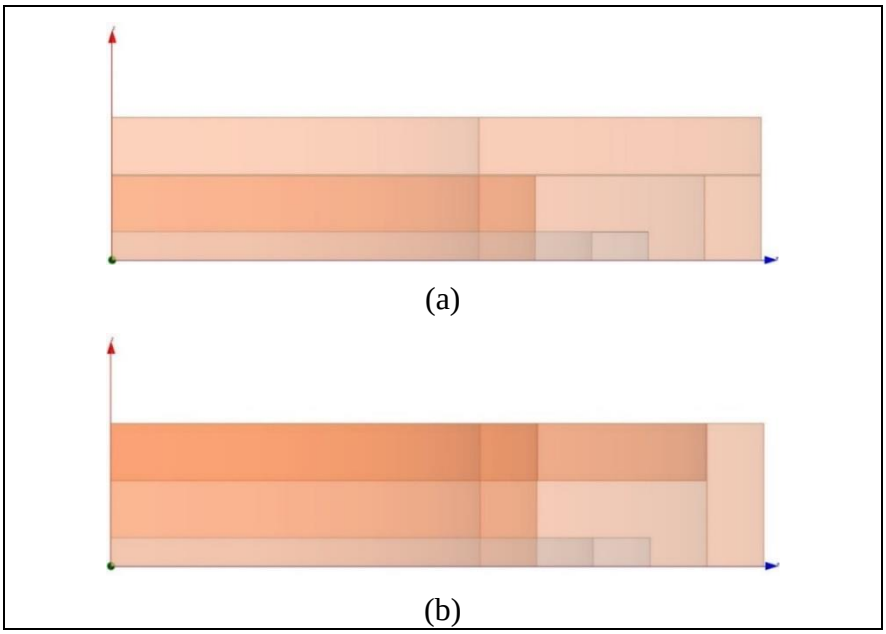

Figure 3.14. One-eighth of magnetic shield with (a) horizontal air gap and (b) vertical air gap

The magnetic shields with horizontal and vertical air gaps were built by surrounding the non-magnetic RC former for the analysis of magnetic shielding effectiveness in Rogowski coil. As described in Chapter 3.1, the magnetic shield consists of four tape wound toroidal magnetic cores in the shape of hollow toroid. These magnetic cores are placed at the top, bottom, inside and outside of the non-magnetic RC former. One-eighth presentations of magnetic shield configurations for the horizontal air gap and the vertical air gap are shown in Figure 3.14.

The developed mesh density and magnetic field distributions were analyzed by *ANSYS-Maxwell*'s post-processing to review the simulation results in the magnetic shielded RC with a horizontal and a vertical air gap. Figure 3.15 shows that the mesh numbers at the corners of the magnetic shield and especially around the horizontal air gaps are intense. In addition to that, the magnetic field intensity values in the magnetic shield are very high (> 1.5 kA/m) in these regions shown in Figure 3.16.

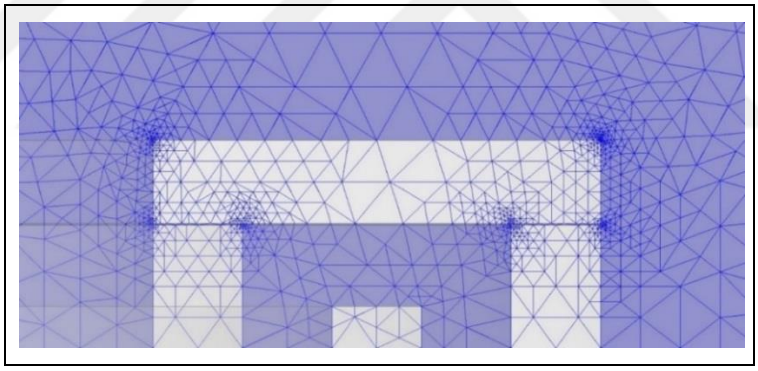

Figure 3.15. Mesh distribution of the magnetic shield with horizontal air gap

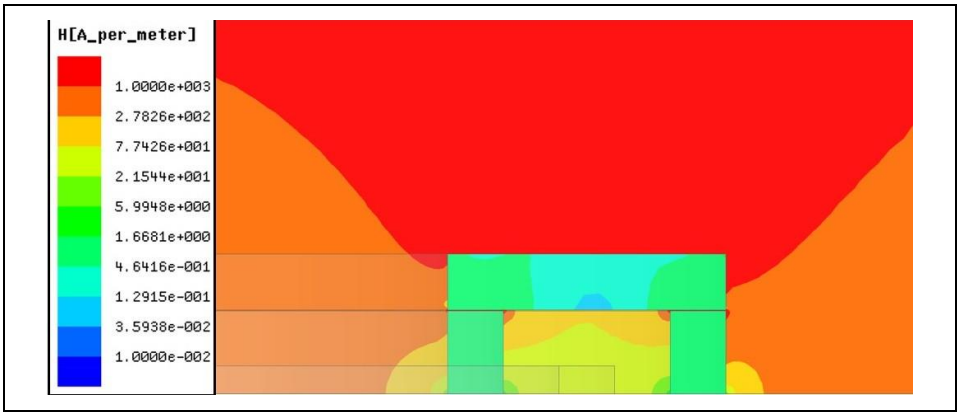

Figure 3.16. Magnetic field distribution of magnetic shield with horizontal air gap

The magnetic field vectors are shown in Figure 3.17 to indicate the non-uniformity of the magnetic field between the inner-shield and outer-shield. The magnetic field vectors are intense at the corners of the magnetic shield and especially around the horizontal air gaps. The magnetic field vectors penetrate the magnetic shield not only from the top surface of the top-shield but also from the sides of the top-shield, the interior surface of inner-shield and the exterior surface of outer-shield.

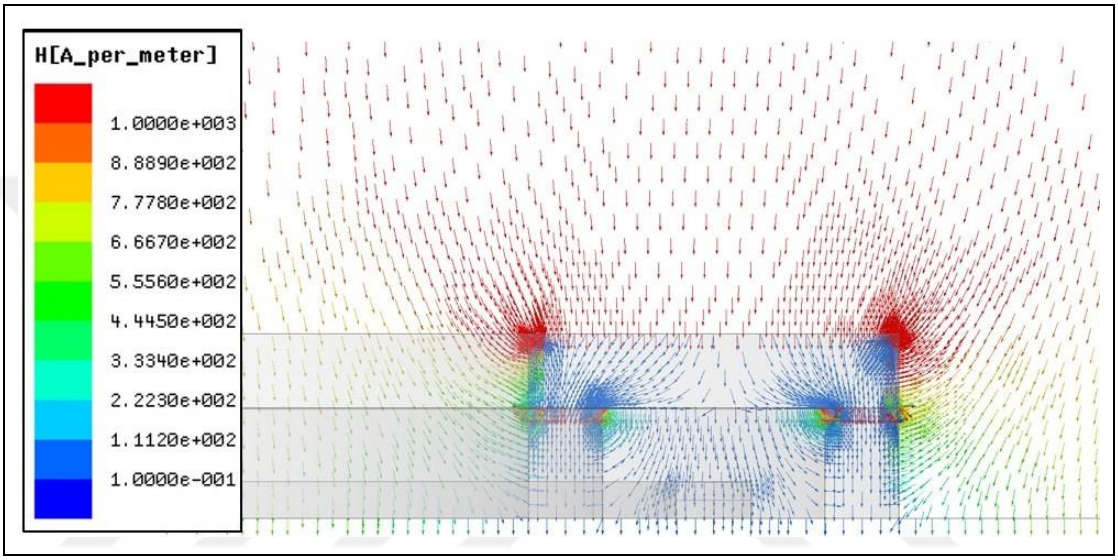

Figure 3.17. Magnetic field vectors for the magnetic shield with horizontal air gap

The mesh density for the magnetic shielded RC with a vertical air gap is shown in Figure 3.18. Similar mesh density is occurred at the corners of the magnetic shield and around the vertical air gaps as a horizontal air gap arrangement due to the selection of adaptive mesh operation in *ANSYS-Maxwell*.

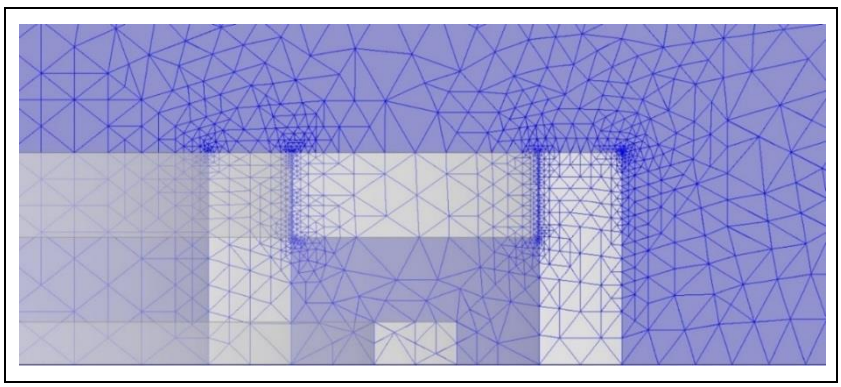

Figure 3.18. Mesh distribution of magnetic shield with vertical air gap

The *H*-field distribution for the magnetic shielded RC with vertical air gap is shown in Figure 3.19.

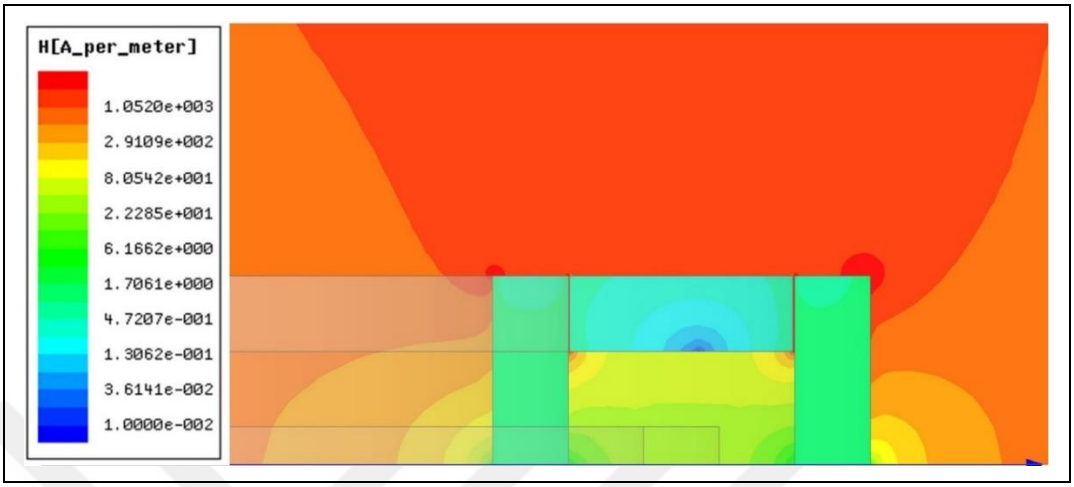

Figure 3.19. Magnetic field distribution of magnetic shield

3.2.3. Magnetic Field Distribution Inside Magnetic Shield for RC

Since a magnetic field intensity with and without magnetic shielding may change from point to point in general, a shielding effectiveness value will depend on the location of the points in the shielding cavity. The magnetic field intensity values at various points in the non-magnetic RC former and in the cavity of magnetic shielding with horizontal air gaps were calculated by *ANSYS-Maxwell* for observation of these changes. And then, magnetic shielding effectiveness was computed by using Equation (1.1) for each point.

The shielding effectiveness were first calculated with average magnetic field intensity values of the non-magnetic RC former by using the field calculator tool of *ANSYS-Maxwell* with the following command "/(Integrate(Volume(Non-magnetic RC former), Mag(<Hx,Hy,Hz>)), Integrate(Volume(Non-magnetic RC former), 1))".

Besides, three lines were placed in non-magnetic RC former. The top line was kept 0.1 mm away from the top surface of the non-magnetic RC former to avoid unexpected changes on the boundary. The middle line was located between the top surface of the non-magnetic RC former and its center. The bottom line was located in the center of non-magnetic RC former. The line named the cavity line was placed in the middle of the magnetic shield cavity. These

lines are shown in Figure 3.20. Since the cylindrical magnetic shield has a symmetrical structure, these lines were only placed at the upper half of the shielding structure. Similar results will be available at the other half of the shielding structure. Magnetic shielding effectiveness was separately calculated at 1000 points on each lines where are from 0 mm to 10 mm by 0.01 mm steps.

For these studies, the thickness parameter a and the shielding distance parameter b in the hollow cylindrical magnetic shielding structures were 10 mm. Gap distance was kept constant at 0.2 mm and relative permeability of the toroidal shielding material was chosen as 4000. One-eighth of the toroidal magnetic shield structure is simulated by using the adaptive mesh operation. During the simulation process, maximum pass numbers are pursued to reach the lowest target error that the computer could be able to achieve.

Magnetic field intensity values of all points were constant and 1000 A/m before the magnetic shield. The magnetic field intensity values in the regions close to the interior and exterior surfaces of the non-magnetic RC former became higher than values in the central region with applying of magnetic shield since the toroidal magnetic shielding cores have high permeabilities.

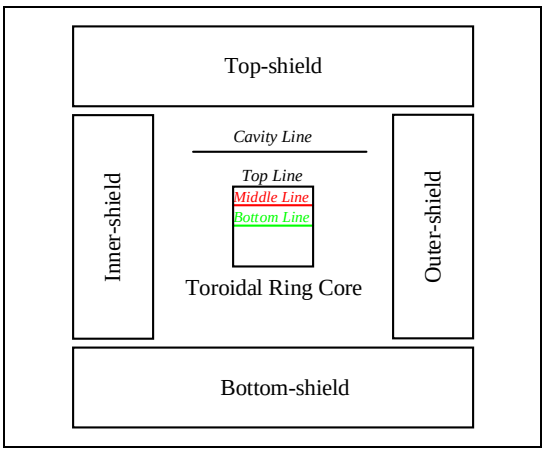

Figure 3.20. Lines for H calculation in the non-magnetic RC former

The line graph in Figure 3.21 presents the distributions of magnetic field intensity on the top, bottom and middle lines in which to be seen their average, minimum and maximum values with the magnetic shield application. Likewise, the distributions of the shielding effectiveness on these lines are shown in Figure 3.22. As clearly seen in Figure 3.22, the magnetic shielding effectiveness values are not constant inside the non-magnetic RC former.

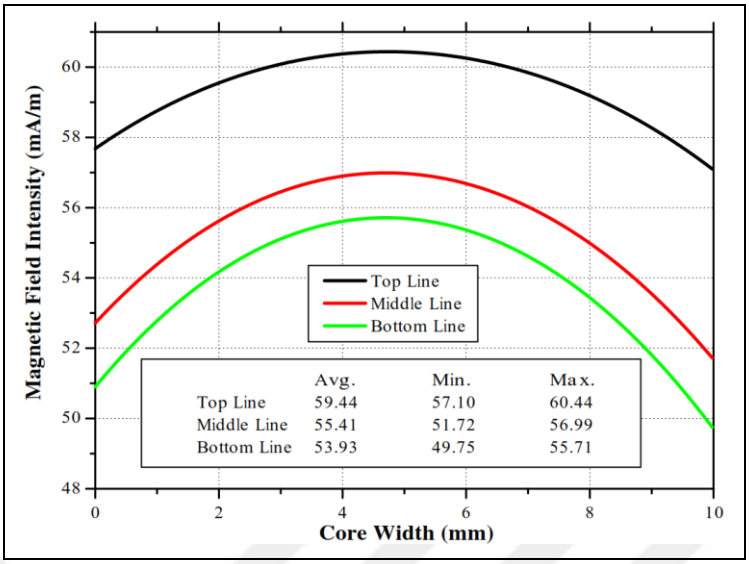

Figure 3.21. *H*-Field values through lines with magnetic shield for RC

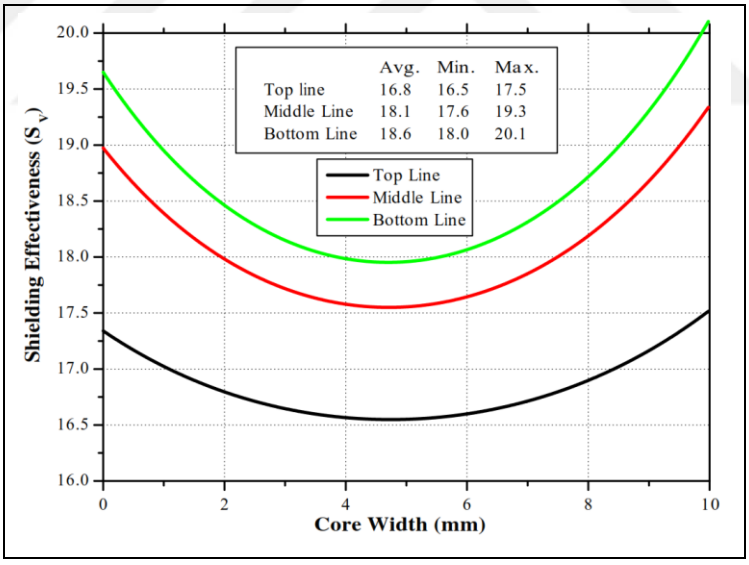

Figure 3.22. Shielding effectiveness values through lines for RC

The distribution of magnetic field intensity on the cavity line is displayed in Figure 3.23 with average, minimum and maximum values, whilst the magnetic shielding effectiveness distribution on this line is shown in Figure 3.24. The shielding effectiveness values on the cavity are not constant as the lines inside the non-magnetic RC former.

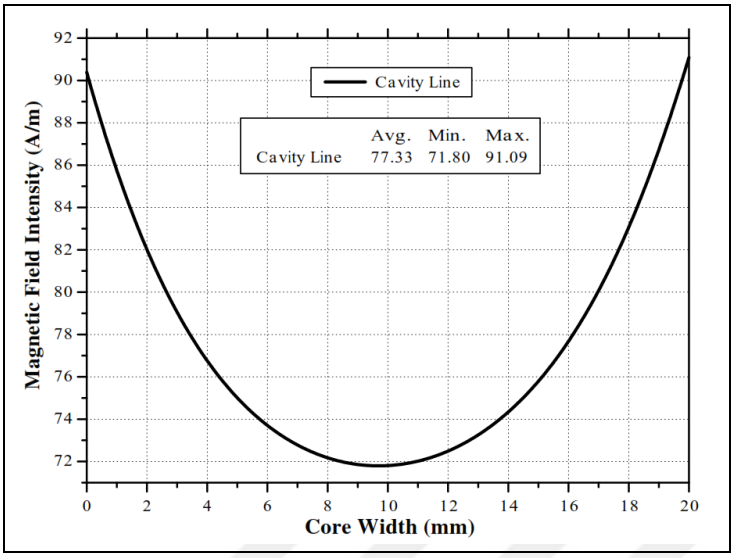

Figure 3.23. *H*-Field values through cavity line with magnetic shield for RC

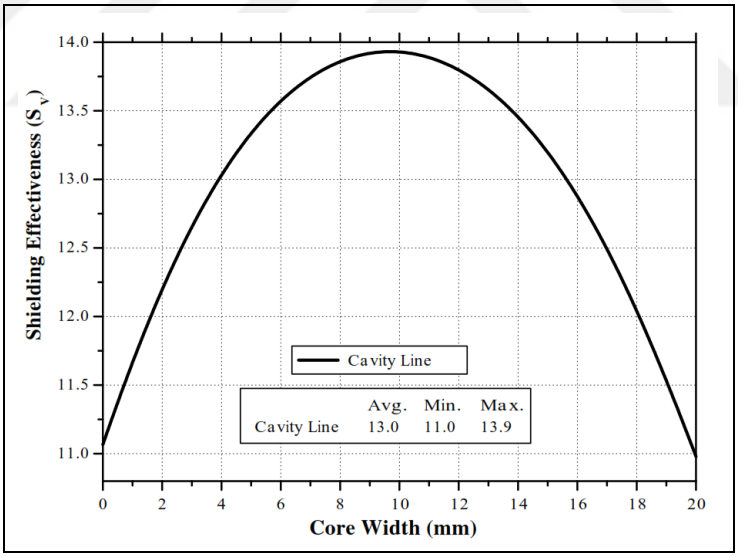

Figure 3.24. Shielding effectiveness values through cavity line for RC

The reason of this change can be explained as applying magnetic shielding may alter the magnitudes and directions of magnetic field intensity vectors differently at each point. Therefore, the averages of the magnetic field intensities in the non-magnetic former before and after applying magnetic shielding are used to calculate shielding effectiveness in the FEM simulations.

3.3. VERIFICATION OF PROPOSED MODELS

The proposed magnetic circuit models for the calculation of magnetic shielding effectiveness is verified by using the FEM simulations by changing the thickness parameter a and the shielding distance parameter b in the hollow cylindrical and the hollow toroidal magnetic shielding structures. For these studies, gap distance is kept constant at 0.2 mm and relative permeability of the shielding material is chosen as 4000. This value of the relative permeability for the magnetic shields is selected to be similar to the literature for the comparisons reason. Moreover, the effect of the relative permeability to the magnetic shielding effectiveness has also been investigated by varying its value between 1000 and 100000 for specified dimensions of shielding.

In simulation studies, axial symmetry in 2D is used instead of 3D to utilize the memory capacity of the computer, reduce the simulation duration and to minimize the energy percent error. Cares have been taken to make sure that the energy percent error in *ANSYS-Maxwell* converged to a very small number so that the results of simulations are reliable.

3.3.1. Results for Hollow Cylindrical Structure

Magnetic shielding effectiveness values for the magnetically shielded RC obtained by the FEM simulations and calculated by the magnetic circuit model are shown in Table 3.3 for horizontal air gaps. The shielding thickness and the distance are varied between 5 mm and 30 mm with steps of 5 mm. In Table 3.3, the numbers shown in bold font are the solutions of the FEM simulations, the numbers with normal font are the proposed magnetic circuit results, and the numbers below these two are the percentile relative errors.

The maximum percent relative error for the range considered is 27 percent as shown in Table 3.3 for $a = 15$ mm and $b = 30$ mm. It can be seen that the magnetic circuit model gives slightly higher magnetic shielding effectiveness values when compared to the FEM results.

The analytical formula for horizontal air gaps given by (3.23) has higher relative errors with respect to the range considered. The percentage error of magnetic shielding effectiveness, calculated from the analytical formula given by (3.66) and from the proposed magnetic circuit approach, are illustrated in Figure 3.25 when the magnetic shielding thickness and

the distance from non-magnetic former are varied from 5 mm to 30 mm. The surface above in Figure 3.25 shows the percentage error of the analytical equation with the minimum error of 37 percent and the maximum error of 86 percent, whereas, the surface below shows the percentage error of the proposed magnetic circuit approach with the minimum of 8 percent and the maximum of 27 percent. The relative error increases considerably when the shielding thickness is increased in (3.23), showing that the thickness is not well represented. Figure 3.25 clearly shows that the proposed magnetic circuit approach gives better results.

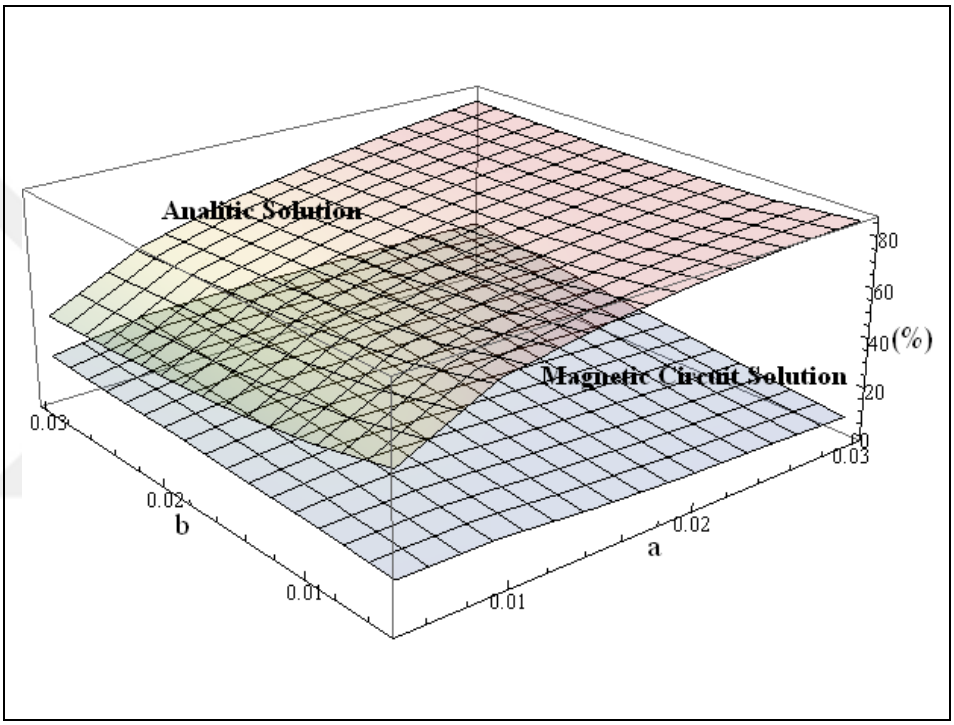

Figure 3.25. The percentage error of magnetic shielding effectiveness of the analytical solution and the proposed magnetic circuit approach

Table 3.4 shows the magnetic shielding effectiveness values for FEM simulations (in bold), for the proposed magnetic circuit model, and relative percent error results for vertical air gaps. In Table 3.4, the maximum and the minimum relative errors between the proposed magnetic circuit model and FEM simulations are 17 percent and 5 percent, respectively. It is noticeable that the relative errors are lower than that of horizontal air gaps for the range considered because, in this case, the gaps are parallel to the external magnetic field. However, similar to horizontal air gaps, the magnetic circuit model gives slightly higher values than the FEM simulations for vertical air gaps.

Table 3.3. Influences of (a) and (b) on magnetic shielding effectiveness for horizontal air gaps r = 90 mm, g = 0.2 mm

***a\b* (mm)**	**5**	**10**	**15**	**20**	**25**	**30**
5	**11.0**	**12.9**	**14.1**	**14.8**	**15.3**	**15.7**
	12.7	15.1	16.6	17.6	18.2	18.7
	16%	17%	18%	19%	19%	20%
10	**14.4**	**17.9**	**20.2**	**21.8**	**22.9**	**23.8**
	16.6	21.1	24.4	26.8	28.6	30.0
	15%	18%	21%	23%	25%	26%
15	**16.5**	**21.1**	**24.3**	**26.7**	**28.5**	**29.8**
	18.5	24.4	29.0	32.6	35.5	37.8
	12%	16%	19%	22%	25%	27%
20	**17.8**	**23.3**	**27.3**	**30.3**	**32.6**	**34.4**
	19.6	26.5	32.1	36.7	40.4	43.5
	10%	14%	18%	21%	24%	27%
25	**18.7**	**24.9**	**29.5**	**33.1**	**35.8**	**37.9**
	20.4	27.9	34.2	39.6	44.0	47.9
	9%	12%	16%	20%	23%	26%
30	**19.4**	**26.1**	**31.2**	**35.2**	**38.3**	**40.7**
	20.9	28.9	35.8	41.7	46.8	51.2
	7%	11%	15%	19%	22%	26%

Magnetic shielding effectiveness does not change significantly for vertical air gaps when the distance between non-magnetic former and shielding is changed, but the thickness of shielding has considerable effect as seen in Table 3.4. The analytical formula for vertical air gaps given by (3.24) produces high relative errors when compared to the FEM simulation results. For example, the relative error is -37 percent at $a = 30$ mm and $b = 5$ mm and 78 percent at $a = 5$ mm and $b = 30$ mm.

The proposed magnetic circuit model is also validated for changes in air gap g, in relative permeability of the shielding material μ_r, and the radius of a hollow cylindrical structure r. Analyses are carried out by keeping magnetic shielding thickness and shielding distance constant at 10 mm.

In Figure 3.26, magnetic shielding effectiveness is shown when air gaps are varied from 0.2 mm to 1.5 mm for r = 90 mm. The differences between the magnetic circuit model and the FEM simulation for both horizontal (maximum relative error 19 percent for g = 0.2 mm) and vertical air gaps (maximum relative error -15 percent for g = 1.5 mm are comparable.

Table 3.4. Influences of (a) and (b) on magnetic shielding effectiveness for vertical air gaps r = 90 mm, g = 0.2 mm

***a\b* (mm)**	**5**	**10**	**15**	**20**	**25**	**30**
5	**23.5**	**23.4**	**23.1**	**22.7**	**22.4**	**22.0**
	24.9	24.6	24.3	24.1	23.8	23.5
	6%	5%	5%	6%	6%	7%
10	**42.9**	**42.8**	**42.1**	**41.4**	**40.6**	**39.8**
	47.5	47.1	46.7	46.2	45.7	45.2
	11%	10%	11%	12%	13%	14%
15	**61.4**	**61.3**	**60.5**	**59.4**	**58.3**	**57.1**
	68.6	68.4	67.9	67.3	66.6	66.0
	12%	12%	12%	13%	14%	16%
20	**78.8**	**78.9**	**77.9**	**76.6**	**75.2**	**73.7**
	87.9	88.2	87.9	87.3	86.6	85.8
	12%	12%	13%	14%	15%	16%
25	**95.0**	**95.5**	**94.4**	**92.9**	**91.2**	**89.5**
	105.4	106.6	106.6	106.1	105.4	104.6
	11%	12%	13%	14%	16%	17%
30	**110.0**	**111.0**	**109.9**	**108.3**	**106.4**	**104.4**
	121.1	123.5	124.0	123.8	123.2	122.4
	10%	11%	13%	14%	16%	17%

For horizontal and vertical air gaps, the influence of the relative permeability of the magnetic shielding material on the magnetic shielding effectiveness is shown in Figure 3.27 for both the magnetic circuit model and the FEM simulation. When the relative permeability of the magnetic shielding is varied from 1000 to 100000, the proposed magnetic circuit model has similar trends as the FEM simulations and the maximum relative error is no more than 21 percent for the horizontal air gaps and 11 percent for the vertical air gaps.

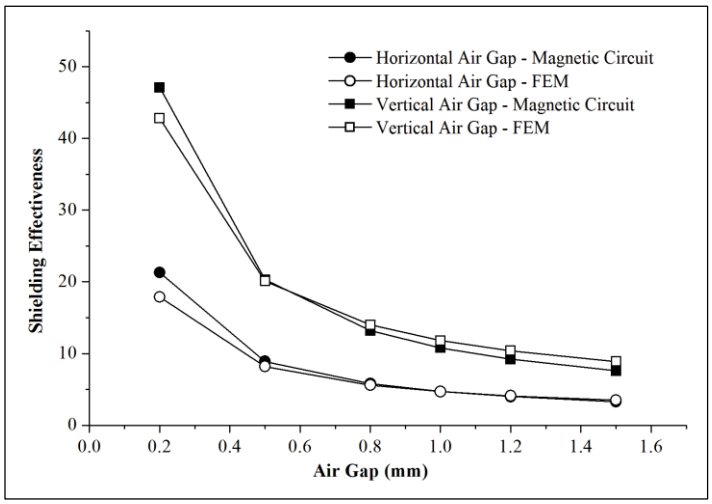

Figure 3.26. Comparison of air gap effect for horizontal and vertical air gaps in hollow cylindrical structure
(a =10 mm, b =10 mm, r = 90 mm).

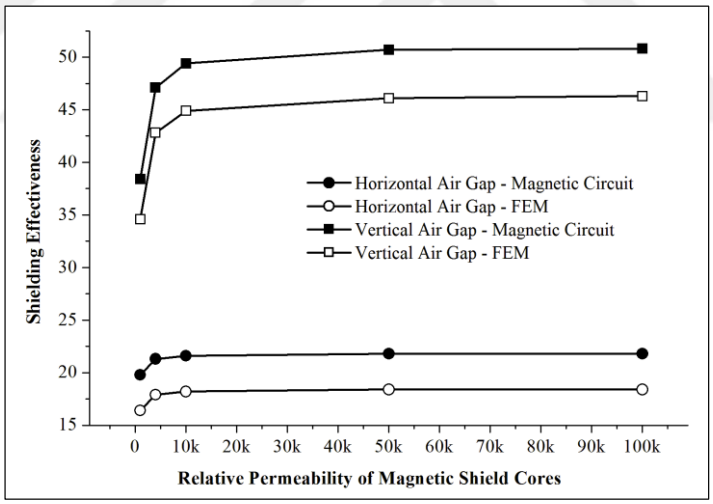

Figure 3.27. Comparison of relative permeability effect for horizontal and vertical air gaps in hollow cylindrical structure
(a =10 mm, b =10 mm, r = 90 mm)

The radius r of the cylindrical structure of the shielding does not influence the shielding effectiveness if it is higher than 60 mm. Therefore, the relative error of the magnetic circuit model does not change when r is increased and it does not exceed 20 percent for horizontal air gaps and 11 percent for vertical air gaps, when the gap is kept at 0.2 mm.

3.3.2. Results for Hollow Toroidal Structure

Magnetic shielding effectiveness for changing the thickness and the shielding distance is shown in Table 3.5 for the hollow toroidal magnetic shielding structure. The maximum and the minimum errors, when the thickness and the shielding distance are varied between 5 mm and 30 mm, are 18 percent and 3 percent, respectively. The magnetic circuit approach gives slightly higher magnetic shielding effectiveness values when it is compared to the FEM results for the range considered.

Table 3.5. Influences of (a) and (b) on magnetic shielding effectiveness for hollow toroidal magnetic shielding r = 90 mm, g = 0.2 mm

***a\b* (mm)**	**5**	**10**	**15**	**20**	**25**	**30**
5	**14.8**	**16.7**	**17.8**	**18.5**	**18.9**	**19.1**
	16.4	18.1	19.0	19.4	19.6	19.7
	11%	9%	7%	5%	4%	3%
10	**20.7**	**24.9**	**27.5**	**29.2**	**30.4**	**31.2**
	24.0	28.3	30.9	32.5	33.5	34.1
	16%	14%	12%	11%	10%	9%
15	**24.3**	**30.3**	**34.3**	**37.2**	**39.3**	**40.8**
	28.5	34.9	39.1	42.0	44.0	45.3
	17%	15%	14%	13%	12%	11%
20	**26.6**	**34.1**	**39.4**	**43.3**	**46.2**	**48.4**
	31.3	39.5	45.2	49.2	52.2	54.3
	18%	16%	15%	14%	13%	12%
25	**28.3**	**36.9**	**43.3**	**48.1**	**51.7**	**54.5**
	33.3	42.8	49.7	54.9	58.7	61.6
	18%	16%	15%	14%	14%	13%
30	**29.5**	**39.0**	**46.2**	**51.8**	**56.1**	**59.4**
	34.7	45.3	53.3	59.3	64.0	67.5
	18%	16%	15%	15%	14%	14%

The differences of magnetic shielding effectiveness values between the magnetic circuit approach and the FEM simulation are shown in Figure 3.28 when air gaps are varied from 0.2 mm to 1.5 mm (a =10 mm, b =10 mm, r = 90 mm). The maximum relative error of 12 percent occurs at 0.2 mm gap distance. Increasing the gap distance reduces the relative error between the magnetic circuit approach and the FEM result. The changes in magnetic

shielding effectiveness as a function of relative permeability of the magnetic shielding are shown in Figure 3.29. The maximum error is also about 18 percent for 100000 relative permeability.

The major radius r of the toroidal magnetic shielding structure has a negligible effect on the magnetic shielding effectiveness values as is the case with the cylindrical magnetic shielding.

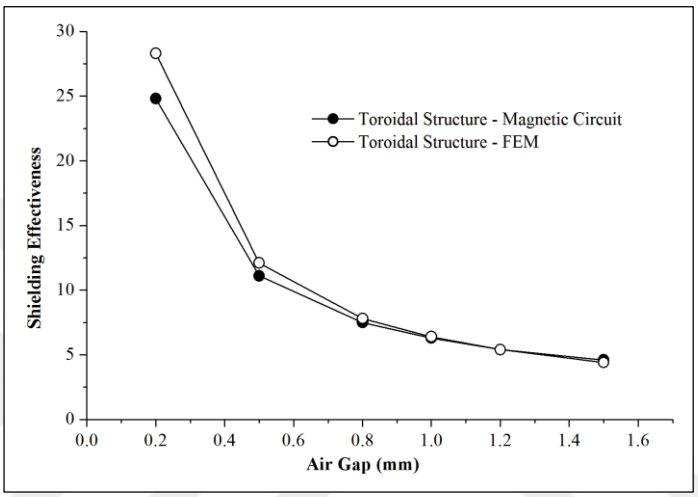

Figure 3.28. Comparison of air gap effect for hollow toroidal structure (a =10 mm, b =10 mm, r = 90 mm).

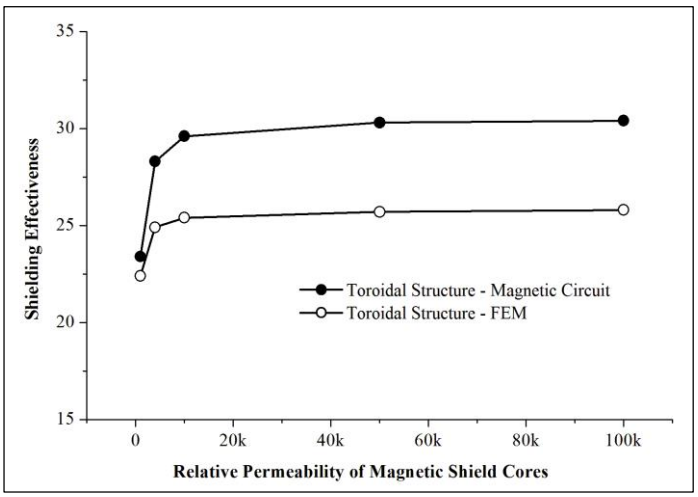

Figure 3.29. Comparison of relative permeability effect for hollow toroidal structure (a =10 mm, b =10 mm, r = 90 mm)

4. MAGNETICALLY SHIELDED ROGOWSKI COIL

4.1. DESIGN CONSIDERATION

Rogowski coils are made of rigid or flexible non-magnetic materials in a round or oval shape. The coils can be made as non-split cores or openable split-core constructions. The cross-sectional shape of the coil is generally either circular, oval or rectangular. The RCs may be wound uniformly distributed having a single layer or multiple layers.

To avoid the formation of a loop or “air turn” on the RC, the coil is generally wound in two layers and one layer is wound opposite to the winding direction of the other layer. If the coil is wound in a single layer, the other end of the winding is brought back directly around the coil former. An electrostatic shield made by a thin copper is used to reduce the impact of external electrical fields and noise in the design of RCs. A slit at one of the edges of the shield is left so that the electrostatic shield does not constitute a short-circuited turn around the coil.

The weakest point of RCs is the effects produced by external currents (or external varying magnetic fields) and the primary conductor position in the vicinity of the coil. The fields arising from currents flowing in neighboring phases and ground conductors are one of the main sources for systematic measurement errors of RCs.

In this dissertation, the aim is to improve the performance of RC by applying magnetic shielding techniques and to increase the immunity of an RC against the coupling of magnetic fields by more than a factor of 10 without compromising performance on the other aspects such as current linearity, temperature and frequency dependencies. To improve immunity against external magnetic fields, a hollow cylindrical magnetic shield is designed and implemented for RC. The magnetic shields are combined with windings inside and outside of the shields to prevent them from saturation. The use of nanocrystalline soft magnetic materials is considered. Finally, designed RC with improved immunity is characterized.

4.2. UNSHIELDED ROGOWSKI COIL

The model of SX-170 Rogowski coil made by ROCOIL was used for the application of magnetic shielding in this dissertation [55]. RC is made of an accurately-machined rigid plastic former with the rectangular cross-section. A uniformly distributed winding is achieved by using special winding machines. The RC shown in Figure 4.1 is manufactured in the split form to enable it to be installed without the disconnection of the primary conductors from their circuits. An electrostatic shield is made on the RC winding for reducing the impact of external electrical fields and noise. Extra turns are added to the end fitting of the coil to compensate air gaps. Each coil is repeatedly tested during fabrication and small adjustments are carried out to reduce the pickup of external magnetic fields.

The mutual inductance of RC is 3.604 μH. This RC has a very stable output and its accuracy is less than 0.1 percent. The dimensions of the RC are as follows; the inner diameter is 168 mm, the outer diameter is 216 mm and the height is 42 mm.

Figure 4.1. Unshielded RC

The output of RC is varied by the feeding conductor position due to the imperfections of the winding of RC. The manufacturer declares that if the conductor is moved from the central position by a distance equal to 0.5 x the inner coil radius the output will change by less than 0.1 percent. Additionally, the pickup of the magnetic field by the coil is less than 0.1 percent compared to the output of the coil if it was mounted around the conductor. Before applying the magnetic shield to this RC, measurements for the metrological performance of RC are carried out and results are presented in the next chapter.

4.3. CONSTRUCTION OF SHIELDED ROGOWSKI COIL

The principle of magnetic shielding was originally introduced by [15]. The shielding principle is similar to that used in current comparators. The magnetic shield consists of four tape-wound magnetic cores in the form of a hollow cylindrical structure which surrounds the rectangular non-magnetic former with horizontal air gaps; this is shown in Figure 4.2. Tape-wound magnetic cores are preferred in power system applications because of the simplicity of their construction. Magnetic cores are made from a high permeability nickel-iron ribbon with thickness of 0.1 mm. The ribbon is used to reduce total core loss. The technical drawings of all structures of the designed magnetic shield are given in Appendix B.

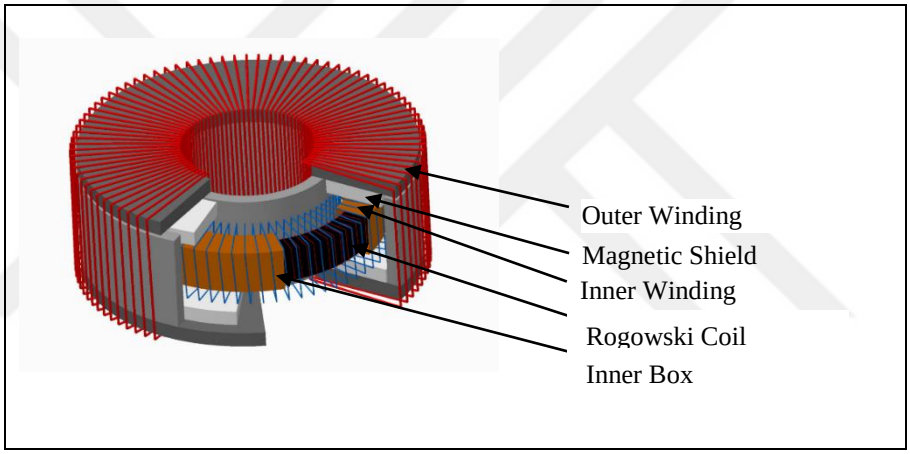

Figure 4.2. Cut-away view of magnetic shield

RC was placed in a rigid box to protect it against any deformation. The rigid box was produced by a 3D printer machine using polyamide materials and it is shown in Figure 4.3.

Figure 4.3. Inner protection box

A closed-loop consisting of two additional windings was installed in order to avoid the saturation of the magnetic shield. These windings, having the same number of turns, were placed one inside and one outside the magnetic shield. In respect to avoiding the detection by the secondary coil, the windings were connected in series with oppose direction so that their ampere-turns are canceled. Inner winding which has 400 turns with 0.9 mm enameled copper wire was wound by using a special winding machine on the rigid box. Inner winding was uniformly distributed around the rigid box in a single layer and is shown in Figure 4.4.

Figure 4.4. Inner winding

Next, the RC with the inner winding was placed into the hollow cylindrical magnetic shield. The magnetic shield must be effective for vertical and horizontal external magnetic fields. For horizontal external field, formulation (2.2) in the literature is considered to be of sufficient accuracy and magnetic shielding effectiveness values are higher than that of vertical external field because of low reluctances of horizontal magnetic shells with no air gaps. Therefore, it is not critical and not examined in this study. Whereas, the magnetic shielding effectiveness for external vertical magnetic fields has been investigated with great detail in Chapter 3. As has been seen there, the magnetic shielding effectiveness depends on the thickness of the hollow cylindrical magnetic shielding structure, the distance between non-magnetic former and magnetic shields, and the air gap distance between magnetic shielding and permeability of magnetic shielding materials. The higher shielding effectiveness can be achieved by increasing the shielding thickness and the distance between non-magnetic former and magnetic shields. However, it is inevitable that these increases will also adversely affect the weight and the cost of the magnetically shielded RC. Thus, the magnetic shielding thickness and the distance were set to 10 mm to have an acceptable weight and cost without compromising magnetic shielding effectiveness value much.

Because of cylindrical structure of shielding ribbons, the air gap is inevitable in the manufacturing of magnetic shield which reduces the shielding effectiveness. Therefore, the air gap was kept as minimum as possible for the higher shielding effectiveness. The dimensions of the magnetic cores are given in Table 4.1.

Table 4.1. Dimensions of magnetic cores

Magnetic Cores	**Dimensions (mm)** **(Inner diameter x Outer diameter x Height / Tape thickness)**
Inner Core	128 x 148 x 62 / 0.1
Outer Core	236 x 256 x 62 / 0.1
Top and Bottom cores	128 x 256 x 10 /0.1

The magnetic shielding effectiveness of constructed RC is calculated based on proposed magnetic circuit model and FEM simulation in the following section. The equivalent reluctances between the nodes in Figure 4.5 can be calculated as

$$\mathcal{R}_{K1} = 2\ \mathcal{R}_1 + 2\ \mathcal{R}_{Hg} + \mathcal{R}_{Ha} = 2\ (\mathcal{R}_1 + \mathcal{R}_{Hg}) + \mathcal{R}_{Ha} \tag{4.1}$$

$$\mathcal{R}_{K2} = 2\ \mathcal{R}_2 + \mathcal{R}_C \tag{4.2}$$

$$\mathcal{R}'_{K1} = 2\ \mathcal{R}'_1 + 2\ \mathcal{R}'_{Hg} + \mathcal{R}'_{Ha} = 2\ (\mathcal{R}'_1 + \mathcal{R}'_{Hg}) + \mathcal{R}'_{Ha} \tag{4.3}$$

For the nodal analysis, permeances are used. Therefore, corresponding permeances are given by $\mathcal{L}_{R_{H3}} = 1/\mathcal{R}_{H3}$, $\mathcal{L}_{\mathrm{R'_{H3}}} = 1/\mathcal{R}'_{\mathrm{H3}}$, $\mathcal{L}_{\mathrm{K1}} = 1/\mathcal{R}_{K1}$, $\mathcal{L}_{\mathrm{K2}} = 1/\mathcal{R}_{K2}$, and $\mathcal{L}_{\mathrm{K3}} = 1/\mathcal{R}_{K3}$. The calculated reluctances of the magnetically shielded RC are given in Table 4.2.

Table 4.2. Calculated reluctance values of magnetically shielded RC
(ampere-turns / weber)

$\mathcal{R}_0$	$\mathcal{R}'_0$	$\mathcal{R}_1$	$\mathcal{R}'_1$	$\mathcal{R}_2$	$\mathcal{R}_{H3}$	$\mathcal{R}'_{H3}$	$\mathcal{R}_{Hg}$
238.179	126.164	229.441	128.711	37.4797	1045.640	784.72	36710.57
$\mathcal{R}'_{Hg}$	$\mathcal{R}_{Ha}$	$\mathcal{R}'_{Ha}$	$\mathcal{R}_c$	$\mathcal{R}_{K1}$	$\mathcal{R}_{K2}$	$\mathcal{R}'_{K1}$	
20593.74	2826.71	1585.72	1858994.25	76706.74	1859069.21	43030.61	

Node equations can be written by considering Chapter 3.1.1. Therefore, it is very simple to construct the matrix equation by just considering the magnetic circuit in Figure 4.5.

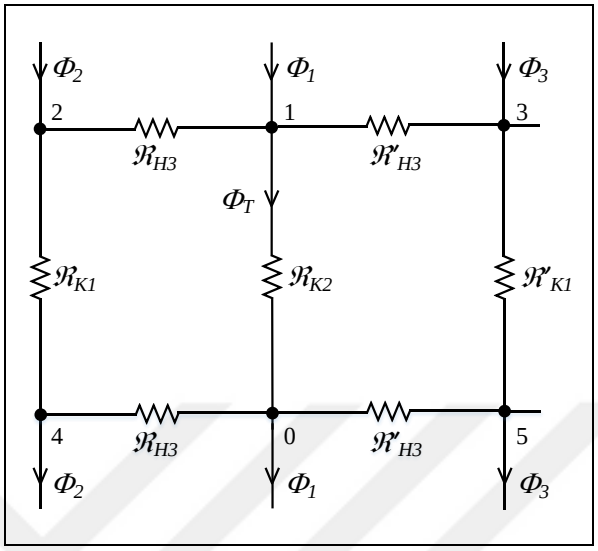

Figure 4.5. A simplified equivalent magnetic circuit

By using this nodal analysis and by taking the zero node as the reference, node equations are constructed in matrix form. The left side corresponds to the source flux vector Φ and the right side of the permeance matrix $\mathcal{L}$ corresponds to the magnetomotive force vector $\mathcal{F}$ in (4.4).

$$\begin{bmatrix} \emptyset_1 \\ \emptyset_2 \\ \emptyset_3 \\ -\emptyset_2 \\ -\emptyset_3 \end{bmatrix} = \begin{bmatrix} \mathcal{L}_{R_{H3}} + \mathcal{L}_{R'_{H3}} + \mathcal{L}_{R_{K2}} & -\mathcal{L}_{R_{H3}} & -\mathcal{L}_{R'_{H3}} & 0 & 0 \\ -\mathcal{L}_{R_{H3}} & \mathcal{L}_{R_{H3}} + \mathcal{L}_{R_{K1}} & 0 & -\mathcal{L}_{R_{K1}} & 0 \\ -\mathcal{L}_{R'_{H3}} & 0 & \mathcal{L}_{R'_{H3}} + \mathcal{L}_{R_{K3}} & 0 & -\mathcal{L}_{R_{K3}} \\ 0 & -\mathcal{L}_{R_{K1}} & 0 & \mathcal{L}_{R_{H3}} + \mathcal{L}_{R_{K1}} & 0 \\ 0 & 0 & -\mathcal{L}_{R_{K3}} & 0 & \mathcal{L}_{R'_{H3}} + \mathcal{L}_{R_{K3}} \end{bmatrix} \begin{bmatrix} \mathcal{F}_1 \\ \mathcal{F}_2 \\ \mathcal{F}_3 \\ \mathcal{F}_4 \\ \mathcal{F}_5 \end{bmatrix} \quad (4.4)$$

The magnetic shielding effectiveness of designed magnetic shield with a horizontal air gap was calculated as 35.3 based on the magnetic circuit model and as 27.9 based on FEM simulation. The relative error between the magnetic circuit model and the FEM simulations is found to be 27 percent for the external vertical magnetic field (1000 A/m).

To prevent the formation of a short circuit during the assembly of the magnetic shield, durable insulation was incorporated. The magnetic shield is illustrated in Figure 4.6. For

minimization of the air gap, a notch was left on the outer shielding to provide connection with the outer circuit.

Figure 4.6. Applying hollow toroidal magnetic shield

A pressboard material on cellulose basis was used to protect the outer winding from the sharp edge of the magnetic shield and is shown in Figure 4.7. The outer winding was wound in a single layer and uniformly distributed around the magnetic shield after the final insulation. The outer winding has 400 turns as inner winding does and it is shown in Figure 4.8. Finally, protective isolation was made on the magnetically shielded RC.

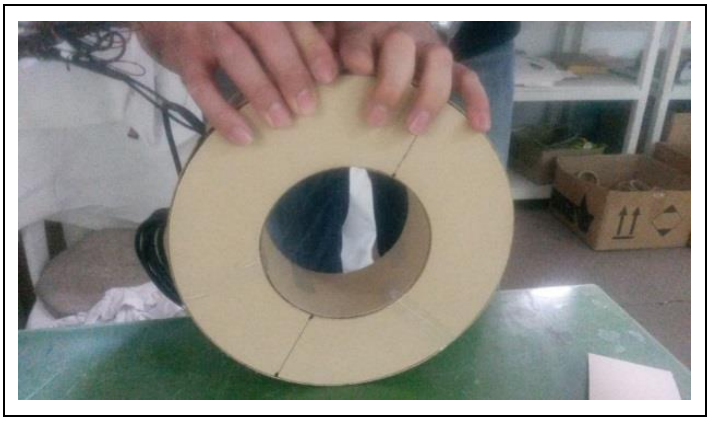

Figure 4.7. Protection box

Figure 4.8. Outer winding

5. DEVELOPMENT OF CALIBRATION SYSTEM FOR NON-CONVENTIONAL CURRENT SENSORS

High current measuring devices can be classified into two categories as conventional and non-conventional. RC sensors are the most common types of non-conventional current sensors and they are well suited for high voltage application in power grids.

In this chapter, the aim is to determine the requirements for the calibration of RC and to investigate the calibration methods. The nominal secondary voltages of analog current sensor and the nominal burden values of its secondary will be defined according to international standards as DIN EN 60044-8 “Specific Requirements for Electronic Current Transformers” [30] published by German Institute for Standardization and IEC 61869-1 “General Requirements” [56] published by International Electrotechnical Commission.

Furthermore, the existing measurement systems of instrument transformer manufacturers and the sampling-based power measurement system of National Metrology Institutes (NMIs) will be modified to satisfy the calibration need for non-conventional current sensors.

5.1. GENERAL REQUIREMENTS

The calibration requirements for non-conventional current sensors are identified in this section [40]. The secondary currents of existing calibration systems for conventional current transformers are set to either 1 A or 5 A. However, non-conventional current sensors can output either lower current or voltage. This means that possible conversions for such sensors will be current-current and current–voltage. The nominal output levels are defined in the international standards. According to DIN EN 60044-8, the nominal secondary voltages of current sensors are as follows: 2.5 mV, 150 mV, 200 mV, 225 mV, and 4 V; the burden values are as follows: 2 kΩ, 20 kΩ, and 2 MΩ.

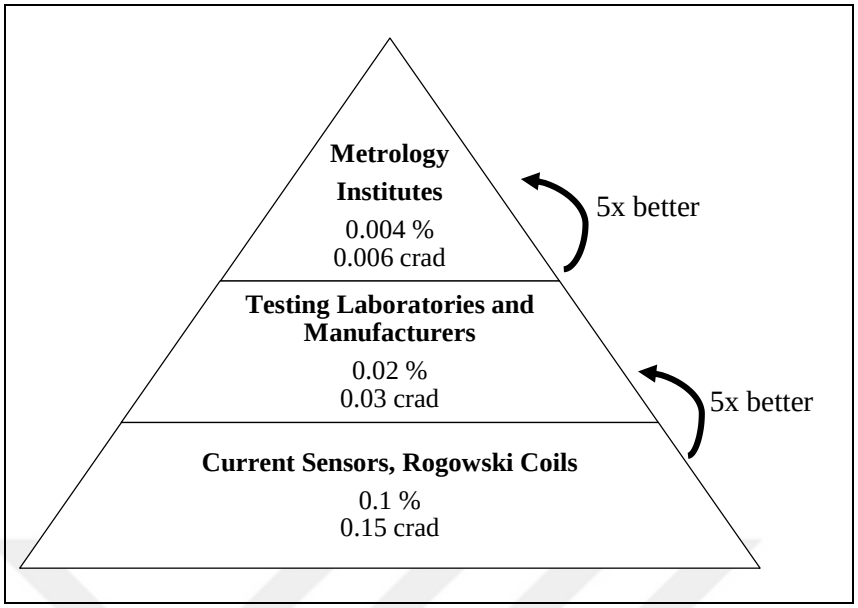

Figure 5.1. Traceability chain of the instrument transformers to national standards

For calibration of current sensors, the test uncertainty ratio is generally selected as five. This means that the measurement uncertainty of the accredited testing laboratories should be five times better than the accuracy of current sensors which are given in Table 5.1. At the same time, NMIs should ensure calibration services to the testing laboratories with five times better accuracy than their test equipment. The traceability chain for instrument transformer calibration is shown in Figure 5.1.

Table 5.1. Accuracy classes according to DIN EN 60044-8 current sensors

Accuracy class	**Error limits at percentage of rated current**														
	Current error ± ε_I					**Phase displacement ± δ**									
	%					**minutes**					**crad**				
	1	**5**	**20**	**100**	**120**	**1**	**5**	**20**	**100**	**120**	**1**	**5**	**20**	**100**	**120**
0.1	-	0.4	0.2	0.1	0.1	-	15	8	5	5	-	0.45	0.24	0.15	0.15
0.2	-	0.75	0.35	0.2	0.2	-	30	15	10	10	-	0.9	0.45	0.3	0.3
0.2 S	0.75	0.35	0.2	0.2	0.2	30	15	10	10	10	0.9	0.45	0.3	0.3	0.3
0.5	-	1.5	0.75	0.5	0.5	-	90	45	30	30	-	2.7	1.35	0.9	0.9
0.5 S	1.5	0.75	0.5	0.5	0.5	90	45	30	30	30	2.7	1.35	0.9	0.9	0.9
1.0	-	3.0	1.5	1.0	1.0	-	180	90	60	60	-	5.4	2.7	1.8	1.8

5.2. CALIBRATION SYSTEMS

The calibration methods for non-conventional current sensors are studied by considering the general requirements for calibration of current sensors and the existing measurement infrastructures of test laboratories, instrument transformer manufacturers and NMIs.

5.2.1. Modified Calibration System with Laboratory Standards

The calibration setup given in Reference [30] for non-conventional current sensors is not a useful method for testing laboratories since it needs too many modifications in the laboratory, and an additional cabling.

The modified calibration system for the current sensor shown in Figure 5.2 consists of a standard current transformer, a current transformer measuring bridge, and a transconductance amplifier. The same primary current signal is applied to the primaries of the standard current transformer, and of the current sensor under calibration. The output of the current sensor whose output voltage is converted to the current is compared with the secondary current of the standard current transformer by using the measuring bridge.

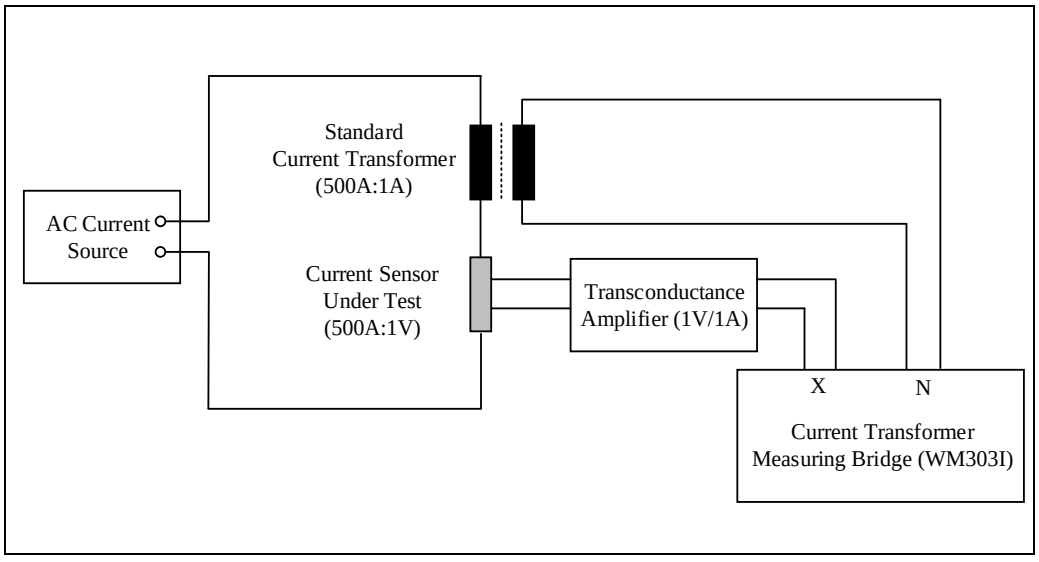

Figure 5.2. Modified calibration setup for current sensors

The analog output of current sensors is converted to traditional current output levels of conventional transformers by integrating a transconductance amplifier into an existing

calibration system for conventional transformers so that two outputs of the current sensor and conventional current transformer are to be comparable at power frequencies.

The single range transconductance amplifier was designed with the nominal input voltage of 1 V and the output current of 1 A by considering the minimizing of loading effects caused by cabling on the amplifier [57]. The amplifier linearly operates between 5 percent and 200 percent of the nominal voltage/current amplification range (50 mA – 2 A). The input impedance of the amplifier is greater than 10 MΩ. Accuracies of the amplifier are determined as 100 parts per million (ppm) for ratio error and 100 μrad for phase displacement. The amplifier whose circuit diagram shown in Figure 5.3 consists of three stages: a unity gain buffer, a control amplifier, and a power amplifier.

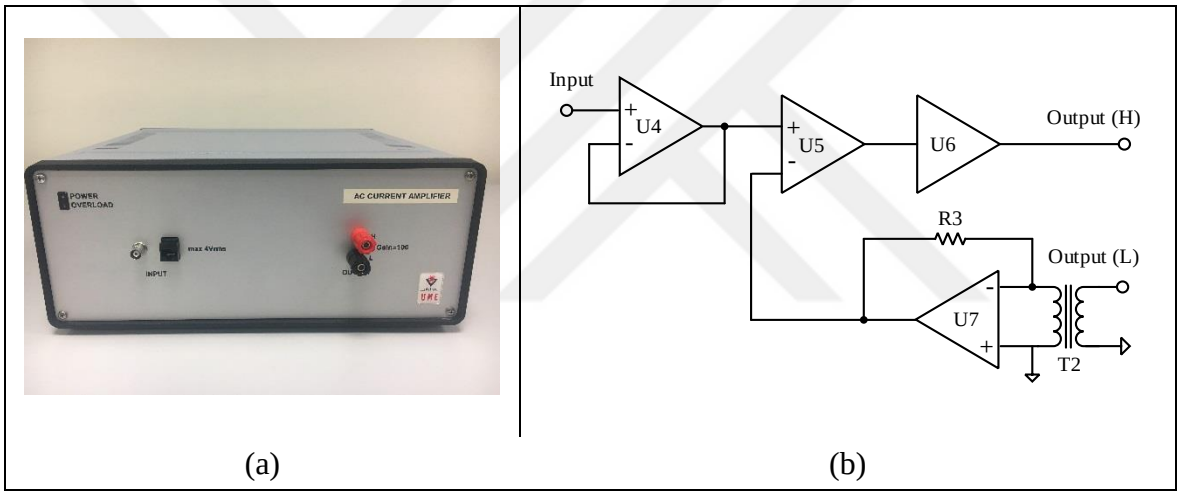

Figure 5.3. (a) Transconductance amplifier and (b) its circuit diagram

Filtering, guarding, electrostatic shielding, magnetic shielding, and electronically compensation techniques in the design of the transconductance amplifiers have been taken into consideration to achieve the targeted accuracy and linearity. Each stage of electronic cards has been enclosed in a magnetically shielded box to minimize ambient magnetic field effects. Since a frequency variation of primary current causes short-time instabilities in the amplifier, the electronic source with stable frequency output is used to generate the primary currents.

5.2.2. Sampling-Based Calibration System

The main idea of the sampling-based calibration system shown in Figure 5.4 is to measure the output voltage of the current sensor with a voltage drop across the current shunt simultaneously by using precise high-resolution samplers. The current shunt is connected to the secondary of the standard current transformer to convert the output current of the standard current transformer to the voltage signal. Sampling-based voltage ratio measurement system consists of two digitizers which are externally triggered by the signal generator to sample the voltage signals simultaneously. The sampling frequency is set to the measured frequency. The measured signals are transformed into the frequency domain by Fast Fourier Transform, subsequently, only fundamental component is picked out for determining of the ratio error and phase displacement of the current sensor by the software. Each of the components of the calibration system needs to be individually characterized in order to achieve the highest precision and to establish the traceability chain.

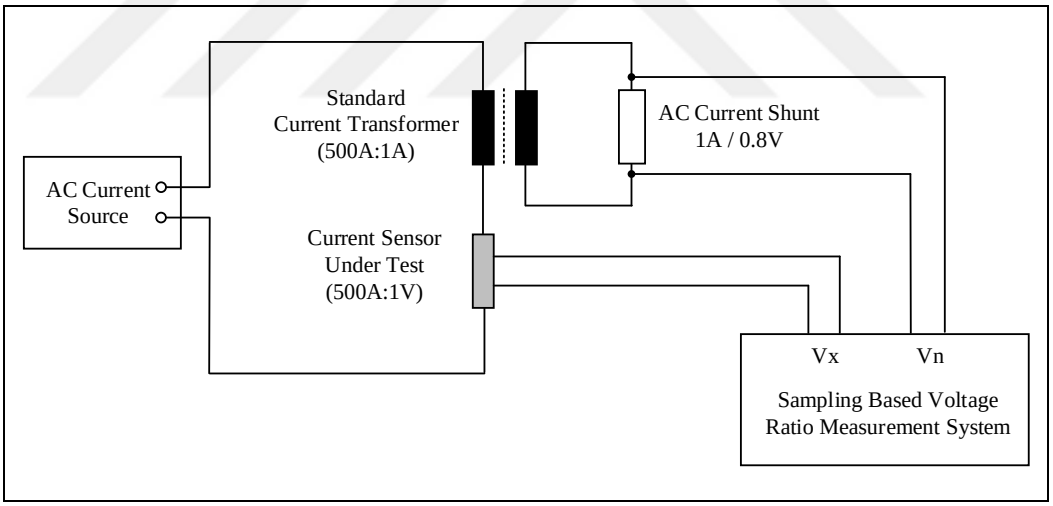

Figure 5.4. Sampling-based calibration setup for current sensors

5.2.3. Use of Commercial Non-Conventional Measuring Bridge

Non-conventional measuring bridge manufactured by ZERA company with the model of WM3000I is a special-edition commercial device for the calibration of the current sensor.

Since it has the direct voltage input for the current sensors (max. 15 V), there is no need for additional converting or scaling devices. This provides great convenience to the operators. The outputs of the current sensor and standard current transformer are directly connected to the measuring bridge. The calibration setup is shown in Figure 5.5.

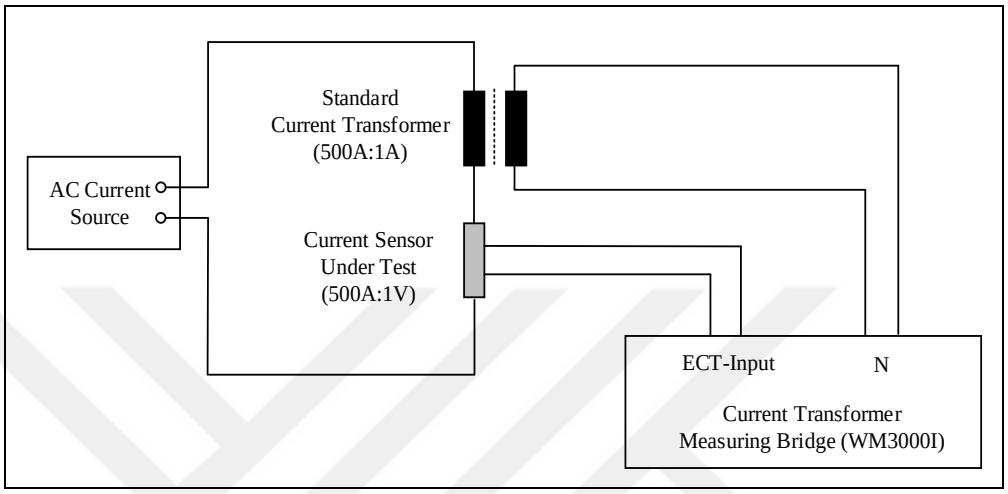

Figure 5.5. Use of non-conventional measuring bridge

ZERA bridges are controlled by software. The errors of the standard current transformer can be corrected by entering its errors to the software [58]. The specifications for calibration of analog non-conventional sensor are given in Table 5.2 for frequencies between 15 Hz and 65 Hz and for the currents of N-input between 50 mA and 15 A. The calibration system for the current sensor input (ECT mode) of ZERA WM3000I will be developed in the dissertation and explained in Chapter 5.3 in detail.

Table 5.2. Error limits for ZERA WM3000I

Voltage of ECT-channel	**Accuracy of ratio error**	**Accuracy of phase displacement**
200 mV < U ≤ 15 V	< 400 x 10^{-6}	< 0.6 min
20 mV < U ≤ 200 mV	< 600 x 10^{-6}	< 1.1 min

5.2.4. Evaluation of Developed Calibration Systems

The calibration systems are developed at TÜBİTAK UME Power and Energy Laboratory. The uncertainties for each calibration method are calculated.

The magnetically shielded RC produced in the dissertation is used as a device under calibration to evaluate the developed calibrations systems because of its good linearity. The first calibration method shown in Figure 5.6 to calibrate the coil is the modified calibration system with laboratory standards. The output voltage of RC is converted to the current via the transconductance amplifier and then two currents are compared via the measuring bridge.

Figure 5.6. View from modified calibration system with laboratory standards

The sampling-based calibration system shown in Figure 5.7 is established by converting the secondary current of the standard current transformer to the voltage with AC current shunt and then by comparing the output voltages of RC and AC current shunt via the sampling-based voltage ratio measurement system. The current shunt was manufactured by UME with the input current of 1 A, the output voltage of 0.8 V and the accuracy of 10 ppm / μrad. Finally, the last measurement was carried out by using WM3000I.

The measurements are performed in the current range of 50 - 500 A at 50 Hz. The results are given in Table 5.3. Measurement results with three calibration systems showed a good agreement for ratio errors and phase displacements.

The uncertainties for ratio error and phase displacements with three calibration setups are calculated and tabulated in Table 5.4 and Table 5.5, respectively. The lowest uncertainties for ratio error and phase displacement measurements are obtained as 0.005 percent and 0.005 crad with the sampling-based calibration system The results of each calibration system agree very well within the calculated measurement uncertainties.

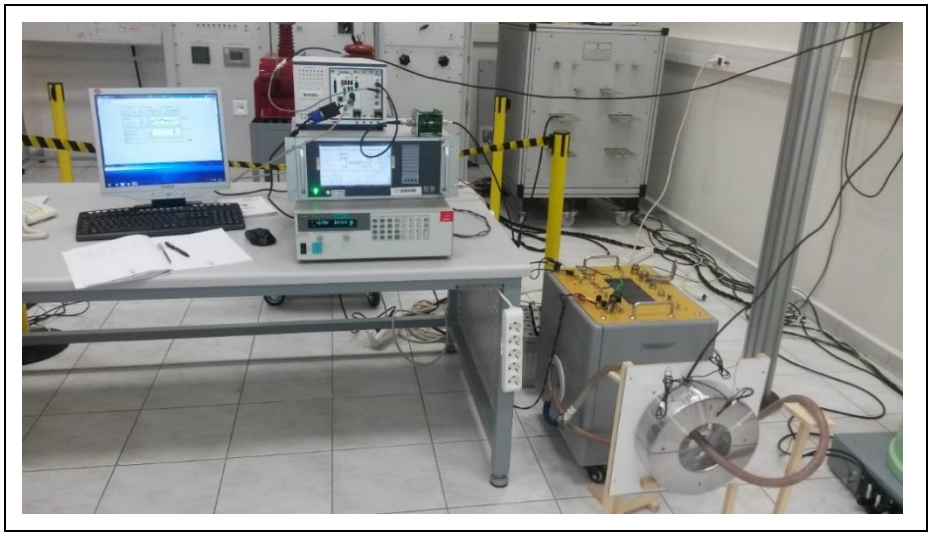

Figure 5.7 View from sampling-based calibration system

The uncertainties do not include the long term stability and the error of the current sensor to be calibrated. The reported expanded uncertainty of measurement is stated as the standard uncertainty of measurement multiplied by the coverage factor k = 2, which for a normal distribution, corresponds to a coverage probability of approximately 95 percent. The standard uncertainty of measurement has been determined in accordance with [59] - [60].

Table 5.3. Measurement results performed by three calibration systems

Applied Value (A)	**Ratio Error**			**Phase Error**		
	WM3000I (%)	**Modified (%)**	**Sampling-Based (%)**	**WM3000I (min.)**	**Modified (min.)**	**Sampling-Based (min.)**
500	0.015	0.013	0.013	-0.3	-0.2	-0.4
400	0.015	0.014	0.013	-0.3	-0.1	-0.4
300	0.015	0.014	0.013	-0.3	-0.1	-0.4
250	0.018	0.012	0.013	-0.3	-0.1	-0.4
200	0.018	0.013	0.013	-0.3	-0.1	-0.4
150	0.015	0.012	0.013	-0.3	-0.1	-0.4
100	0.015	0.012	0.013	-0.3	-0.1	-0.4
50	0.015	0.012	0.013	-0.3	-0.2	-0.4

All calibration methods have been verified, and the characterization of transducers (e.g transconductance amplifier, current shunt) has been performed by utilization of the calibrated reference current to voltage converter and inductive voltage dividers [61].

The calibration method by modifying the existing calibration system for the conventional current transformer method might be highly useful and reliable for calibration and testing laboratories and manufacturers of conventional and non-conventional instrument transformer. Sampling-based calibration system is preferred by NMIs because of achieving the highest accuracy. Its main challenge is that the outputs of current sensors and standard current transformer are precisely brought to the suitable levels for the digitizers (samplers). Since commercial non-conventional measuring bridge has the direct voltage input for the current sensors (max. 15 V), there is no need for additional converting or scaling devices. This provides great convenience to the operators. The effects of linearity and ambient temperature are not studied in the dissertation work.

Table 5.4. Uncertainties budget for ratio measurements

Uncertainty Sources	**Partial Uncertainty**			**Variance**		
Description	**%**	**Probability Dist.**	**Factor**	**Sampling-Based**	**Modified**	**WM3000I**
Standard Current Transformer	0.001	Normal	0.5	2.5E-07	2.5E-07	2.5E-07
Sampling System	0.002	Normal	0.5	1.0E-06		
WM3000I (Conventional Part)	0.001	Normal	0.5		2.5E-07	
WM3000I (ECT Part)	0.008	Normal	0.5			1.6E-05
Voltage to Current Amplifier	0.002	Normal	0.5		1.0E-06	
Current Shunt	0.002	Normal	0.5	1.0E-06		
Linearity		Rect.	0.577			
Effect of conductor position	0.001	Rect.	0.577	3.3E-07	3.3E-07	3.3E-07
Effect of external magnetic field	0.001	Rect.	0.577	3.3E-07	3.3E-07	3.3E-07
Ambient Temperature		Rect.	0.577			
Stability and repeatability	0.002	Normal	1	4.0E-06	4.0E-06	4.0E-06
	Total Variance			6.9E-06	6.2E-06	2.1E-05
	Standard Uncertainty (%)			0.003	0.002	0.005
	Expanded Uncertainty (%)			0.005	0.005	0.009

Table 5.5. Uncertainties budget for phase displacement

Uncertainty Sources	Partial Uncertainty			Variance		
Description	**crad**	**Probability Dist.**	**Factor**	**Sampling-Based**	**Modified**	**WM3000I**
Standard Current Transformer	0.001	Normal	0.5	2.5E-07	2.5E-07	2.5E-07
Sampling System	0.002	Normal	0.5	1.0E-06		
WM3000I (Conventional Part)	0.006	Normal	0.5		9.0E-06	
WM3000I (ECT Part)	0.008	Normal	0.5			1.6E-05
Voltage to Current Amplifier	0.004	Normal	0.5		4.0E-06	
Current Shunt	0.002	Rect.	0.5	1.0E-06		
Linearity		Rect.	0.577			
Effect of conductor position	0.001	Rect.	0.577	3.3E-07	3.3E-07	3.3E-07
Effect of external magnetic field	0.001	Rect.	0.577	3.3E-07	3.3E-07	3.3E-07
Ambient Temperature		Rect.	0.577			
Stability and repeatability	0.002	Normal	1	4.0E-06	4.0E-06	4.0E-06
	Total Variance			6.9E-06	1.8E-05	2.1E-05
	Standard Uncertainty (crad)			0.003	0.004	0.005
	Expanded Uncertainty (crad)			0.005	0.008	0.009
	Expanded Uncertainty (min)			0.2	0.3	0.3

5.3. CALIBRATION SYSTEM FOR COMMERCIAL MEASURING BRIDGE

5.3.1. Introduction

Traditional measuring bridge which carries out a differential comparison between the secondaries of standard transformer and transformer/sensor to be calibrated should be generalized for analog and digital current sensors. Therefore, the capability of the measuring bridge is widened for the measurement of non-standard secondary analog current or voltage levels as well as calibration of non-conventional current sensors with digital output. Hence, the analog front-end of traditional measuring bridge is replaced with circuitry comparing an

analog conventional input to either analog or digital non-conventional input in the design of the measuring bridge [62]. The generalized calibration setup for analog and digital current sensors is illustrated in Figure 5.8.

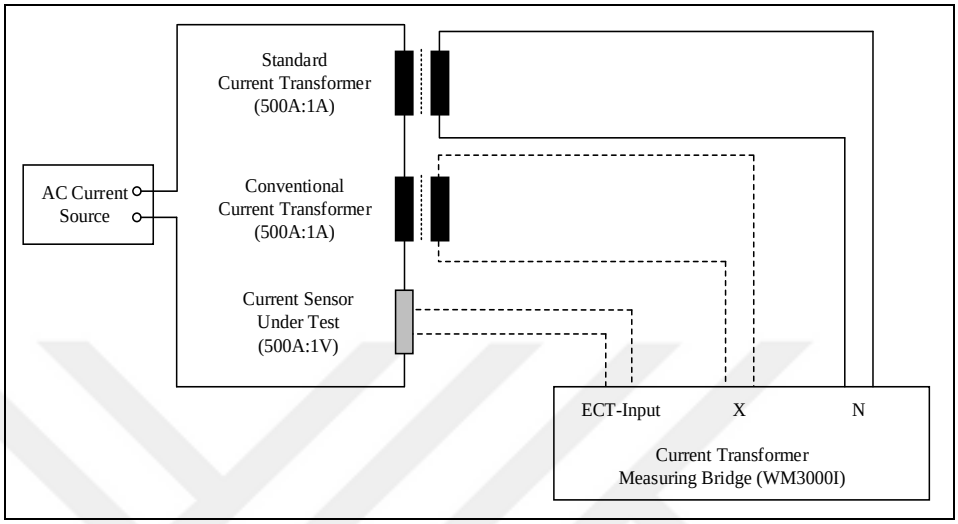

Figure 5.8. Commercial test set for non-conventional current sensor.

The calibration infrastructure for the new generation measuring bridge which is used as a reference in calibration of conventional and non-conventional current transformers is needed for ensuring the traceability of the measurement results.

5.3.2. Development of Calibration Method

A calibration method which is practical, highly accurate and applicable to a wide current and voltage ranges is developed by using the three phase power source, the electronically-compensated current comparator (ECCC) and the current shunt as references for commercial non-conventional measuring bridges (ZERA WM3000I) with analog outputs. The verification and calibration of ECCC and AC current shunt are presented. Finally, uncertainty of calibration is evaluated by considering whole uncertainty sources.

5.3.2.1. Electronic Current Transformer (ECT) Mode Calibration

The main principle of ECT mode calibration is that two isolated current signals with known ratio and phase differences are generated by using a three-phase PC controlled current

source, wattmeter and ECC, and then these isolated signals are applied to WM3000I [63]. To simulate the output of the current sensor, one of two isolated current signals is transformed to a voltage by using an accurate AC current shunt. The calibration setup and view of the ECT mode of WM3000I are shown in Figure 5.9 and Figure 5.10 respectively.

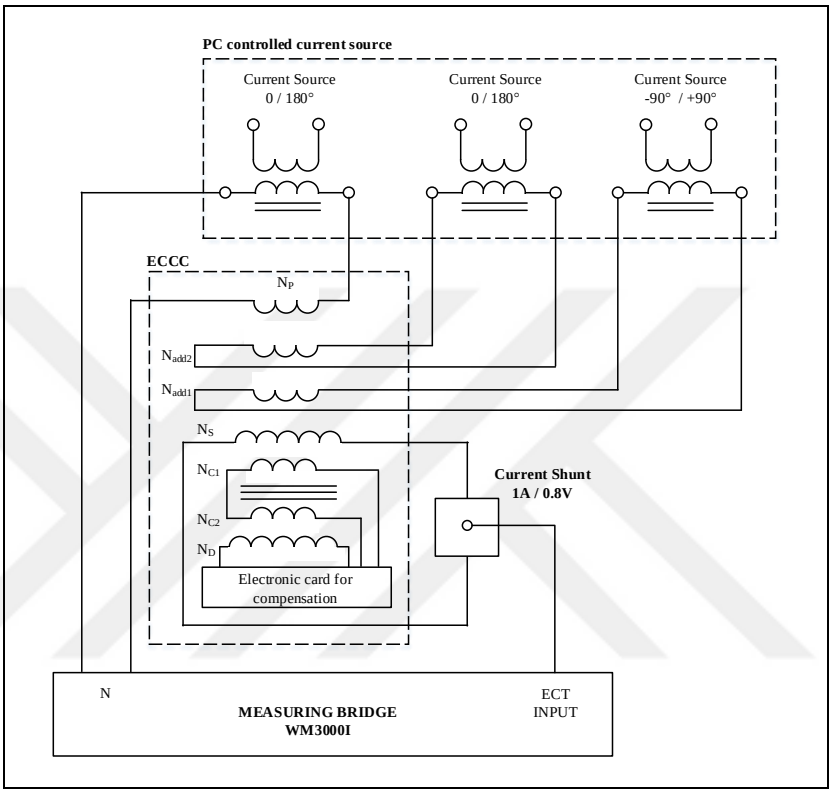

Figure 5.9. Calibration setup for the ECT part of WM3000I

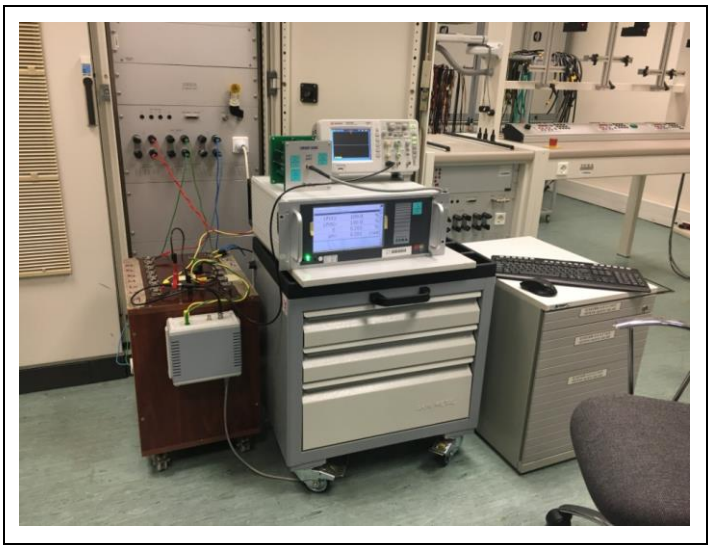

Figure 5.10. View from calibration

5.3.2.2. Electronically-Compensated Current Comparator

The current comparator with its first use dating back to 1960s is a stable, accurate and reliable magnetic device for AC current ratio measurements. Magnetic shielding has long been used to prevent the detector of the current comparator from the leakage and the external magnetic fluxes in the current comparator. In this way the unbalanced currents are sensed by the detector core almost with a few parts in 100 000. Moreover, by using an electronic circuit for compensation in its design, the errors of the current comparator can be lowered more than a few parts in million (ppm).

The ECCC developed by UME was modified for the ECT mode calibration of WM3000I by adding two additional windings inside and outside of its magnetic shield so that two isolated current signals with known ratio and phase differences are not compensated by the unit. The current comparator shown in Figure 5.11 comprises a detector core C_3, a detection winding N_D, a magnetic shield in the form of a hollow cylindrical structure C_1 enclosing the detector core, a primary winding N_P and a secondary winding N_S. In addition, it has also two compensation windings N_{C1}, N_{C2}. These windings, having the same number of turns, are wound inside and outside of hollow cylindrical magnetic shield and connected in series opposite direction so that the compensation current is not be sensed by the detector winding.

The dashed line E_1 here shows a thin electrostatic shield made by copper foil enclosing the detector winding. The electrostatic shield prevents the detector winding from the stray electric fields produced by primary and secondary currents. C_2 depicts a thick magnetic shield made by ferromagnetic foil enclosing all. The dashed line E_2 represents a thick copper shield.

The voltage induced on the detector winding by unbalanced ratio currents converts a current by using electronic circuitry as a transconductance amplifier, represented by A. It applies the compensation current to the inner and outer compensation windings not only for compensation of the secondary current but also for automatically zeroing the detection voltage.

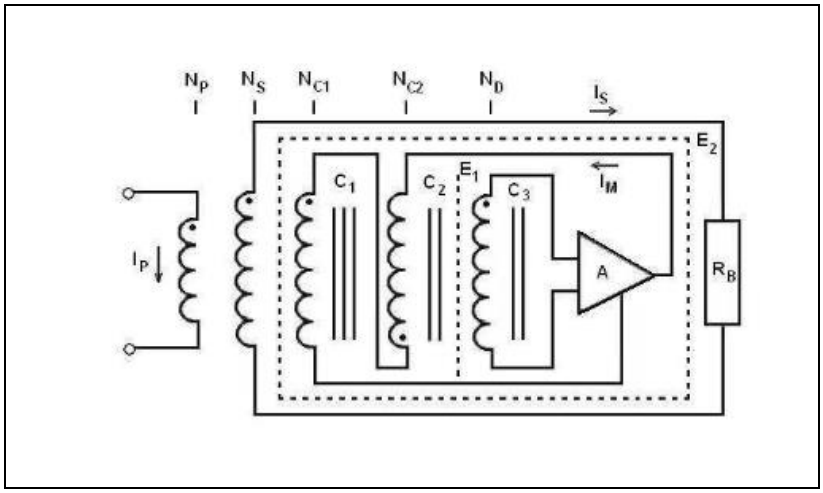

Figure 5.11. Electronically compensated current comparator [63]

5.3.2.3. AC Current Shunt

AC current shunt is used in order to transform the secondary of the standard current transformer into the voltage which simulates the output voltage of current sensors. The coaxial current shunt was first developed by Mendelejev Institute, St Petersburg with a squirrel-cage design [64], [65]. As can be seen from Figure 5.12, the shunt has an extremely symmetrical design to reduce the mutual inductance between the output of shunt and the current path leading to the resistors and also external current loops. The current paths and sidewalls of the coaxial shunt are constructed by double-sided copper-clad printed circuits boards. The currents from flowing from the top and bottom of the board are equal and opposite to each other. Since the thickness of the boards is very low, the current loop area here is also very low. The magnetic fields produced by these loops and by external current loops are suppressed using the cylindrical symmetric and metal chassis. The problem of centralized resistances such as skin effect is reduced by using discrete resistors. These resistors are located away from the current input connector of the shunt in order to prevent the possible asymmetries.

AC current shunt was designed by UME with the rated current value of 1 A and the output voltage of 0.8 V. It was calibrated by UME standards with an uncertainty level about 2 μΩ/Ω and 5 μrad.

Figure 5.12. Current shunt

5.3.2.4. Generation of Calibration Values

Any error required for the ECT mode calibration of WM3000I can be obtained with the combination of a three-phase current source, the ECCC, and two additional windings. A current signal is generated by the first phase of three-phase current source and this signal is then applied to the N input of WM3000I and to the primary winding of the ECCC in serial. To simulate the output voltage of ECT under calibration, the secondary current of ECCC is transformed into a voltage by using AC current shunt and next, this voltage is applied to the ECT input of WM3000I.

Two additional windings are wound in order to generate known ratio errors and phase displacements. The required ratio errors are achieved by generating an in-phase current signal that is different from the main signal by 0º or 180º from the second phase of the three-phase current source and by applying this current signal to one of the additional windings of the ECCC. The required phase displacements are achieved by generating a quadrature-phase current signal which differs from the reference signal by +90º or -90º from the third phase of three-phase current source and applying this current signal to the second additional winding of ECCC. The primary and secondary windings of ECCC are equal since its transformation ratio is 1. Thus, complex total currents of the primary and two additional windings proportional to their number of turns are produced by the secondary side of the ECCC.

Grounding of the N current input and the ECT voltage input of WM3000I are occurred safely because of the magnetic coupling in the ECCC.

5.3.2.5. Verification and Uncertainty Evaluation

Linearity measurements of the current comparator at the unity ratio mode were performed by using the current transformer test-set with a resolution of 1 ppm at the maximum burden of 0.8 Ω which is the resistor value of AC current shunt used for generation of calibration values. The auxiliary compensated current comparator was needed for currents below 10 percent of nominal current due to instability problems. The auxiliary comparator has a compact design and a large number of turns in its detector in order to increase its sensitivity for lower currents and to have more stable results. The measurement results of the current comparator between 1 percent and 200 percent of nominal current 1 A are given in Table 5.6. The maximum ratio and phase error of the current comparator are found to be less than 2 μA/A and 2 μrad respectively with the current transformer test set and the auxiliary comparator as shown in Table 5.6. Phase errors of comparators are originated from capacitive currents flowing within and between the ratio windings, and between the ratio windings and ground.

Table 5.6. Calibration results of current comparator in Ratio 1:1

Applied Current, I_P (A)	**Measured Relative Error (Load 0.8 Ω)**		
	with current transformer test-set		**with auxiliary comparator**
	Ratio Error (μA/A)	**Phase Displacement (μrad)**	**Combined Error (μA/A)**
2	$\varepsilon \leq 2$	$\delta \leq 2$	0.8
1.2			0.9
1			1.1
0.5			1.4
0.2			1.7
0.1			1.5
0.05			1.8
0.01			1.9

Several additional tests have been carried out not only to analyze the linearity of the current comparator but also for verification of the generating system including the three-phase current source and the current comparator.

Since the number of turns of primary and secondary of the current comparator are equal and 200 turns, the in-phase current signal flowing the additional winding with one turn will induce a ±0.5 percent ratio difference on the secondary side. Inversing tests for the primary side were performed up to 10 turns, and no significant errors were observed from 1 percent to 200 percent of the nominal current.

In addition, such ratio errors and phase displacements configuring the number of turns of primary and secondary windings were compensated by applying the proper current signals from the second phase of three-phase current source to the additional winding. Since the accuracy of reference wattmeter used in three-phase current source is below 100 μA/A, ±0.5 percent ratio difference between primary and secondary currents by using 1 turn additional winding will be generated with the uncertainty of not greater than 1 μA/A.

The interaction of two additional windings with neglecting primary or secondary windings was studied by generating two current signals from the second and third phases of three-phase current source and by applying these currents to the additional windings. Successful compensation was observed. All tests were carried out for the generation of phase displacements.

The uncertainties of phase measurements are very low since the phase errors of units used in the generation of known phase displacements are not worse than 100 μrad. All uncertainty sources, their distributions and the uncertainty calculation of the developed calibration method are given in Table 5.7.

The ECT mode calibration of WM3000I with repeatability was performed by the developed calibration system with the total measurement uncertainty of not more than 10 μA/A and 10 μrad for ratio and phase error measurements, respectively. A sample calibration certificate using the developed measurement setup during this dissertation is given in Appendix A.

Table 5.7. Uncertainty calculation for ECT mode

Source of Uncertainty	Standard Uncertainty		Probability Distribution Contribution	Contribution to the Standard Uncertainty	
	Ratio Error (µA/A)	Phase Error (µrad)		Ratio Error (µA/A)	Phase Error (µrad)
Generating error values (wattmeter & divider)	2	5	Normal	2	5
Current Comparator (1:1 ratio & summing)	1	1	Normal	1	1
AC Current Shunt	18	< 1	Normal	2	5
Calibration setup	< 1	< 1	Rectangular	< 1	< 1
Repeatability	< 1	< 1	Normal	< 1	< 1
Resolution	1	1	Rectangular	1	1
Standard Uncertainty (k=2)				< 10	< 10

5.4. CHARACTERIZATION OF SHIELDED ROGOWSKI COIL

Characterization of RC is determined by several factors such as linearity, the influence of the conductor position, influence of return current conductor, and temperature dependency. The calibration system in Chapter 5.2.3 was used for RC characterization. The RC was installed a well-defined current path for the conductor position test also for the return current conductor test in the calibration setup. Thus, the variations in mutual inductance of RC due to the conductor position was reduced considerably and repeatable measurements were achieved before and after the magnetic shield. The results are presented in the following chapter. Then, the magnetically shielded RC was sent to VTT for determining of the temperature dependence of the RC. To reduce the temperature dependence of the shielded RC, temperature compensation was applied by connecting the definite terminating resistor to the output of the coil. The effects of conductor position and nearby return conductor were also studied by VTT. The results are given in the certificate published by VTT in Appendix A.

5.4.1. Calibration Setup

After the calibration of non-conventional measuring bridge, the calibration method using the ECT mode of WM3000I was chosen to perform a linearity test, a position of primary conductor and a return conductor test as it contains fewer references and is more practical. The calibration setup is shown in Figure 5.13.

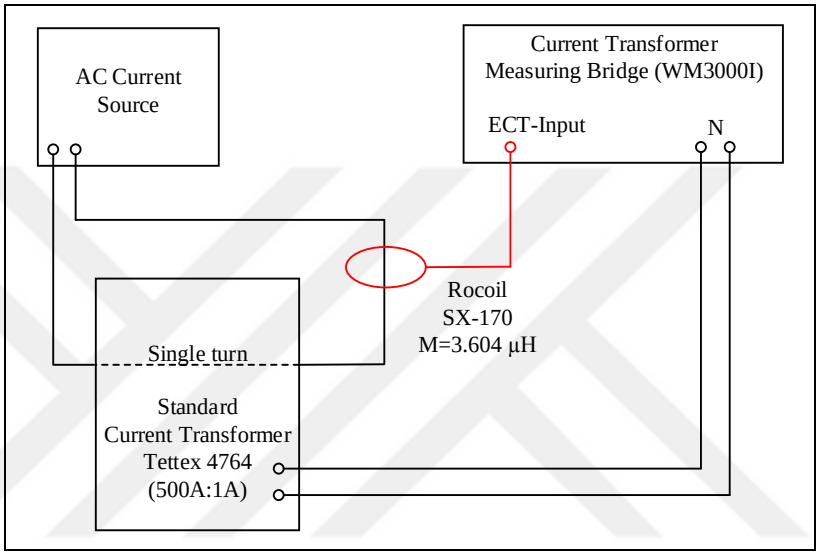

Figure 5.13. Calibration setup for calibrating of RC

Before the magnetic shield, the calibration of SX-170 Rogowski Coil was performed by applying appropriate primary current to the RC and the standard current transformer from AC current source, and by directly measuring the ratio error and phase displacement values of the RC with the measuring bridge. The bridge compares the output voltage of RC with the secondary current of standard current transformer. After applying the magnetic shield to the SX-170 Rogowski coil, the magnetically shielded RC was again calibrated by using the same calibration setup. The view of the calibration setup is shown in Figure 5.14. The design details and characterization test results of the magnetically shielded RC were given in Reference [66].

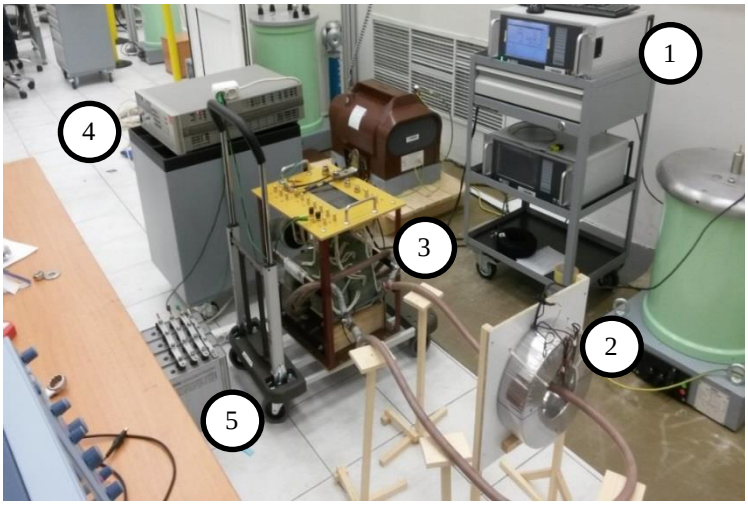

1. Measuring Bridge (WM3000I)

2. Magnetically Shielded RC

3. Reference Current Transformer

4. AC Power Source

5. Capacitive Bank

Figure 5.14. View of calibration setup

5.4.2. Test Results

5.4.2.1. Linearity

One of the most important characteristics of the RC is the remarkable amplitude linearity since it has no magnetic material in the core. However, effects that are unusual and unknown may exist in the material of coil former. Source of these effects is most likely the core material, It is assumed that the core material has a uniform and a constant relative permeability. Impurity, even in very small amounts, can alter the permeability of the core, and as a result, create nonlinearities in the amplitude response.

RC was calibrated at various values from 50 A to 500 A while the primary conductor was placed in the center of the RC for determining the coil linearity. This measurement was performed for two cases, before and after magnetic shielding, and the results are presented in Table 5.8.

The ratio error of the RC has changed from 0.024 percent to 0.018 percent for 500 A of primary current after the magnetic shield is applied. The reason for this variation between the measured ratio errors before and after the magnetic shield can be due to the tightening of RC since the manufacturer declares that “With an SX-76 coil, for example, a gap error of

0.3 mm would introduce an output error of less than 0.1 percent. The phase is not affected even by a much larger gap" [55].

Table 5.8. Linearity test results

Primary Current (A)	Before Magnetic Shield		After Magnetic Shield	
	Ratio Error (%)	Phase Error (crad)	Ratio Error (%)	Phase Error (crad)
50	0.024	-0.002	0.015	-0.004
100	0.025	-0.004	0.015	-0.004
150	0.025	-0.004	0.016	-0.001
200	0.025	-0.004	0.016	-0.002
250	0.025	-0.004	0.018	-0.002
300	0.024	-0.004	0.019	-0.001
400	0.025	-0.004	0.019	-0.001
500	0.024	-0.004	0.018	-0.001

Based on the measurement results, the linearity of RC does not change between 50 A and 500 A by more than ±0.002 percent. The coil has still had very good linearity after the magnetic shield when the total measurement uncertainty limits are considered.

5.4.2.2. Influence of a Position of Feeding Conductor

RC has a sensitivity to the position of feeding conductor since the cross-sectional area of each turn in the coil is not the same with others, the turn density is not uniform around the coil and the coil shape is not the same everywhere in the coil. The sensitivity to the position of feeding conductor was studied separately for before and after the magnetic shield. A conductor with a 20 mm diameter is passed through the coil. The setup is shown in Figure 5.15. The reference value was determined when the conductor is passed through the center of the coil. Then the conductor was moved to four directions until it touched the coil. The ratio error and phase displacement of the RC were measured at d = 85 mm (equal to 0.5 x the inner coil radius) and d = 105 mm. d is the distance between positions 2 and 4 which are located around the core.

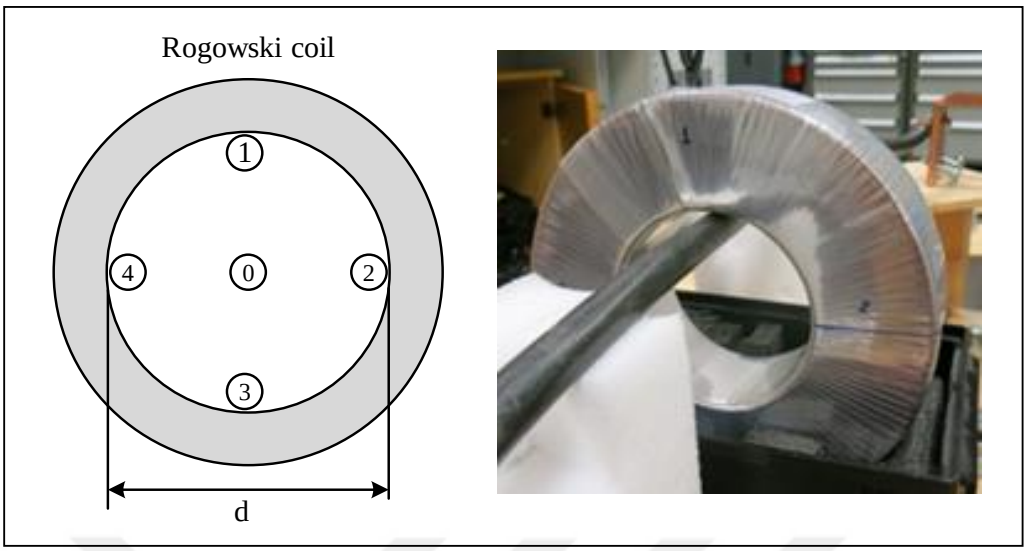

Figure 5.15. Setup for measuring of sensitivity to the position of feeding conductor

The primary conductor current was set to 400 A at 50 Hz. Results of the positional tests are given in Table 5.9 and in Table 5.10 for before and for after magnetic shielding, respectively. Before the magnetic shield, the maximum deviation was defined as -0.088 percent between where the conductor is touching the winding and reference point where the conductor is in the center of the coil. After the magnetic shield, the deviation was dramatically decreased to 0.001 percent. A very good improvement has been achieved for the influence of the position of current conductor.

Table 5.9. Positional test of feeding conductor before magnetic shield

I_p = 400A Freq : 50 Hz	**Ratio Error (%)**	**Phase Error (crad)**	**Ratio Error (%)**	**Phase Error (crad)**	**Ratio Error (%)**	**Phase Error (crad)**	**Ratio Error (%)**	**Phase Error (crad)**
Pos No:	***d* = 85 mm**		***d* = 105 mm**		***d* = 85 mm**		***d* = 105 mm**	
0	0.025	-0.004	0.025	-0.004	Deviations from Pos. 0			
1	-0.008	-0.004	-0.027	-0.004	-0.033	0.000	-0.052	0.000
2	-0.008	-0.004	-0.063	-0.004	-0.033	0.000	-0.088	0.000
3	0.071	-0.004	0.105	-0.004	0.046	0.000	0.080	0.000
4	-0.003	-0.004	-0.037	-0.004	-0.028	0.000	-0.062	0.000

Table 5.10. Positional test of feeding conductor after magnetic shield

I_p = 400A Freq : 50 Hz	**Ratio Error (%)**	**Phase Error (crad)**	**Ratio Error (%)**	**Phase Error (crad)**
Pos No:	***d* = 85 mm**			
0	0.018	-0.001	Deviations from Pos. 0	
1	0.018	-0.001	0.000	0.000
2	0.018	-0.001	0.000	0.000
3	0.018	-0.001	0.000	0.000
4	0.019	-0.001	0.001	0.000

5.4.2.3. Influence of a Return Current Conductor

A similar exercise was repeated to examine how the closeness of return conductor interacts with the measured current. The test setup is shown in Figure 5.16. The position of the return current conductor with 2 cm diameter was varied from 20 cm where it is touching the coil to 80 cm with 20 cm steps. The feeding current was set as 400 A at 50 Hz. For each distance, the errors of the RC were measured separately for before and after magnetic shielding and the results of ratio error and phase displacements are given in Table 5.11 and Table 5.12, respectively.

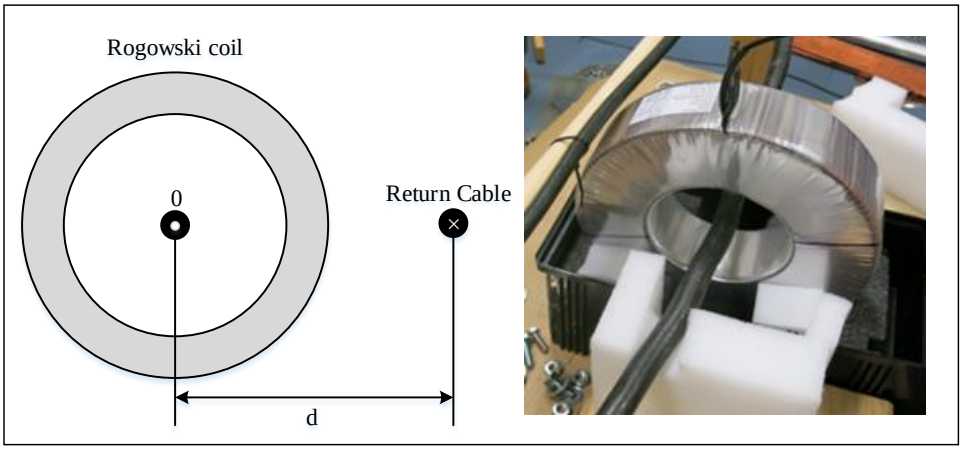

Figure 5.16. Setup for measuring of sensitivity to nearby current conductor

The reference point was selected where the return current conductor was 80 cm away from the coil center. Next, variations were calculated by subtracting the values of ratio error and phase displacement at any distance from the values of the reference point. Before the magnetic shield, the maximum deviation was defined as -0.022 percent when the return current conductor is 20cm from the center of the RC. After the magnetic shield, the deviation was sharply reduced to 0.001 percent.

Table 5.11. Positional of nearby primary conductor before magnetic shield

Primary Current : 400 A Frequency :50 Hz			**Ratio Error (%)**	**Phase Displacement (crad)**
***d* (cm)**	**Ratio Error (%)**	**Phase Displacement (crad)**	**Variation from *d*=80 cm**	
80	0.022	-0.004		
60	0.022	-0.004	0.000	0.000
40	0.017	-0.004	-0.005	0.000
20	0.000	-0.004	-0.022	0.000

Table 5.12. Positional of nearby primary conductor after magnetic shield

Primary Current : 400 A Frequency :50 Hz			**Ratio Error (%)**	**Phase Displacement (crad)**
***d* (cm)**	**Ratio Error (%)**	**Phase Displacement (crad)**	**Variation from *d*=80 cm**	
80	0.018	-0.001		
60	0.018	-0.001	0.000	0.000
40	0.018	-0.001	0.000	0.000
20	0.019	-0.001	0.001	0.000

5.4.2.4. Temperature Dependence of Magnetically Shielded Rogowski Coil

The output of magnetically shielded RC is influenced by a temperature dependence since the coil material expands as its temperature rises and the winding resistance of the coil changes with the temperature. An additional load resistor is connected to the coil output in parallel in order to reduce the temperature dependence of the RC. Thereby, a resistive voltage divider is built by the coil winding resistance and the load resistor. The output of divider has no variation as temperature is changed. The contribution of the additional load resistor to the frequency response of the can be ignored at power frequencies [67].

First tests were carried out to specify an existing temperature dependence of the magnetically shielded RC designed in the dissertation when the temperature compensation was not made. And then, further tests were performed by connecting several load resistors to the coil in parallel and by placing them into a temperature bath in order to specify the value of additional load resistor for the lowest temperature dependence of the coil. The coil was operated eight hours for each test in the temperature bath. Measurement results are shown with/without the temperature compensation in Figure 5.17 and Figure 5.18, respectively. The temperature is shown with the red curve, the mutual inductance of the coil with the blue curve. The optimal value of the additional load resistor was found as 9.5 kΩ.

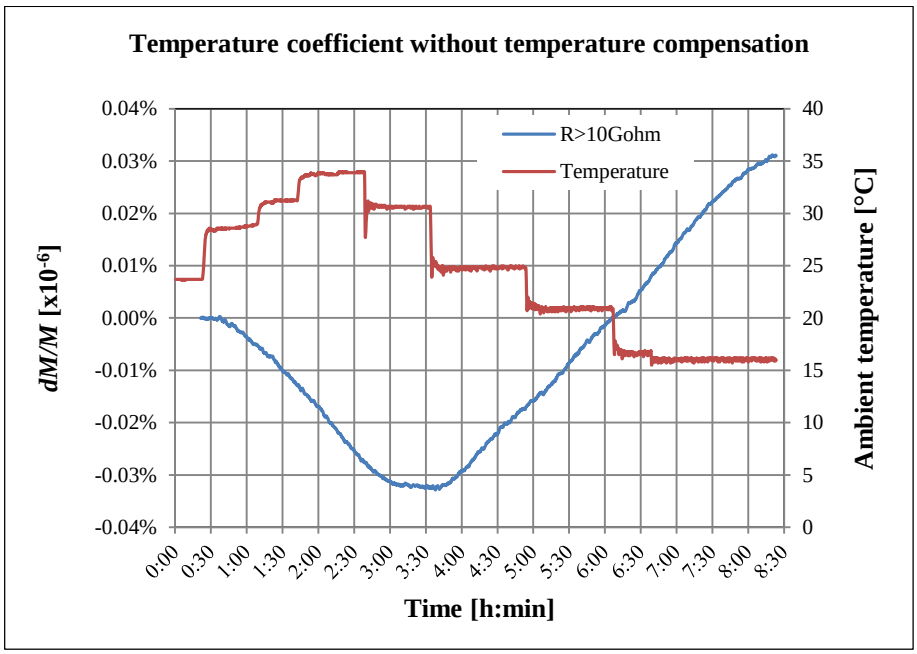

Figure 5.17. Temperature coefficient of the coil without temperature compensation

This work was performed by VTT in the scope of EMRP project, ENG61 “Nonconventional voltage and current sensors for future power grids”. Necessary permissions were obtained from them to share the measurement results in the dissertation.

The temperature coefficient of the coil was measured as 41 ppm/K when temperature compensation was not made. After connecting to a resistor of 9.5 kΩ for temperature compensation, the temperature coefficient of the coil was decreased to 3 ppm/K over a temperature range of 16°C - 36°C. A very good achievement is obtained for the temperature dependence of the magnetically shielded RC.

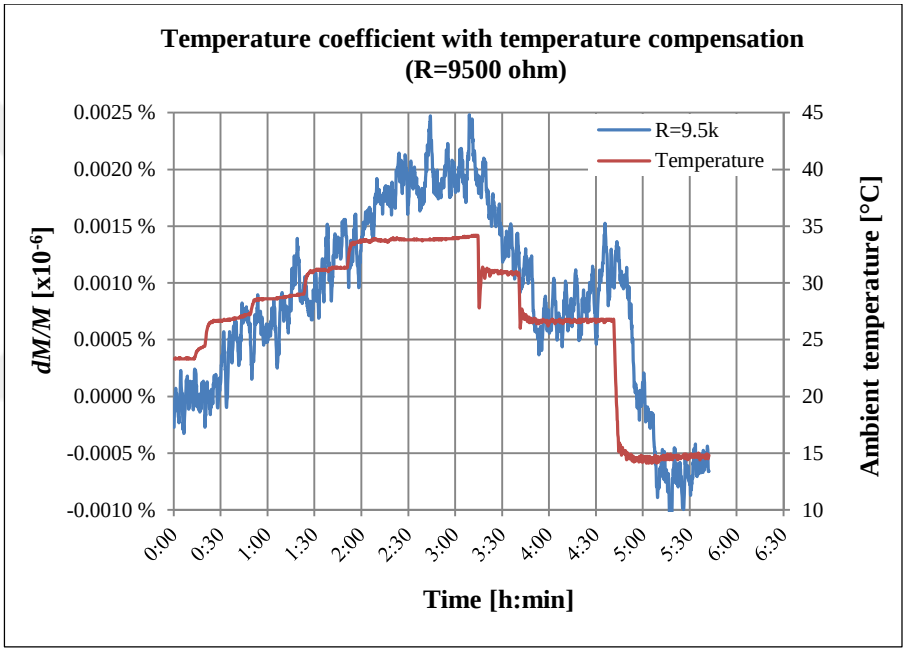

Figure 5.18. Temperature coefficient of the coil with temperature compensation

5.4.2.5. Demonstration of Magnetically Shielded Rogowski Coil On Medium Voltage

The magnetically shielded RC designed in this dissertation was used in order to calibrate a current transformer medium voltage level as a reference. The calibration was carried out by applying the rated primary currents both the current transformer to be calibrated and the coil, and measuring the ratio error and phase displacement between the secondary signals of the transformer and the coil with the measuring bridge for non-conventional current transformers. The measuring arrangement is shown in Figure 5.19.

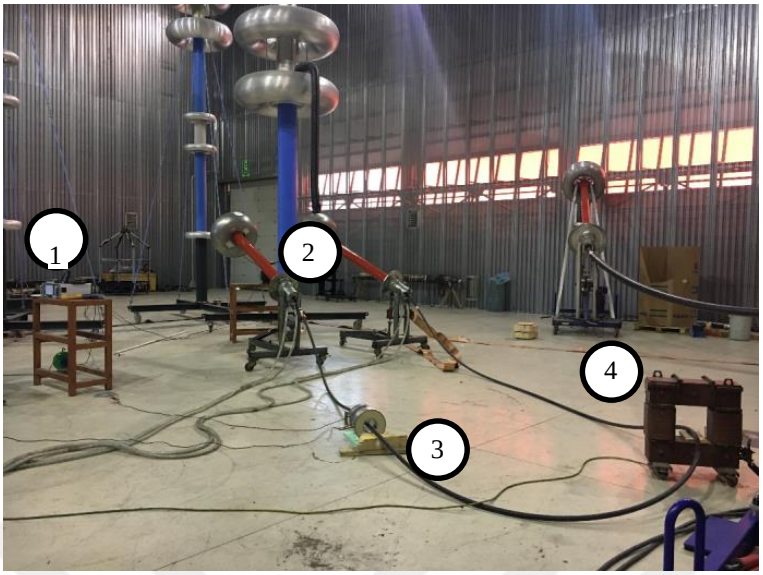

1. Measuring Bridge (WM3000I)

2. Current Transformer Under Test

3. Reference magnetically shielded RC

4. AC Current Generator

Figure 5.19. On-site calibration of current transformers using the RC

With applying magnetic shielding to the coil, the influences of magnetic coupling of a position of current conductor and a return current conductor were determined to be less than 10 μA/A. The temperature dependence of the shielded RC was found to be less than 5 ppm / K (18°C - 21 °C) by adding a resistor of 9.5 kΩ to its output.

The uncertainty of the measurement system was calculated and the budget is given in Table 5.13. The uncertainty components are grouped into two categories; Type A: repeatability (n = 10 measurements) and Type B: the coil, the measuring bridge, effects of magnetic coupling, linearity and influences of temperature change.

Table 5.13. Uncertainty budget

Uncertainty Sources	**Ratio (μA/A)**	**Phase (μrad)**
Shielded RC	20	20
WM3000I (ECT Mode)	80	70
Linearity	5	5
Effect of conductor position	5	2
Effect of external magnetic field	10	3
Ambient Temperature	5	5
Repeatability	20	30
Expanded Uncertainty	100	100

The ambient temperature in the laboratory was kept at 19 °C ± 2 °C since a temperature variation may cause the changes on the mutual inductance of RC in spite of being temperature compensated. The uncertainties for the ratio error and phase displacement measurements were calculated as 100 μA/A and 100 μrad, respectively. The uncertainties do not include the long-term behavior of the RC. The standard uncertainty of measurements were determined in accordance with [59] and [60]. Measurement results with the declared uncertainty values are given in the calibration certificate in Appendix A. The reported expanded uncertainty of measurement is stated as the standard uncertainty of measurement multiplied by the coverage factor k = 2, which for a normal distribution corresponds to a coverage probability of approximately 95 percent [68].

6. CONCLUSION

Investigation of parameter changes for the magnetic shielding of RCs and current comparators are important for both the analysis and the design of these devices. Although the FEM analysis is more accurate, it requires considerable computer capability and time when parameter effects are studied. However, methods such as the proposed magnetic circuit models yield comparable results, as has been shown in the dissertation, and they may find application in the analysis and design of RCs and current comparators.

In this dissertation, improved magnetic circuit models are developed by considering the hollow cylindrical structure of the magnetic shield, unlike a rectangular shell assumption in literature, to compute the magnetic shielding effectiveness of RCs with horizontal and vertical air gaps. These robust models are verified by the FEM simulations and they are capable of calculating the magnetic shielding effectiveness within a reasonable accuracy for a wide range of design parameters. The maximum relative errors between the magnetic circuit model and the FEM simulations are found to be 27 percent for horizontal air gaps and 17 percent for vertical air gaps when shielding thicknesses and shielding distances are varied from 5 mm to 30 mm in the hollow cylindrical structure. Moreover, for changes in air gaps, in relative permeability of the shielding material, and in radius of a hollow cylindrical structure, the model accuracy does not exceed 21 percent relative error.

The magnetic circuit approach has also been tested with the hollow toroidal magnetic shielding structure. Although the hollow toroidal magnetic shielding has a circular cross-sectional view and therefore, lengths are not well defined, an acceptable accuracy is obtained by the developed method. The errors in magnetic shielding effectiveness do not exceed 18 percent for the same parameter range considered for the cylindrical structure. These works are original in this field.

In the light of this knowledge, the hollow cylindrical magnetic shield is applied to RC to improve its immunity against the coupling of external magnetic fields and its sensitivity to the position of current feeding conductor. Two additional windings are used to avoid the saturation of the magnetic shield. These windings, having the same number of turns and locating inside and outside the magnetic shield, are wound in series-opposition so that their ampere-turns are canceled.

Unique measurement systems are developed for the calibration of non-conventional current sensors by using several devices to scale current and voltages to traditional levels, and then to compare with the standards/references either traditional measuring bridges or using new sampling-based systems. The evaluation of these calibration systems is carried out by considering their measurement uncertainty. The modified calibration system with laboratory standards and the use of commercial measuring bridge for non-conventional current sensors are better suited for calibration laboratories although they don't have the best uncertainty. The sampling-based calibration system is best suited for National Metrology Institutes due to the added flexibility and having the lowest uncertainty. An innovative work is performed to calibrate commercial measuring bridge for non-conventional current sensors. The bridge is calibrated with the expanded uncertainty of 10 μA/A and 10 μrad (k = 2) for ratio and phase error measurements, respectively.

By applying the magnetic shield, the immunity of new design RC to the primary conductor position, and pick-up from nearby current-carrying conductors or from other interference sources has been reduced to less than 10 μA/A, and the phase displacement less than ±2 μrad regardless the conductor position within temperature range from 15 to 35 °C up to 600 A. The immunity of new design RC has been improved 100 times. The performance of the new design coil with temperature compensation techniques is demonstrated in power calibration setup on medium voltage. In the literature, the best measurement uncertainty value of 150 μA/A for CT calibrations where RCs are used as reference is reduced to less than 100 μA/A with the temperature compensated RC.

The drawbacks of the design are increased weight, and limited current range compared with RCs without shielding. Further work is still needed to increase the current range of new design RC to 2000 A.

REFERENCES

1. Chattock AP. On a magnetic potentiometer. *Philosophical Magazine Series 5*. 1887; 24:94-96.

2. Rogowski W, Steinhaus W. Die messung der magnetischen spannung. *Archiv für Elektrotechnik*. 1912; 1(4):141-150.

3. Kojovic LA, Beresh R, Bishop MT, Radek J, Bruce M, McLaren P, et al. Practical aspects of Rogowski coil applications to relaying. Technical report. IEEE Power System Relaying Committee. 2010.

4. Ramboz JD. Machinable Rogowski coil, design, and calibration. *IEEE Transactions on Instrumentation and Measurement*. 1996; 45(2):511 – 515.

5. Ward DA. Calibrating Rogowski Coils [cited 2020 1 April]. Available from: https://www.mikrocontroller.net/attachment/111221/Rogowski_Coils.pdf.

6. Ward DA. Alternating current measuring devices. UK Patent, 2 034 487 A; 1980.

7. Skendzic V, Kesler JR. Precision Rogowski coil and method for manufacturing same. US Patent, 7,227,441; 2009.

8. Gris JP, Dupraz JP. Rogowski Coil. US Patent, 5,414,400; 1995.

9. Baudart C. Device for measuring an electrical current in a conductor using a Rogowski coil. US Patent, 5,442,280; 1995.

10. Kojovic LA. PCB Rogowski coils – High precision low power sensors. *CIGRE Session*; 2004: CIGRE.

11. Kojovic LA. Shielded Rogowski Coil Assembly and Methods. US Patent, US 2008/0106253 A1; 2008.

12. Karrer N, Hofer-Noser P. PCB Rogowski coils for high di/dt current measurement. *31st Annual Power Electronics Specialists Conference*; 2000; Galway, Ireland: IEEE.

13. Rea D, Kaye KL, Zawisa M. High precision Rogowski current transformer. US Patent, 7.579.824 B2; 2008.

14. Draxler K, Styblikova R. Magnetic shielding of Rogowski coils. *IEEE Transactions on Instrumentation and Measurement.*2018; 67(5):1207-1213.

15. Petersons O. A wide-range high voltage capacitance bridge with one ppm acuracy. *Ph.D. dissertation, George Washington Univ., Washington, DC*. Feb., 1974.

16. Kusters NL, Moore WJM. The development and performance of current comparators for audio frequencies. *IEEE Transactions on Instrumentation and Measurement*. 1965; IM-14(4):178 - 190.

17. Miljanic PN, Kusters NL, Moore WJM. The development of the current comparator, a high accuracy ac ratio measuring device. *Transactions of the American Institute of Electrical Engineers, Part I: Communication and Electronics*. 1962; 81(5):359 - 368.

18. Souders TM. Transformer-like devices for high-accuracy ac current measurements. Technical Report. National Institute of Standards and Technology (NIST-1473). 2008.

19. Moore WJM, Miljanic PN. *The Current comparator*. London: Peter Perengrinus; 1988.

20. Ren S, Ding H, Li M. Analysis and calculation of magnetic shielding effectiveness for comparators. *Conference on Precision Electromagnetic Measurements (CPEM)*; 1994: IEEE.

21. Ren S, Ding H, Li M, She S. Magnetic shielding effectiveness for comparators. *IEEE Transaction on Instrumentatiton and Measurement*. 1995; 44(2):422-424.

22. Zhang Z, Ren S. The numerical calculation of magnetic shielding effectiveness of comparator based on FEM. *Conference on Precision Electromagnetic Measurements (CPEM)*; 2000: IEEE.

23. Kyriazis GA. The effectiveness of current-comparator magnetic shields against leakage fields at power frequencies. *Conference on Precision Electromagnetic Measurements (CPEM)*; 2002: IEEE.

24. Wang X, Ren S. Calculating magnetic shielding effectiveness for high-power DC comparator by magnetic circuit method. *Journal of Chongqing University*. 2013; 6(2):113-118.

25. Shao H, Qu K, Lin F, Liang B. Magnetic shielding effectiveness of current comparator. *IEEE Transactions on Instrumentation and Measurement*. 2013; 62(6):1486-1490.

26. Ren S, Guo S, Liu X, Liu Q. Shielding effectiveness of double-layer magnetic shield of current comparator under radial disturbing magnetic field. *IEEE Transactions On Magnetics*. 2016; 52(10):Art. No.: 9401907.

27. Zhang Z, Ren S, Zhou X. FEM analysis of shielding effectiveness of magnetic shield of comparator by ANSYS program. *Conference on Precision Electromagnetic Measurements (CPEM)*; 2002; Ottawa, Ontario, Canada: IEEE.

28. Ren S, Yang H, Zhong D. The study of both two-and three-dimensional models of magnetic shielding effectiveness for comparators. *Conference on Precision Electromagnetic Measurements (CPEM)*; 2004; London, UK: IEEE.

29. Djokić B. The design and calibration of Rogowski coils. *NCSLI Measure*. 2009; 4(2):62-75.

30. Instrument transformers – Part 8: Electronic current transformers. IEC technical committe 38. Instrument transformers; DIN EN 60044-8:2003-6.

31. Draxler K, Styblikova R, Hlavacek J, Prochazka R. Calibration of Rogowski coils with an integrator at high currents. *IEEE Transactions on Instrumentation and Measurement*. 2011; 60(7):2434 - 2438.

32. Draxler K, Styblikova R. Calibration of Rogowski coil [cited 2020 1 June]. Available from: http://futuregrid.emrp.eu/wp-content/uploads/2016/09/F12-Calibration-of-Rogowski-coils.pdf.

33. Suomalainen EP, Hällström J. Experience with current transformer calibration system based on Rogowski Coil. *Conference on Precision Electromagnetic Measurements (CPEM)*; 2018; Paris, France: IEEE.

34. Suomalainen EP, Hällström J. Onsite calibration of a current transformer using a Rogowski coil. *IEEE Transactions on Instrumentation and Measurement*. 2009; 58(4):1054-1058.

35. IEEE Guide for the Application of Rogowski Coils Used for Protective Relaying Purposes. IEEE Power System Relaying and Control Committee; IEEE C37.235™:2007.

36. Kim YH, Jung JK, Kang JH, Lee SH, Han SO. Establishment of 40,000 A Rogowski coil calibration system and its uncertainty analysis. *Conference on Precision Electromagnetic Measurements (CPEM)*; 2010; Daejeon, South Korea: IEEE.

37. Çaycı H, Kefeli T. A calibration system for electronic current transformer with analog outputs. *III. International Metrology Conference*; 2010; Cairo, Egypt: CAFMET.

38. B.Djokić. Calibration of Rogowski coils at power frequencies using digital sampling. *IEEE Transactions on Instrumentation and Measurement*. 2009; 58(4):751 - 755.

39. B.Djokić. Calibration of Rogowski coils at frequencies up to 10 kHz using digital sampling. *IEEE Transactions on Instrumentation and Measurement*. 2010; 59(5):1303 - 1308.

40. Houtzager E, Mohns E, Fricke S, Ayhan B, Kefeli T, Çaycı H. Calibration systems for analogue non-conventional voltage and current transducers. *Conference on Precision Electromagnetic Measurements (CPEM)*; 2016; Ottawa, Canada: IEEE.

41. Ayhan B, Çaycı H, Mohns E, Houtzager E. Calibration system for analogue, non-conventional ECTs and EVTs operational and characterized. Techinal report. National Metrology Institute of Turkey (TÜBİTAK UME). 2016.

42. Christian J, Mohns E, Alessandro M, Houtzager E, Ayhan B. Recommendations related to the calibration and testing of nonconventional current and voltage sensors [cited 2020 1 June]. Available from: http://futuregrid.emrp.eu/wp-content/uploads/2017/08/FutureGrid-GPG-Calibration-of-non-conventional-sensors.pdf.

43. Mohns E, Mortara A, Cayci H, Houtzager E, Fricke S, Agustoni M, et al. Calibration of commercial test sets for non-conventional instrument transformers. *International Workshop on Applied Measurements for Power Systems (AMPS)*; 2017; Liverpool, UK: IEEE.

44. Ramboz JD, Flach DR. High-current measurement technique. Technical Report. Gaithersburg, MD, USA: National Institute of Standards and Technology (NBSIR 84-2881). 1984.

45. Miljanic PN. Mutual inductance highly independent of primary winding position and ambient fields. *IEEE Transactions on Instrumentation and Measurement*. 1997; 46(2):471-473.

46. Ferković L, Ilić D. Mutual inductance of a precise Rogowski coil in dependence of the position of primary conductor. *IEEE Transactions on Instrumentation and Measurement*. 2009; 58(1):122 - 128.

47. Chekurov Y, Hällström J. Influence of busbar geometry on ac current measurement using Rogowski coil. *Conference on Precision Electromagnetic Measurements (CPEM)*; 2008; Broomfield, CO, USA: IEEE.

48. Suomalainen EP, Hällström J. Uncertainty estimate of a split-core Rogowski coil for high ac current. *Conference on Precision Electromagnetic Measurements (CPEM)*; 2010; Daejeon, Korea: IEEE.

49. Teppan W, Turpin P, Beguin M. IEC 61869 Compliant Rogowski Coil for Volume Production. *International Workshop on Applied Measurements for Power Systems (AMPS)*; 2016; Aachen, Germany: IEEE.

50. Liu X, Huang H, Cui Y, Dai Y, Liu X. Mutual inductance between arbitrary conductor and Rogowski coil with circular skeleton and gap compensation. *IEEE Sensors Journal*. 2019; 19(11):4106 - 4114.

51. Ayhan B, Uçak C. Improved magnetic circuit model for magnetic shielding effectiveness in Rogowski coil. *IEEE Transactions on Magnetics*. 2020; 56(3):Art. No.: 8500109.

52. Chua LO, Lin PM. Computer-Aided Analysis of Electronic Cicuits. 1st ed. New Jersey: Prentice-Hall; 1975.

53. Derbas HW, Williams JM, Koenig AC, Pekarek SD. A comparison of nodal- and mesh-based magnetic equivalent circuit models. *IEEE Transactions On Energy Conversion*. 2009; 24(2):388-396.

54. ANSYS. Academic Research EM, Release 19 Canonsburg, PA, USA: ANSYS; 2019.

55. Technical specification of 2100 Series rigid Rogowski coils [cited 2020 1 June]. Available from: https://www.rocoil.co.uk/Specification%20Rigid%20Coils.pdf.

56. Instrument transformers - Part 1: General requirements. IEC technical committe 38 - Instrument transformers; IEC 61869-1:2007-10.

57. Kefeli T. Design and manufacture of high-accuracy transconductance amplifier. Technical report. National Metrology Institute of Turkey (TÜBİTAK UME). 2016.

58. ZERA. WM3000U / WM3000I Measuring bridges for voltage transformers and current transformers [cited 2020 1 June]. Available from: https://www.zera.de/fileadmin/pdf_and_more/Products/Transformers/WM3000U-I_Pros_EXT_GB_V408.pdf.

59. Evaluation of measurement data — Guide to the expression of uncertainty in measurement (GUM) : BIPM [cited 2020 1 June]. Available from: https://www.bipm.org/utils/common/documents/jcgm/JCGM_100_2008_E.pdf.

60. Evaluation of the uncertainty of measurement in calibration : EA-4/02M [cited 2020 1 June]. Available from: https://european-accreditation.org/wp-content/uploads/2018/10/ea-4-02-m-rev01-september-2013.pdf.

61. Ayhan B, Canbolat U, Çaycı H, Turhan E. Precision voltage transformer for AC power measurement standard. *The 12th International Conference on Probabilistic Methods Applied to Power Systems (PMAPS)*; 2012; Istanbul, Turkey.

62. Brenncke C. Methods of instrument transformer testing are changing [cited 2020 1 June]. Available from: https://www.smart-energy.com/top-stories/methods-of-instrument-transformer-testing-are-changing/.

63. Çaycı H. A complex current ratio device for the calibration of current transformer test sets. *Metrology and Measurement Systems*. 2011; 18(1):159-164.

64. Voljc B, Lindic M, Pinter B, Svetik Z, Lapuh R. Direct measurement of AC current with coaxial current shunts down to 1 mA. *Conference on Precision Electromagnetic Measurements (CPEM)*; 2010; Daejeon, Korea: IEEE.

65. Voljc B, Lindic M, Lapuh R. Direct measurement of ac current by measuring the voltage drop on the coaxial current shunt. *IEEE Transactions on Instrumentation and Measurement*. 2009; 58(4):863-867.

66. Hällström J, Ayhan B, Suomalainen EP, Valero A. Improvement of Rogowski coil immunity against unwanted magnetic coupling effects. *The 20th International Symposium on High Voltage Engineering*; 2017; Buenos Aires, Argentina: ISH.

67. Lehtonen TA, Hällström J. Optimizing temperature coefficient and frequency response of Rogowski coils. *IEEE Sensors Journal*. 2017; 17(20):6646 - 6652.

68 Ayhan B. Uncertainty budget form for current sensors. National Metrology Institute of Turkey (TÜBİTAK UME). 2017. Report No.: FRM-05-G1PE-04-05.

APPENDIX A : CALIBRATION CERTIFICATES

Calibration Certificate of Magnetically Shielded Rogowski Coil published by MIKES

KALIBROINTITODISTUS
KALIBRERINGSBEVIS
CERTIFICATE OF CALIBRATION

Nro nr • no.	M-17E040
Tilaaja Uppdragsgivare • Customer	TUBITAK-UME Baris Mah. Dr. Zeki Acar Cad. No:1 41470 GEBZE, KOCAELI TURKEY
Kalibroitu laite Kalibrerat instrument • Calibrated instrument	Shielded Rogowski Coil
Valmistaja Tillverkare • Manufactured by	TUBITAK / Rocoil
Tyyppi Typ • Model	SX-170
Sarjanumero Serienummer • Serial number	MRC01
Kalibrointipäivä Kalibreringsdatum • Date of calibration	10.2.2017
Päiväys Datum • Date	4.4.2017
Allekirjoitukset Underskrifter • Signatures	Jari Hällström Senior Scientist Pekka Immonen Research Scientist
Sivu Sida • Page	1/3
Liitteitä Bilagor • Appendices	-

MIKES
Kansallinen mittanormaalilaboratorio
National Standards Laboratory
Mittatekniikan keskus, MIKES, Teknikantie 1, FI-02150 Espoo, FINLAND, tel +358 20 722 111
www.mikes.fi

Kalibroidun laitteen kunto
Kondition av kalibrerat instrument • Condition of calibrated instrument

No faults were observed in the condition of the calibrated device during the calibration.

Kalibrointimenetelmä
Kalibreringsmetod • Calibration method

Before calibration of the mutual inductance, the temperature dependence of the Rogowski coil was determined in order to find the optimal value for the terminating resistor for compensation of the temperature dependence. Results of these measurements are presented in appendix 1.

In addition, the linearity, the dependence on conductor position and the effect of nearby return conductor were studied. These results are shown in appendix 2.

For calibration of mutual inductance and phase displacement, AC current was generated using low harmonic distortion source /6/. Measurements were performed with four different frequencies between 50 Hz and 60 Hz. Primary current was measured with a current shunt /3/ and a sampling voltmeter /2/. Output voltage of the device under calibration was measured with another sampling voltmeter /1/. An external trigger generator /5/ locked to local 10 MHz reference frequency was used to synchronize the two voltmeters.

Mutual inductance and phase displacement of the Rogowski coil were measured with the temperature compensation resistor box connected in parallel with the coil. The optimized terminating resistor value was 9.4857 kΩ ± 0.1 Ω.

Phase displacement and ratio error were defined according to IEC61869-2:2012 from the measured data. Calibration was performed according to working instruction MIK-S254.

Kalibroinnissa käytetyt mittanormaalit ja jäljitettävyys
Mätnormalerna som använts i kalibrering och spårbarhet • Measurement standards used in calibration and traceability

Reference standards:

/1/ sampling voltmeter, Hewlett Packard 3458A, sn. 2823A11980 (MIKES000697);
/2/ sampling voltmeter, Hewlett Packard 3458A, sn. 2823A22375 (MIKES004192);
/3/ current shunt, 100 mΩ (MIKES000022).

Auxiliary devices:

/4/ Rogowski coil (MIKES004923):
/5/ function generator, Agilent Technologies 33220A, sn. MY44025438 (MIKES005062):
/6/ Multi-Product Calibrator, Fluke 5520A, sn. 7250208 (MIKES000116).

Reference standards are traceable to Finnish national standards of DC-voltage and resistance.

Kalibrointiolosuhteet
Kalibreringsförhållanden • Calibration conditions

Temperature in the calibration laboratory was (23 ± 2) °C and relative humidity (40 ± 5) %.

JEH
PI

Kalibrointitulokset ja mittausepävarmuus
Kalibreringsresultat och mätosäkerhet • Calibration results and measurement uncertainty

Calibration results for the mutual inductance and phase displacement are in Table 1.

While calculating the uncertainty of the calibration, the following sources were considered:
- uncertainty of the ratio measured with sampling voltmeters /1,2/;
- deviation of the measuring results; and
- uncertainty of current shunt /3/.

The long term stability effects of the device under calibration are not included.

Estimate of the uncertainty is multiplied by the coverage factor $k = 2$, which for normal distribution corresponds to a coverage probability of approximately 95 %. The measurement uncertainty has been estimated according to the JCGM 100:2008 guide "Evaluation of measurement data – Guide to the expression of uncertainty in measurement".

Table 1. Calibration results with 9.4857 kΩ temperature compensation resistor connected. Applied current is 7 A.

Frequency [Hz]	Mutual inductance [µH]	Uncertainty [µH]	Phase Displacement[1] Diff. from π/2 [crad]	Uncertainty [crad]
50	3.56323	0.00006	0.035	0.002
53	3.56322	0.00004	0.037	0.002
55	3.56321	0.00004	0.038	0.002
60	3.56321	0.00004	0.041	0.002

[1] According to IEC 61869-2:2012 Instrument transformers - Part 2: Additional requirements for current transformers

Huomautukset
Anmärkningar • Remarks

PI JKH

Appendix 1: Temperature dependence and current linearity studies

Temperature dependency

The temperature dependence of a Rogowski coil can be reduced by about factor of ten by adding a suitable load resistor to its output, which will also affect the frequency response of the coil. The temperature effect of the Rogowski coil was studied by inserting the coil in a thermal chamber, and changing the temperature from 15 °C to 35 °C. Time constant of the Rogowski coil is several hours.

Measurements were performed with the 0.8 A current and 60 Hz frequency. Current was generated using audio amplifier (Sony, STR-DG510). Effective current was increased by using a multiple current turns (N=32), and for the Rogowski coil under investigation it was 25 A. Measurements were performed without load resistor with 9.4857 kΩ ± 0.1 Ω load resistor. Measurement results are shown in Figures A.1.1-A1.5

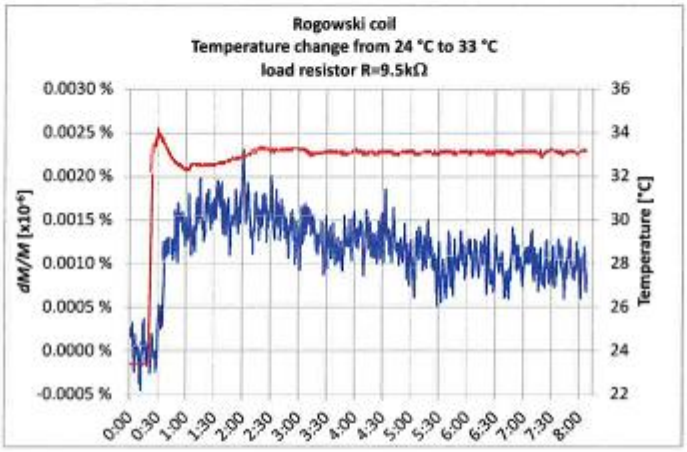

Figure A1.1. Measured temperature dependence of the Rogowski coil with 9.5 kΩ load resistor. Blue: mutual inductance, red: temperature.

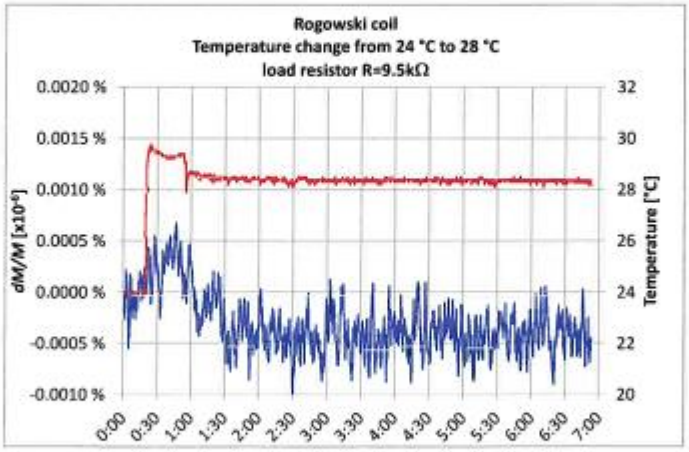

Figure A1.2. Measured temperature dependence of the Rogowski coil with 9.5 kΩ load resistor. Blue: mutual inductance, red: temperature.

P1 JKU

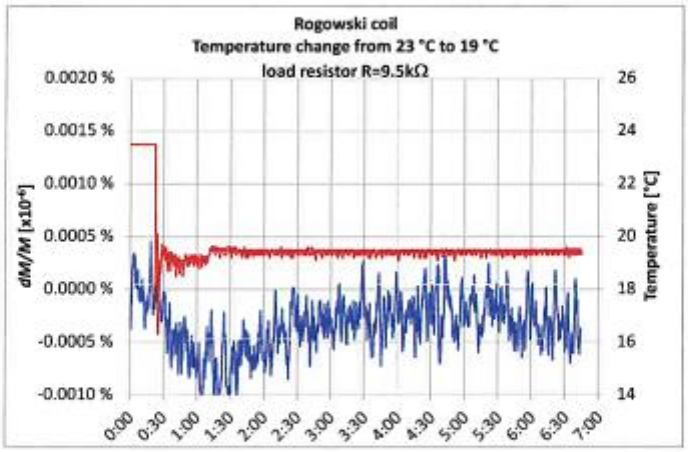

Figure A1.3. Measured temperature dependence of the Rogowski coil with 9.5 kΩ load resistor. Blue: mutual inductance, red: temperature.

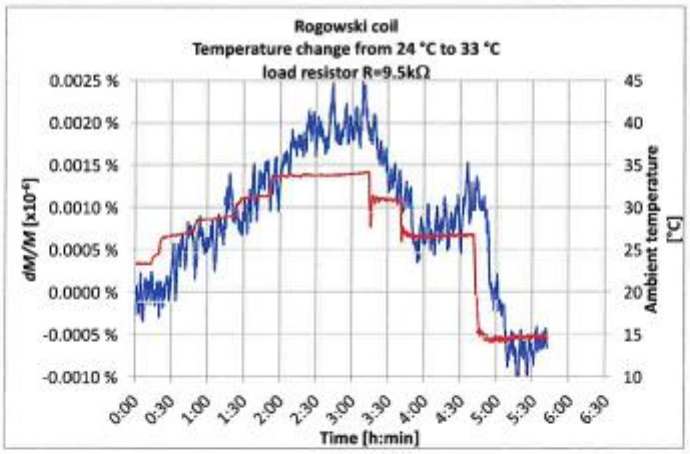

Figure A1.4. Measured temperature dependence of the Rogowski coil with 9.5 kΩ load resistor. Blue: mutual inductance, red: temperature.

PI JKY

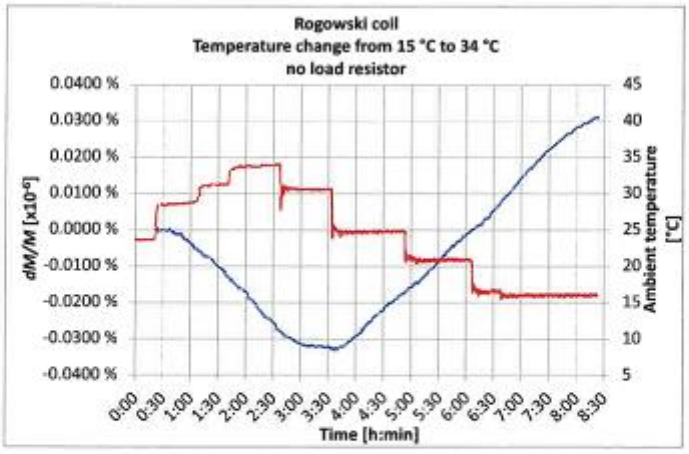

Figure A1.5. Measured temperature dependence of the Rogowski coil without load resistor. Blue: mutual inductance, red: temperature.

Current nonlinearity

Current nonlinearity was measured up to 600 A with 60 Hz frequency against a reference Rogowski coil. Measurement result is shown in Figure A1.6.

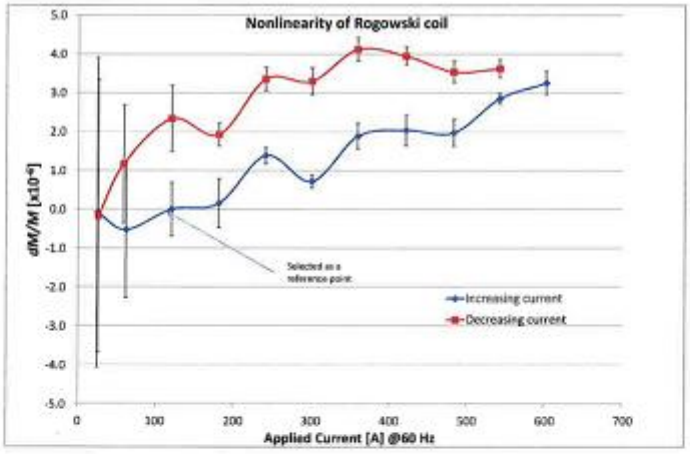

Figure A1.6. Current (60 Hz) linearity of the temperature compensated split-core coil compared with MIKES reference Rogowski coil. Error bars show one standard deviation of the measurement result.

PI JKH

Appendix 2: Conductor position and return conductor proximity effect studies

Conductor position study

These measurements were performed using Rogowski coil of MIKES (MIKES004923) as the reference. The measurements were carried out on 23.11.2016.

The injected current was 60 A with 55 Hz frequency. The tested positions were as defined in Figure A2.1. Results of the measured position dependence are given in Table A2.1 and in the graph of Figure A2.2.

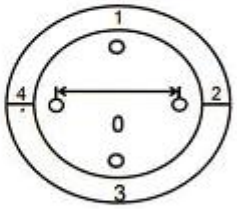

a)

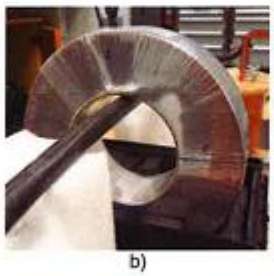

b)

Figure A2.1. a) Conductor position description. Conductor diameter 20 mm. Reference position is the centre of the coil window. Distance of positions 2-4 (and 1-3) is 105 mm.
b) Photograph of setup in position 1.

Table A2.1. Results of the measured differences in mutual inductance and phase displacement.

Position No:	dM/M [%]	Standard deviation [%]	Phase displacement [crad]	Standard deviation [crad]
0	0.00000	0.00004	0.00000	0.00003
1	0.00026	0.00006	-0.00002	0.00005
2	0.00016	0.00005	-0.00012	0.00007
3	-0.00008	0.00004	-0.00013	0.00008
4	-0.00012	0.00006	-0.00003	0.00006

PI JEK

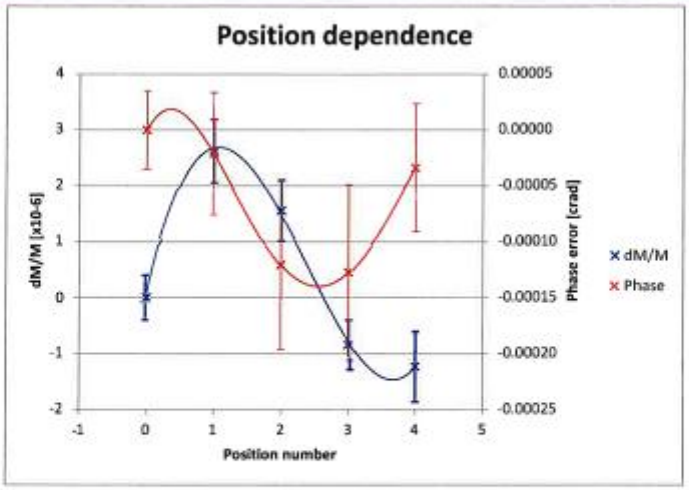

Figure A2.2. Measured conductor position dependences of mutual inductance and phase error with centre position (0) as a reference.

Return conductor proximity effect

These measurements were performed on 25.1.2017. To minimize the effect of conductor positions on the reference, a current transformer and a shunt resistor were used instead of the Rogowski reference coil.

The change of measured mutual inductance and phase error was determined by moving the return current conductor to different distances from the coil centre as described in Figure A2.3.

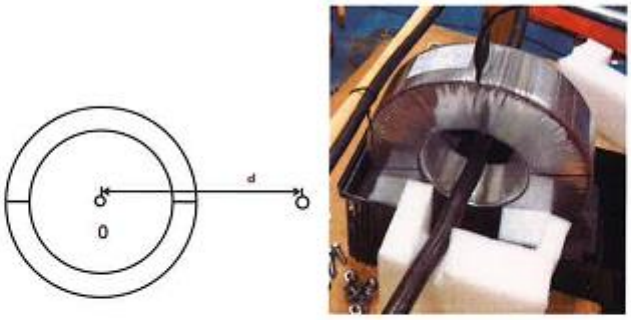

a) b)

Figure A2.3. a) Return conductor position description. Distance d = 80 cm from the centre of the coil window as used as the reference for other measurements. b) Photograph of the setup with d = 20 cm .

Dependence of mutual inductance and phase error on the distance was measured with 80 A current at 55 Hz and 53 Hz frequencies. Results of the measurements are given in Table A2.2 and in graphical form in Figure A2.4.

PI JKA

Table A2.2. Results for ratio and phase error dependence on position of the return conductor.

Primary current [A]	Frequency [Hz]	d [cm]	dM/M [x10^{-6}]	Standard deviation [x10^{-6}]	Phase error [crad]	Standard deviation [crad]
77.7	55	21	-5.5	4.4	-0.00016	0.00083
77.2	55	40	-1.2	2.9	-0.00019	0.00049
77.1	55	60	0.1	2.4	-0.00012	0.00031
77.5	55	80	0.0	2.6	0.00000	0.00040
75.1	55	98	-1.9	0.9	0.00006	0.00103
80.4	55	127	-0.6	0.9	-0.00012	0.00047
80.3	53	20	-4.7	4.0	-0.00005	0.00064
80.4	53	40	0.0	1.4	0.00006	0.00049
80.3	53	60	0.1	2.4	0.00027	0.00012
80.4	53	80	0.0	5.1	0.00000	0.00037
80.2	53	100	-1.6	2.2	0.00017	0.00038
80.2	53	128	-0.7	3.0	-0.00002	0.00013

PI JeH

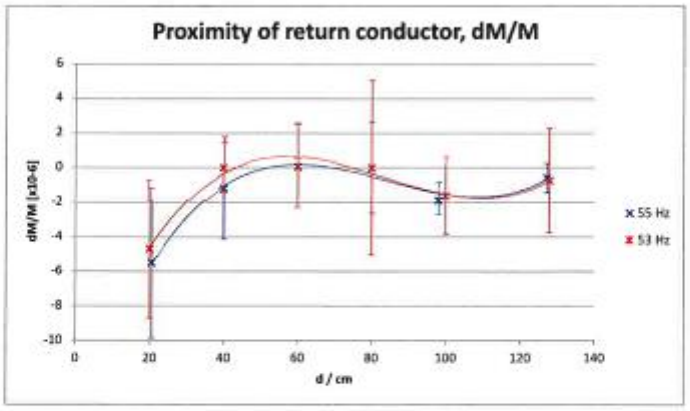

a)

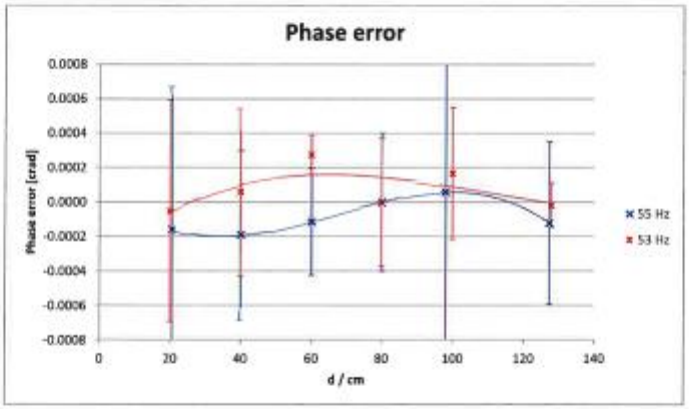

b)

Figure A2.4. Measured dependences of mutual inductance and phase error on proximity of the return conductor. Distance of 80 cm from the centre of Rogowski coil window is used as a reference for each frequency.

PI JKH

Calibration Certificate of Current Transformer by Using Magnetically Shielded Rogowski Coil as a Reference.

TÜBİTAK
UME

TÜBİTAK
ULUSAL METROLOJİ ENSTİTÜSÜ

TÜBİTAK
UME
G1PE-0059
03-17

Kalibrasyon Sertifikası
Calibration Certificate

Cihazın Sahibi / Adresi *Customer / Address*	:	**TÜBİTAK UME GÜÇ VE ENERJİ LABORATUVARI** *TÜBİTAK Gebze Yerleşkesi 41470 Gebze - KOCAELİ*
İstek Numarası *Order No*	:	**2017.00929**
Makine / Cihaz *Instrument / Device*	:	**Akım Transformatörü** *Current Transformer*
İmalatçı *Manufacturer*	:	**ALCE**
Tip *Type*	:	**AK36**
Seri Numarası *Serial Number*	:	**2004/12532**
Kalibrasyon Tarihi *Date of Calibration*	:	**23.03.2017**
Sayfa Sayısı *Number of Pages*	:	**6**

Bu kalibrasyon sertifikası, Uluslararası Birimler Sistemi'nde (SI) tanımlanmış birimleri gerçekleştiren ulusal ölçüm standartlarına izlenebilirliği belgeler. TÜBİTAK UME, CIPM nezdinde Karşılıklı Tanıma Düzenlemesi'ne (MRA) taraf bir kuruluştur.
This calibration certificate documents traceability to national standards, which realize units of measurement according to the International System of Units (SI). TÜBİTAK UME is a signatory of the CIPM Mutual Recognition Arrangement (MRA).

Ölçüm sonuçları, genişletilmiş ölçüm belirsizlikleri ve kalibrasyon metotları bu sertifikanın tamamlayıcı kısmı olan takip eden sayfalarda verilmiştir.
Measurement results, expanded measurement uncertainties and calibration methods are given on the following pages, which are part of this certificate.

27.04.2017
Tarih
Date

Dr. Mustafa ÇETİNTAŞ
Enstitü Müdürü
Director

TÜBİTAK Gebze Yerleşkesi PK 54 41470 Gebze-Kocaeli / TÜRKİYE T +90 262 679 50 00 F +90 262 679 50 01 www.ume.tubitak.gov.tr

Makine / Cihaz
Instrument / Device

Cihaz Adı *Instrument Name*	**Üretici Firma** *Manufacturer*	**Tip / Model** *Type/Model*	**Ölçme Aralığı / Uygun Tanımlama** *Measurement Range / Convenient Description*
Akım Transformatörü *Current Transformer*	ALCE	AK36	Primer Akım : 100 A *Primary Current* Sekonder Akım : 5 A *Secondary Current* Gerilim Seviyesi : 36 kV *Voltage Level* Sınıf : 0,5 *Class* Frekans : 50 Hz *Frequency*

Kalibrasyonun Yapıldığı Yer
Location

Kalibrasyon, DEMİRER Kablo'ya ait yüksek gerilim laboratuvarında gerçekleştirilmiştir. Adres: 4 Eylül Mahallesi, İsmet İnönü Caddesi, No: 279, Bozüyük 11300, Bilecik, Türkiye.

The calibration was performed at the high voltage laboratory of DEMİRER Cable factory. Address: 4 Eylül Mahallesi, İsmet İnönü Caddesi, No: 279, Bozüyük 11300, Bilecik, Türkiye.

Cihazın Laboratuvara Kabul Tarihi
Date of Receipt of the Device

-

Kalibrasyonda Kullanılan Referans Cihaz(lar)
Reference(s) Used in Calibration

No	**Cihaz Adı** *Instrument Name*	**Üretici Firma** *Manufacturer*	**Tip / Model** *Type/Model*	**Seri No** *Serial No*	**İzlenebilirlik** *Traceability*
1	Ekranlı Rogowski Bobini *Shielded Rogowski Coil*	TÜBİTAK UME	SX-170	MRC01	MIKES, M-17E040, 10.02.2017
2	Akım Transformatörü Karşılaştırma Köprüsü *Current Transformer Test Set*	ZERA	WM3000I	070000037	UME, G1PE-0016, 07.03.2017

Sayfa 3 / 6 *Page*	**TÜBİTAK** **ULUSAL METROLOJİ ENSTİTÜSÜ** NATIONAL METROLOGY INSTITUTE	TÜBİTAK UME G1PE-0059 03-17

Kalibrasyon Yöntemi ve Prosedürü

Calibration Method and Procedure

36 kV orta gerilim seviyesi altındaki akım transformatörü ekranlı Rogowski bobini kullanılarak TÜBİTAK UME tarafından yerinde kalibre edilmiştir. Akım transformatörünün kalibrasyonu, TLM-05-G1PE-04-05 "Akım Transformatörü Kalibrasyon Talimatı"na göre, kalibre edilen akım transformatörü ve ekranlı Rogowski bobinine aynı primer akımın uygulanması, transformatör ve bobinin sekonder sinyalleri arasındaki oran hatası ve faz kayması değerlerinin akım transformatörü karşılaştırma köprüsü ile ölçülmesi suretiyle gerçekleştirilmiştir. Ölçüm düzeneği Şekil 1'de verilmiştir. Ölçümler ekranlı Rogowski bobininin sıcaklık bağımlılığını düşürmek için belirlenen 9,4857 kΩ ± 0,1 Ω yük direnci ile birlikte gerçekleştirilmiştir.

Kalibrasyon sonuç tablolarında, I_P primer akımı, I_S ise sekonder akımı göstermektedir.

The current transformer under 36 kV medium voltage level was calibrated on-site by TÜBİTAK UME using the shielded Rogowski coil. The calibration was performed by applying appropriate primary currents both to the current transformer to be calibrated and the shielded Rogowski coil, and measuring the ratio and phase displacement between the secondary signals of the transformer and the coil with the test set for non-conventional current transformers. The measuring arrangement is shown in Figure 1. Measurements were performed with 9.4857 kΩ ± 0.1 Ω load resistor which was determined to reduce the temperature coefficient of the shielded Rogowski coil.

Primary and secondary currents are represented by I_P and I_S respectively in the calibration results table.

Şekil 1. Akım transformatörünün yerinde kalibrasyonu ölçüm düzeneği

Figure 1. Setup for On-site calibration of current transformer

Çevre Şartları

Environmental Conditions

Sıcaklık : (20 ± 2) °C
Temperature

Bağıl Nem : (40 ± 10) %rh
Relative Humidity

Sayfa 4 / 6 *Page*	**TÜBİTAK** **ULUSAL METROLOJİ ENSTİTÜSÜ** NATIONAL METROLOGY INSTITUTE	TÜBİTAK UME G1PE-0059 03-17

Kalibrasyon Sonuçları
Calibration Results

Kalibrasyon sonuçları değer olarak Tablo 1'de, grafiksel olarak Şekil 2 ve 3' te verilmiştir.
The calibration results are given in Table 1and graphically in Figure 2 and 3.

Tablo 1. Oran Hatası ve Faz Kayması Ölçümleri (50 Hz)
Table 1. Measurements of Ratio Error and Phase Displacement

UYGULANAN DEĞER *Applied Value*			**YÜK** *Burden*	**ORAN HATASI** *Ratio Error* (%)	**FAZ KAYMASI** *Phase Displacement* (crad)
I_P : 100 A	I_S : 5 A	%120 x I_P	Yüksüz *No Burden*	0,424	0,111
		%100 x I_P		0,422	0,119
		%50 x I_P		0,413	0,150
		%20 x I_P		0,393	0,203
		%5 x I_P		0,343	0,337

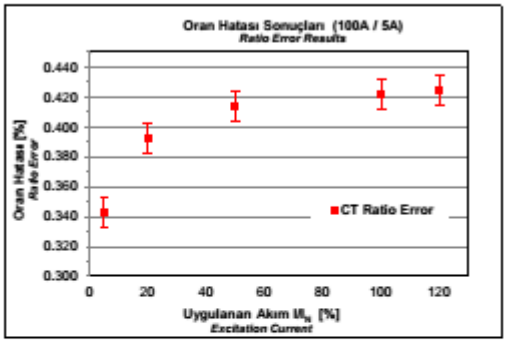

Şekil 2. Oran hatası sonuçları
Figure 2. Ratio error results

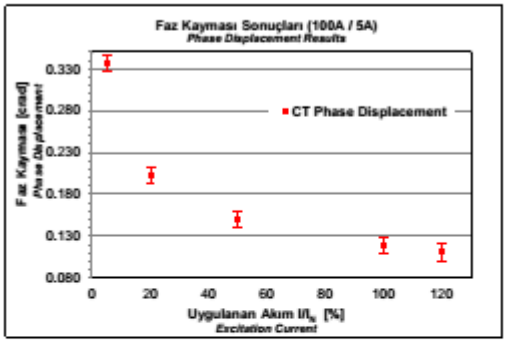

Şekil 3. Faz kayması sonuçları
Figure 3. Phase displacement results

Ölçüm Belirsizliği
Measurement Uncertainty

Ölçüm sisteminin belirsizlik bütçesi Tablo 2' de verilmiştir. Belirsizlik değerleri, oran hatası ve faz kayması ölçümleri için sırasıyla % 0,010 ve 0,010 crad olarak belirlenmiştir. Belirsizlik değerleri, kalibre edilen cihazın uzun dönem kararlılığını ve hatasını içermemektedir.

Beyan edilen genişletilmiş ölçüm belirsizliği, standart ölçüm belirsizliğinin normal dağılım için yaklaşık % 95 güvenilirlik seviyesini sağlayan k = 2 kapsam faktörü ile çarpımının sonucudur. Standart ölçüm belirsizliği GUM ve EA-4/02 dokümanlarına uygun olarak belirlenmiştir.

Tablo 2. Belirsizlik Bütçesi
Table 2. Uncertainty Budget

Belirsizlik Kaynakları *Uncertainty Sources*	Oran Hatası *Ratio Error*	Faz Kayması *Phase Displacement*
	(ppm)	(μrad)
Ekranlı Rogowski Bobini *Shielded Rogowski Coil*	20	20
Karşılaştırma Köprüsü ve kayma *WM3000I (ECT Part) and drift*	50	50
Doğrusallık *Linearity*	5	5
Primer iletken pozisyon etkisi *Effect of conductor position*	5	2
Dış manyetik alan etkisi *Effect of external magnetic field*	10	3
Ortam sıcaklığı *Ambient Temperature*	5	5
Tekrarlanabilirlik *Repeatability*	20	10
Genişletilmiş Belirsizlik *Expanded Uncertainty*	**85 ppm % 0,0085**	**83 μrad 0,0083 crad**

The uncertainty budget of the measurement system is given in Table 2. The uncertainties for the ratio error and phase displacement measurements are as 0.010 % and 0.010 crad respectively. The uncertainties do not include the long-term behaviour of the calibration object

The reported expanded uncertainty of measurement is stated as the standard uncertainty of measurement multiplied by the coverage factor k = 2, which for a normal distribution corresponds to a coverage probability of approximately 95%. The standard uncertainty of measurement has been determined in accordance with GUM and EA-4/02.

Görüşler, Açıklamalar ve Uygunluk Beyanı

Comments, Remarks and Statement of Compliance

Kalibrasyon sonuçları sadece kalibrasyonu yapılan Akım Transformatörüne aittir. Cihazın performansı için gerekli çevre şartlarında kullanımından ve uygun aralıklarla kalibre edilmesinin sağlanmasından kullanıcı sorumludur.

The results of the calibration refer only to the calibrated Current Transformer at the time of calibration. The user is responsible to have the instrument recalibrated at appropriate intervals and using at the required environmental conditions.

Kalibrasyonu Yapan(lar) * *Performed By*	**Laboratuvar Sorumlusu *** *Head of the Laboratory*
Burak AYHAN	Hüseyin ÇAYCI
Tevfik Fikret ARMAĞAN	

* Elektronik olarak onaylanmıştır.
Approved electronically.

Calibration Certificate of Current Transformer Bridge (ECT part of measurements is given)

TÜBİTAK
UME

CIPM MRA

TÜRKAK
TÜRK AKREDİTASYON KURUMU
TURKISH ACCREDITATION AGENCY
tarafından akredite edilmiş

TÜRKAK
Kalibrasyon
TS EN ISO IEC 17025
AB-0034-K

TÜBİTAK
ULUSAL METROLOJİ ENSTİTÜSÜ

AB-0034-K
UME G1PE-0005
01-16

Kalibrasyon Sertifikası
Calibration Certificate

Cihazın Sahibi / Adresi *Customer / Address*	:	**SAUDI STANDARDS, METROLOGY AND QUALITY ORGANIZATION OF THE KINGDOM OF SAUDI ARABIA (SASO)** *Riyadh 11471, P.O. Box 3437 KINGDOM of SAUDI ARABIA*
İstek Numarası *Order No*	:	**2015.02150**
Makine / Cihaz *Instrument / Device*	:	**Akım Transformatörü Karşılaştırma Köprüsü** *Current Transformer Test Set*
İmalatçı *Manufacturer*	:	**Zera**
Tip *Type*	:	**WM3000I**
Seri Numarası *Serial Number*	:	**070000036**
Kalibrasyon Tarihi *Date of Calibration*	:	**25.01.2016 - 26.01.2016**
Sayfa Sayısı *Number of Pages*	:	**10**

Bu kalibrasyon sertifikası, Uluslararası Birimler Sistemi'nde (SI) tanımlanmış birimleri gerçekleştiren ulusal ölçüm standartlarına izlenebilirliği belgeler. TÜBİTAK UME, CIPM nezdinde Karşılıklı Tanıma Düzenlemesi'ne (MRA) taraf bir kuruluştur.
This calibration certificate documents traceability to national standards, which realize units of measurement according to the International System of Units (SI). TÜBİTAK UME is a signatory of the CIPM Mutual Recognition Arrangement (MRA).

Bu sertifika, CIPM tarafından hazırlanan Karşılıklı Tanıma Düzenlemesi (MRA) Ek C'de belirtilen yeteneklerle tutarlıdır. MRA kapsamında tüm katılımcı enstitüler, Ek C'de belirtilen büyüklükler, aralıklar ve ölçüm belirsizliklerini içeren sertifikaların geçerliliğini karşılıklı olarak tanır (ayrıntılar için bakınız http://www.bipm.org).
This certificate is consistent with the capabilities that are included in Appendix C of the MRA drawn up by the CIPM. Under the MRA, all participating institutes recognize the validity of each other's calibration and measurement certificates for the quantities, ranges and measurement uncertainties specified in Appendix C (for details see http://www.bipm.org).

Türk Akreditasyon Kurumu (TÜRKAK) kalibrasyon sertifikalarının tanınması konusunda Avrupa Akreditasyon Birliği (EA) ve Uluslararası Laboratuvar Akreditasyonu Birliği (ILAC) ile Karşılıklı Tanınma Anlaşması'nı imzalamıştır.
The Turkish Accreditation Agency (TÜRKAK) is signatory to the multilateral agreements of the European Cooperation for Accreditation (EA) and of the International Laboratory Accreditation Cooperation (ILAC) for the mutual recognition of calibration certificates.

Ölçüm sonuçları, genişletilmiş ölçüm belirsizlikleri ve kalibrasyon metotları bu sertifikanın tamamlayıcı kısmı olan takip eden sayfalarda verilmiştir.
Measurement results, expanded measurement uncertainties and calibration methods are given on the following pages, which are part of this certificate.

05.02.2016
Tarih
Date

Dr. Mustafa ÇETİNTAŞ Y.
Enstitü Müdürü
Director

TÜBİTAK Gebze Yerleşkesi PK 54 41470 Gebze-Kocaeli /TÜRKİYE T +90 262 679 50 00 F +90 262 679 50 01 www.ume.tubitak.gov.tr

Sayfa 2 / 10 *Page*	**TÜBİTAK** **ULUSAL METROLOJİ ENSTİTÜSÜ** NATIONAL METROLOGY INSTITUTE	AB-0034-K UME G1PE-0005 01-16

Makine / Cihaz
Instrument / Device

Cihaz Adı *Instrument Name*	**Üretici Firma** *Manufacturer*	**Tip / Model** *Type/Model*	**Ölçme Aralığı / Uygun Tanımlama** *Measurement Range / Convenient Description*
Akım Transformatörü Karşılaştırma Köprüsü *Current Transformer Test Set*	ZERA	WM3000I	Giriş Akımı : 1 mA...15 A *Input Current* Giriş Gerilimi (ECT) : 2,5 mV...18 V *Input Voltage* Ölçüm Bölgesi : % 0,2 - % 2 *Range* Frekans : 15 Hz - 65 Hz *Frequency*

Kalibrasyonun Yapıldığı Yer
Location

TÜBİTAK UME

Cihazın Laboratuvara Kabul Tarihi
Date of Receipt of the Device

25.01.2016

Kalibrasyonda Kullanılan Referans Cihaz(lar)
Reference(s) Used in Calibration

No	**Cihaz Adı** *Instrument Name*	**Üretici Firma** *Manufacturer*	**Tip / Model** *Type/Model*	**Seri No** *Serial No*	**İzlenebilirlik** *Traceability*
1	Standart Akım Transformatörü *Standard Current Transformer*	TETTEX	4764	146577	UME, G1PE-0210, 23.07.2014
2	Kompanzasyonlu Akım Komparatörü *Compansated Current Comparator*	TÜBİTAK UME	1200A CCC	G1PE-CCC-01	UME, Kullanım öncesi kalibrasyon *Self Calibration*
3	Üç Fazlı Standart Wattmetre / Enerjimetre *Three Phase Standard Wattmeter / Energymeter*	ZERA	COM303-1	98-701-4	UME, G1PE-0307, 29.05.2015
4	Akım Şöntü *Current Shunt*	SP	CS3B	CS3B-1104	UME, G1LR-0061, 26.04.2013

Kalibrasyon Yöntemi ve Prosedürü
Calibration Method and Procedure

Akım transformatörü karşılaştırma köprüsü, TLM-05-G1PE-04-07 "Akım Transformatörü Karşılaştırma Köprüsü Kalibrasyon Talimatı"na göre, bilinen oran hatası ve faz kayması değerlerinin akım transformatörü karşılaştırma köprüsüne uygulanması yöntemiyle gerçekleştirilmektedir.

Akım transformatörü karşılaştırma köprüsünün bir terminaline referans akım sinyali uygulanırken, diğer terminaline referans akım sinyalinden galvanik izolasyonu sağlanmış ve ihtiyaç duyulan oran hatası ve faz kayması elde edilmiş olan ikinci bir akım sinyali uygulanmaktadır.

The calibration of the current transformer test set has been performed according to TLM-05-G1PE-04-07 "Calibration Instruction of Current Transformer Bridge" by applying known ratio error and phase displacement values to the current transformer test set. A reference current signal is applied to the reference input of the current transformer bridge while a galvanically-isolated second current signal with known ratio error and phase displacement is applied to the other input.

Çevre Şartları
Environmental Conditions

Sıcaklık : (23 ± 1) °C
Temperature

Bağıl Nem : (45 ± 10) %rh
Relative Humidity

Sayfa 9 / 10 *Page*	**TÜBİTAK** **ULUSAL METROLOJİ ENSTİTÜSÜ** NATIONAL METROLOGY INSTITUTE	AB-0034-K / UME G1PE-0005 / 01-16

ORAN HATASI VE FAZ KAYMASI ÖLÇÜMLERİ (ECT) (60 Hz) (% 0,2)
Measurements of Ratio Error and Phase Displacement (ECT)

ÖLÇÜM BÖLGESİ *Range* I_N = 1 A U_{NECT} = 1 V	**UYGULANAN DEĞER** *Applied Value*		**ÖLÇÜLEN DEĞER** *Measured Value*		**FARK** *Difference*	
	Oran Hatası (ε) ve Faz Kayması (δ) *Ratio Error (ε) and Phase Displacement (δ)*					
I/I_N (%)	**ε, (%)**	**δ, (crad)**	**ε, (%)**	**δ, (crad)**	**ε, (%)**	**δ, (crad)**
100	0,000	0,000	0,000	-0,001	0,000	-0,001
100	0,200	0,000	0,200	-0,002	0,000	-0,002
100	0,200	-0,200	0,200	-0,201	0,000	-0,001
100	0,000	-0,200	0,000	-0,201	0,000	-0,001
100	-0,200	-0,200	-0,200	-0,201	0,000	-0,001
100	-0,200	0,000	-0,200	-0,001	0,000	-0,001
100	-0,200	0,200	-0,199	0,199	0,001	-0,001
100	0,000	0,200	0,001	0,199	0,001	-0,001
100	0,200	0,200	0,201	0,198	0,001	-0,002
50	0,000	0,000	0,002	-0,001	0,002	-0,001
50	0,200	0,000	0,202	-0,001	0,002	-0,001
50	0,200	-0,200	0,202	-0,201	0,002	-0,001
50	0,000	-0,200	0,002	-0,201	0,002	-0,001
50	-0,200	-0,200	-0,198	-0,201	0,002	-0,001
50	-0,200	0,000	-0,198	-0,001	0,002	-0,001
50	-0,200	0,200	-0,198	0,200	0,002	0,000
50	0,000	0,200	0,002	0,199	0,002	-0,001
50	0,200	0,200	0,202	0,198	0,002	-0,002
25	0,000	0,000	0,004	-0,001	0,004	-0,001
25	0,200	0,000	0,204	-0,002	0,004	-0,002
25	0,200	-0,200	0,204	-0,201	0,004	-0,001
25	0,000	-0,200	0,004	-0,201	0,004	-0,001
25	-0,200	-0,200	-0,196	-0,201	0,004	-0,001
25	-0,200	0,000	-0,196	-0,001	0,004	-0,001
25	-0,200	0,200	-0,196	0,199	0,004	-0,001
25	0,000	0,200	0,004	0,199	0,004	-0,001
25	0,200	0,200	0,204	0,198	0,004	-0,002
10	0,000	0,000	0,002	-0,004	0,002	-0,004
10	0,200	0,000	0,202	-0,007	0,002	-0,007
10	0,200	-0,200	0,200	-0,206	0,000	-0,006
10	0,000	-0,200	0,000	-0,204	0,000	-0,004
10	-0,200	-0,200	-0,200	-0,202	0,000	-0,002
10	-0,200	0,000	-0,198	-0,002	0,002	-0,002
10	-0,200	0,200	-0,195	0,199	0,005	-0,001
10	0,000	0,200	0,005	0,196	0,005	-0,004
10	0,200	0,200	0,205	0,193	0,005	-0,007
5	0,000	0,000	0,002	-0,003	0,002	-0,003
5	0,200	0,000	0,202	-0,005	0,002	-0,005
5	0,200	-0,200	0,200	-0,205	0,000	-0,005
5	0,000	-0,200	-0,001	-0,203	-0,001	-0,003
5	-0,200	-0,200	-0,201	-0,201	-0,001	-0,001
5	-0,200	0,000	-0,199	0,000	0,001	0,000
5	-0,200	0,200	-0,196	0,200	0,004	0,000
5	0,000	0,200	0,004	0,197	0,004	-0,003
5	0,200	0,200	0,204	0,194	0,004	-0,006

Sayfa 10 / 10 *Page*	**TÜBİTAK** **ULUSAL METROLOJİ ENSTİTÜSÜ** NATIONAL METROLOGY INSTITUTE	AB-0034-K UME G1PE-0005 01-16

Ölçüm Belirsizliği
Measurement Uncertainty

Belirsizlik değerleri, oran hatası ve faz kayması ölçümleri için sırasıyla % 0,005 ve 0,005 crad olarak belirlenmiştir. Belirsizlik değerleri, kalibre edilen cihazın uzun dönem kararlılığını ve hatasını içermemektedir.

Beyan edilen genişletilmiş ölçüm belirsizliği, standart ölçüm belirsizliğinin normal dağılım için yaklaşık % 95 güvenilirlik seviyesini sağlayan k = 2 kapsam faktörü ile çarpımının sonucudur. Standart ölçüm belirsizliği GUM ve EA-4/02 dokümanlarına uygun olarak belirlenmiştir.

The uncertainties for the ratio error and phase displacement measurements are as 0.005 % and 0.005 crad respectively. The uncertainties do not include the long-term behaviour of the calibration object.

The reported expanded uncertainty of measurement is stated as the standard uncertainty of measurement multiplied by the coverage factor k = 2, which for a normal distribution corresponds to a coverage probability of approximately 95%. The standard uncertainty of measurement has been determined in accordance with GUM and EA-4/02.

Görüşler, Açıklamalar ve Uygunluk Beyanı
Comments, Remarks and Statement of Compliance

Kalibrasyon sonuçları sadece kalibrasyonu yapılan Akım Transformatörü Karşılaştırma Köprüsü'ne aittir. Cihazın performansı için gerekli çevre şartlarında kullanımından ve uygun aralıklarla kalibre edilmesinin sağlanmasından kullanıcı sorumludur.

The results of the calibration refer only to the calibrated Current Transformer Test Set at the time of calibration. The user is responsible to have the instrument recalibrated at appropriate intervals and using at the required environmental conditions.

Kalibrasyonu Yapan(lar) * *Performed By*	**Laboratuvar Sorumlusu *** *Head of the Laboratory*
Burak AYHAN	Hüseyin ÇAYCI
Mustafa GÜNEŞ	

* Elektronik olarak onaylanmıştır.
Approved electronically.

APPENDIX B : TECHNICAL DRAWINGS

Unshielded Rogowski Coil

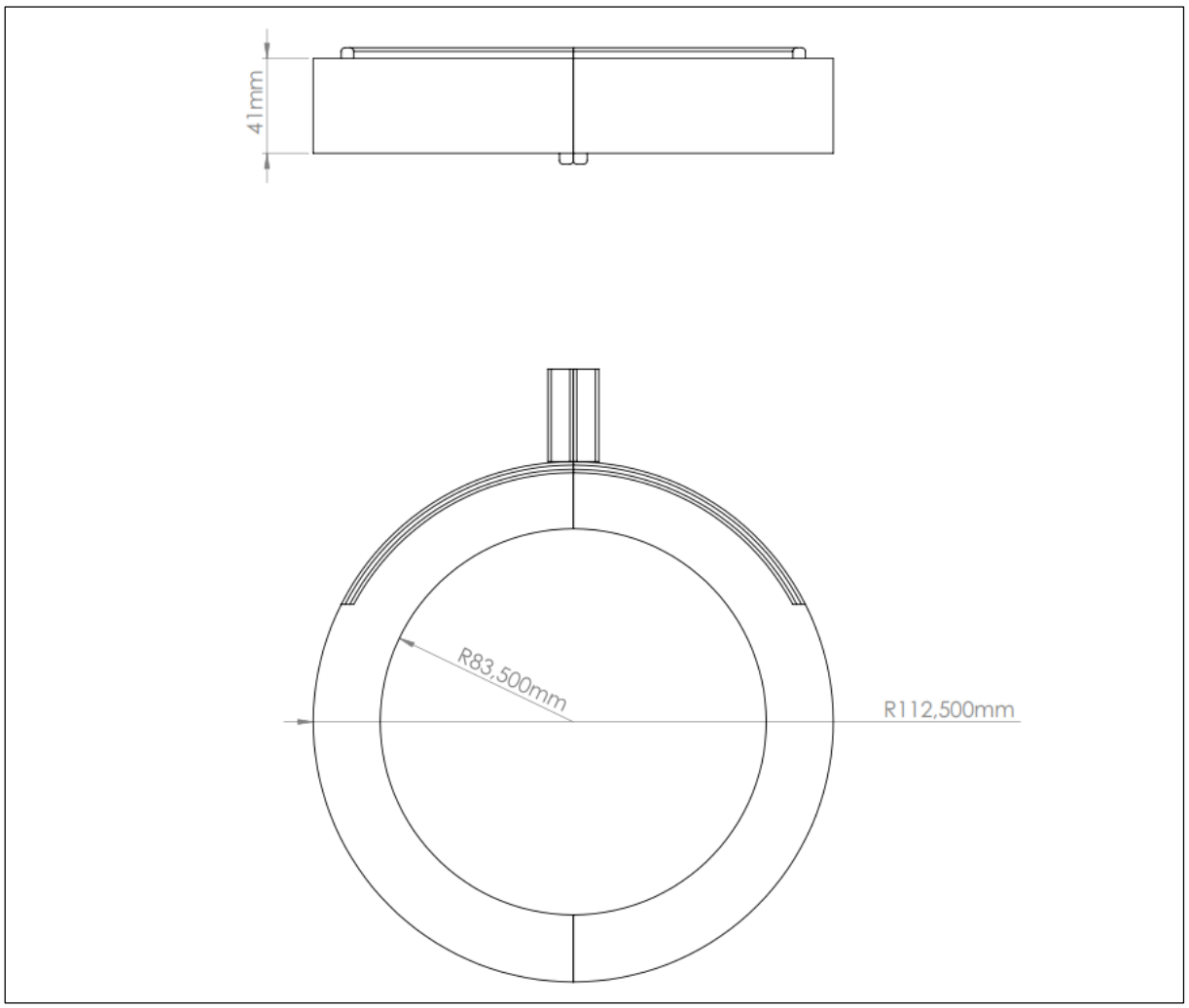

Inner Box

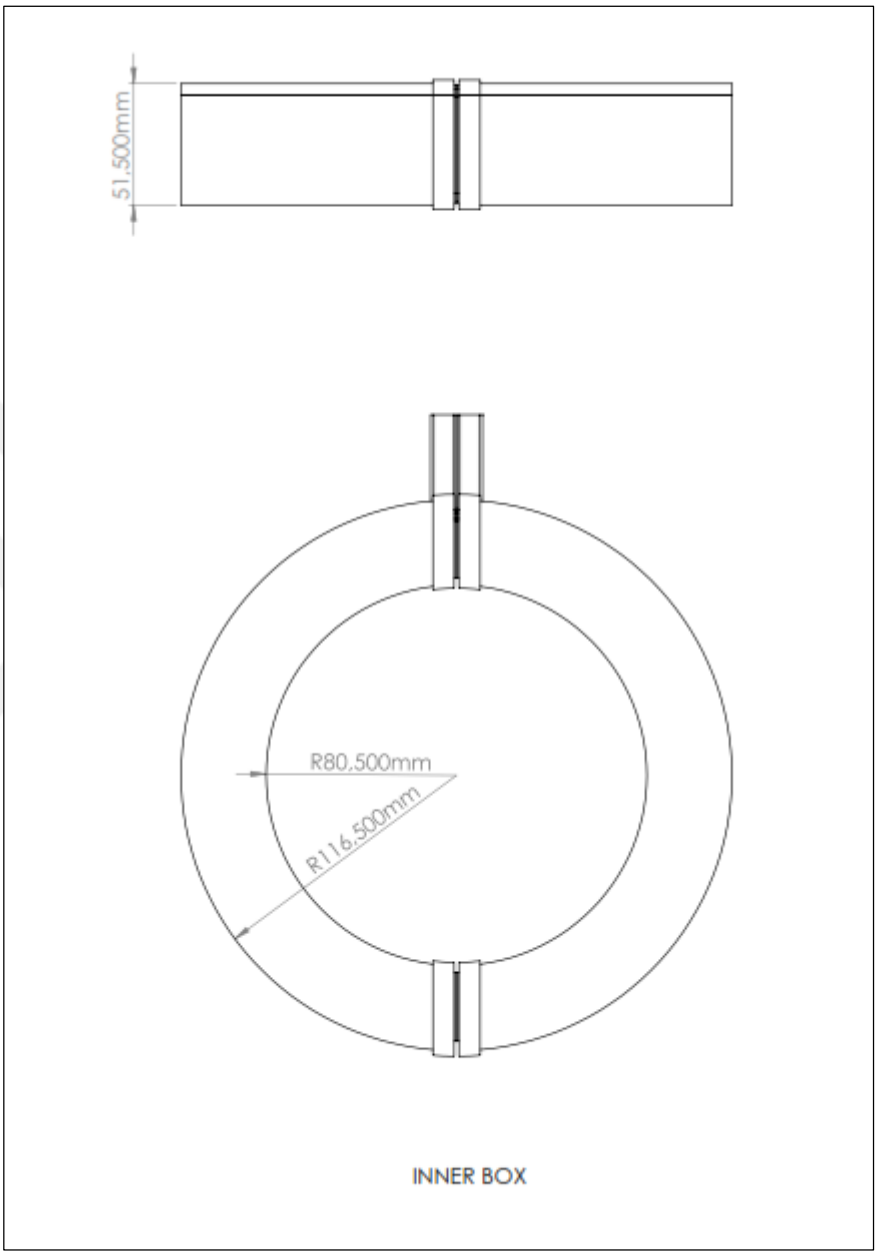

Inner Winding

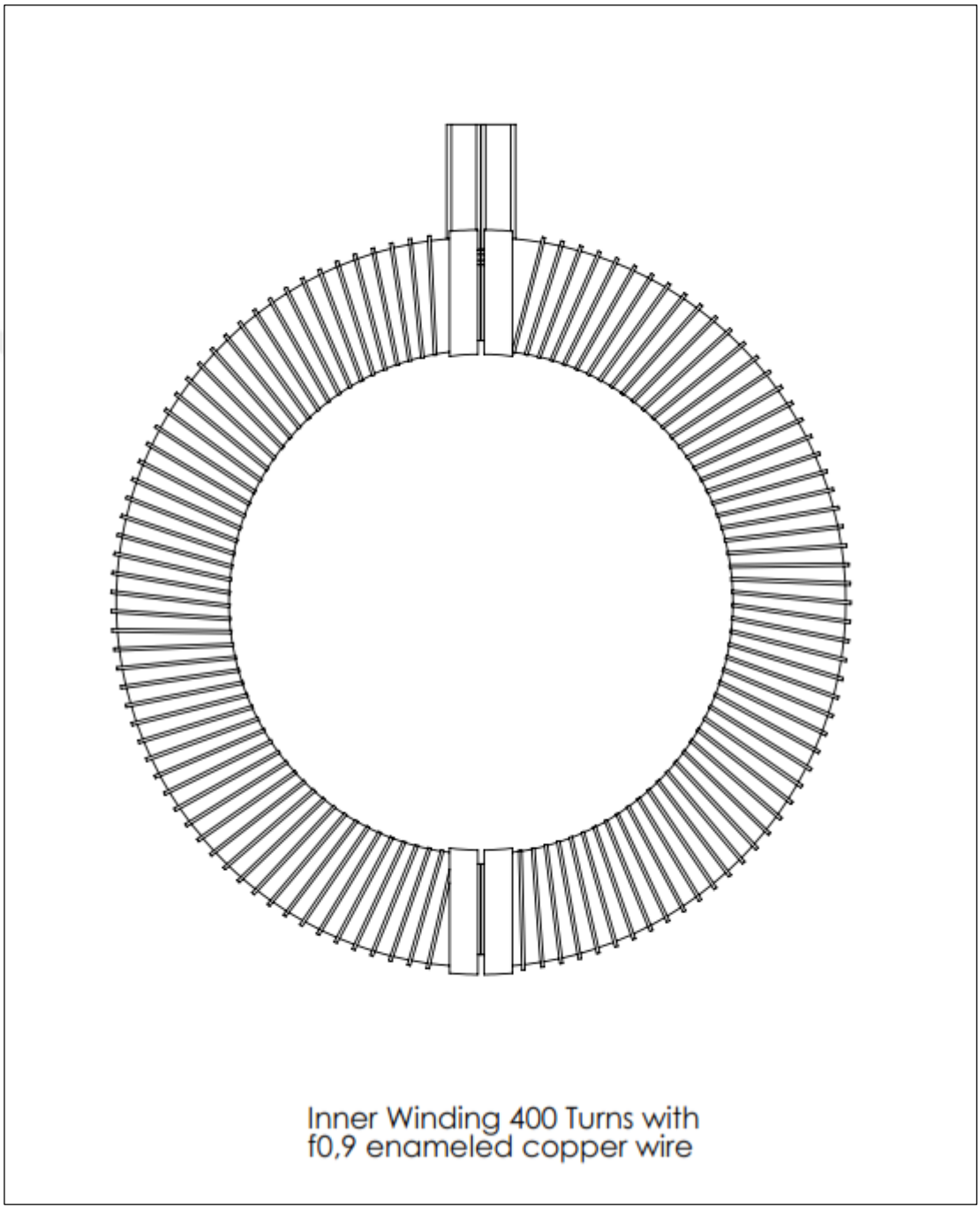

Enhanced Magnetic Cores

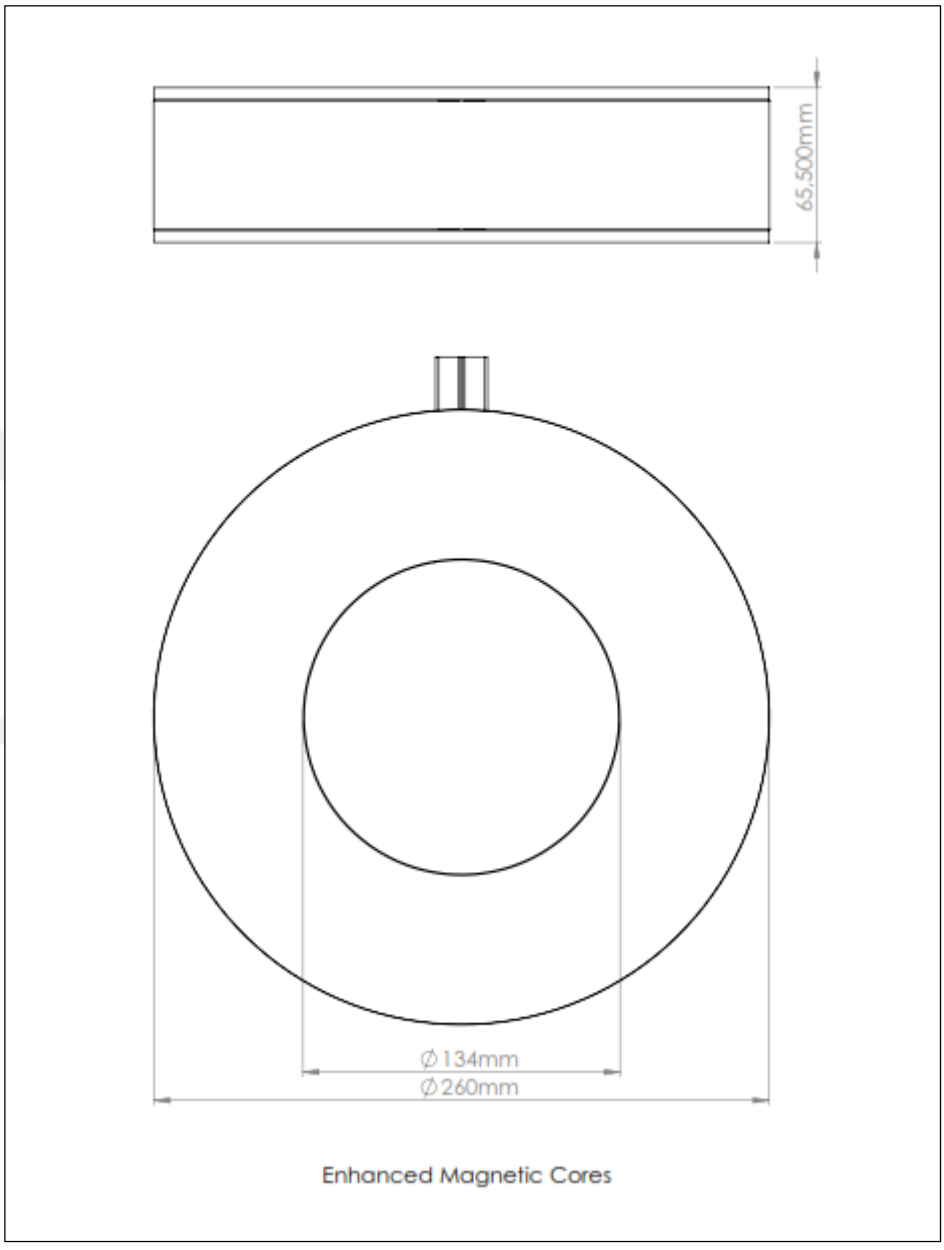

Outer Box

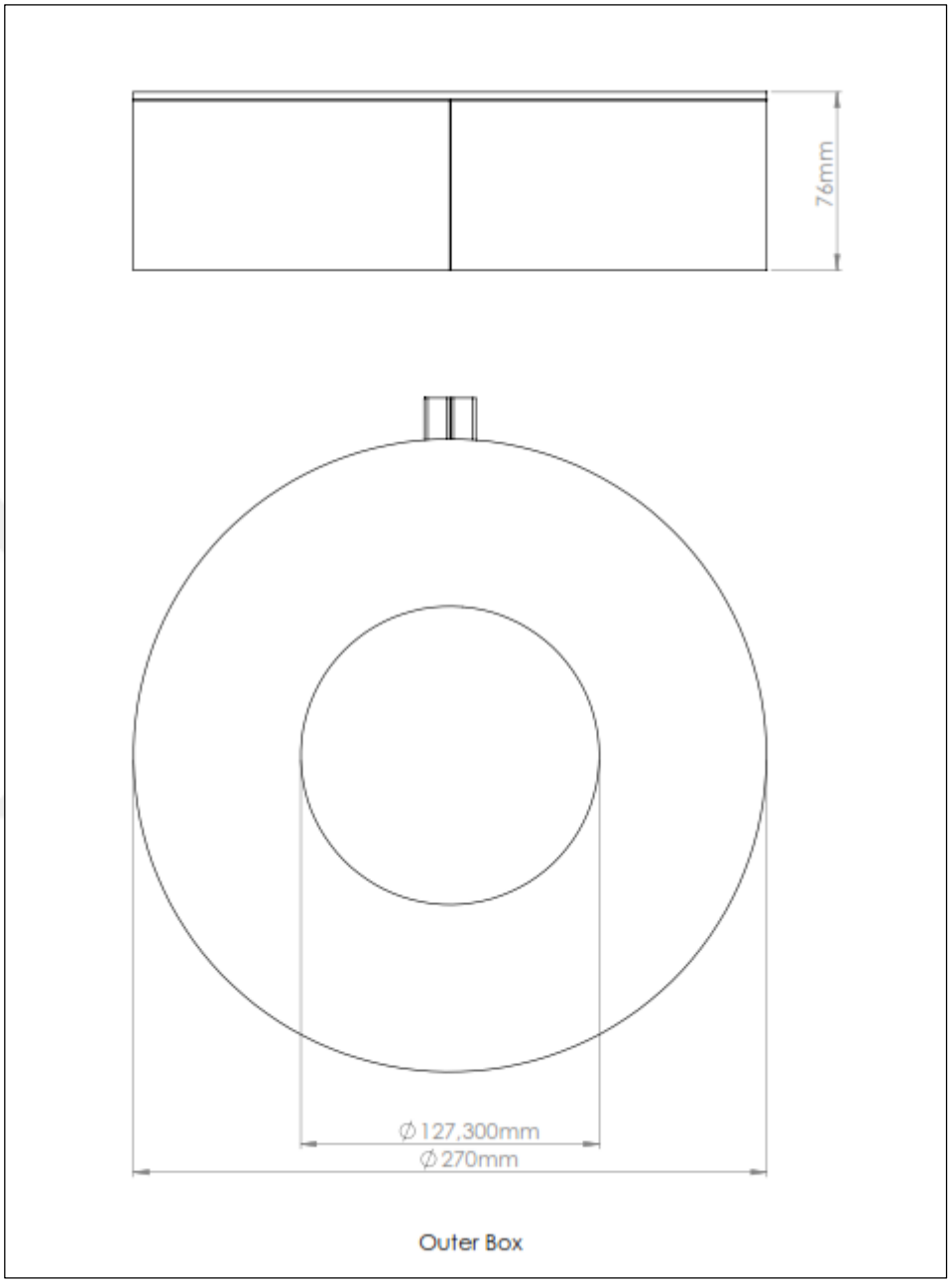

Outer Winding

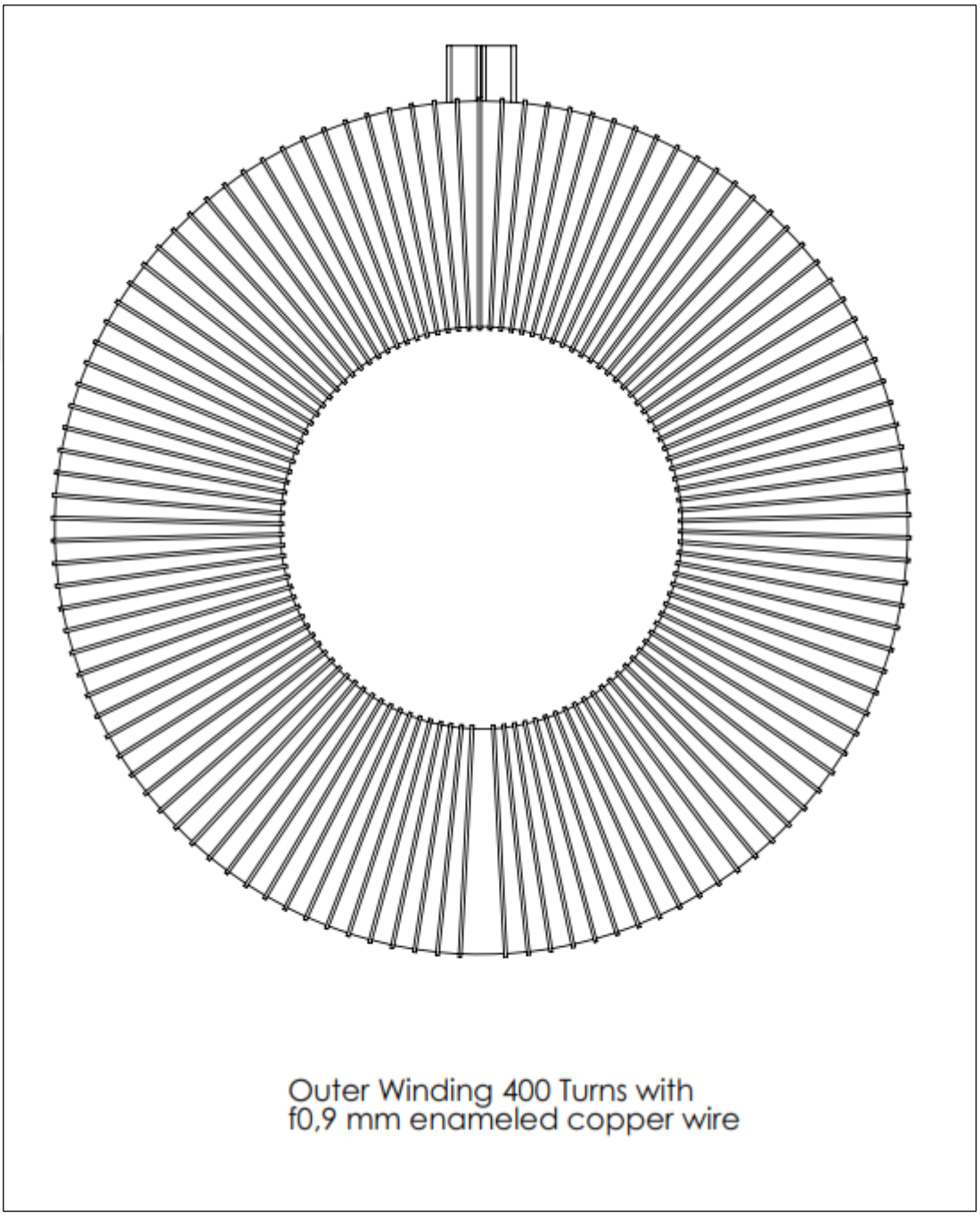

Final Outer Box